

Indexed in: EMBASE/Excerpta Medica,

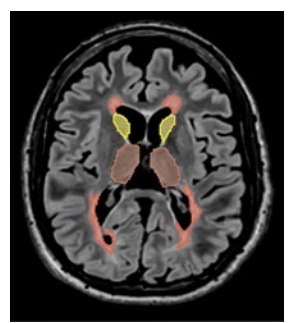
Journal of the Mexican Federation of Radiology and Imaging

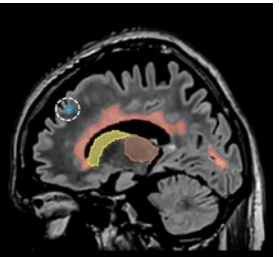
J Mex Fed Radiol Imaging

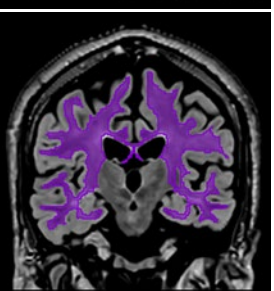
Volume 4. Number 3, July-September 2025

ISSN: 2938-1215

elSSN: 2696-8444











EDITORIAL

Are workforce radiologists concerned about ethical issues in artificial intelligence use? (p.139-141)

IN-DEPTH REVIEW

Endometriosis in magnetic resonance imaging: essentials for radiologists and clinicians (p.142-153)

FULL RESEARCH ARTICLES

Five-year mortality analysis of cirrhotic Mexican patients after a transjugular intrahepatic portosystemic shunt with or without a liver transplant (p.154-162)

Thalamic atrophy correlates with white matter lesion metrics in Mexican patients with multiple sclerosis: an automated MRI volumetry analysis (p.163-172)

Stiffness cut-off value of point-shear wave elastography (pSWE) for predicting malignancy in peripheral lymphadenopathy (p.173-183)

Vascular signs of Kaiser score* on contrast-enhanced breast MRI improve prediction of malignancy in mass and non-mass breast lesions (p.184-197)

BRIEF RESEARCH ARTICLE

Comparison of the diagnostic performance of Quantra artificial intelligence software with an experienced radiologist in the mammographic breast density assessment in women with and without breast implants (p.198-204)

CASE REPORT

Quantification of an intrathoracic organoaxial gastric volvulus secondary to a hiatal hernia diagnosed by multidetector computed tomography: a case report (p.205-210)

IMAGES IN RADIOLOGY

CT and MRI calcifications in the basal ganglia in primary hypoparathyroidism (p.211-213)

Official Journal of the



FEDERACIÓN MEXICANA DE RADIOLOGÍA E IMAGEN, A.C



Journal of the Mexican Federation of Radiology and Imaging

J Mex Fed Radiol Imaging

Volume 4. Number 3, July-September 2025

ISSN: 2938-1215

elSSN: 2696-8444

The Journal of the Mexican Federation of Radiology and Imaging (JMeXFRI) is the official journal of the Federacion Mexicana de Radiologia e Imagen. The aim of the journal is to disseminate scientific knowledge and technological developments for innovation in diagnostic and therapeutic radiology with original articles on basic and clinical aspects of modern radiology in an international context with global impact. JMeXFRI is published in American English with 4 issues per year (print and online) and the first issue was published in the first quarter of 2022. Articles undergo a rigorous, double-blind peer-review process. Publication of articles in JMexFRI is free of charge and all published articles are open access.

The journal publishes the following types of manuscripts: Full Research Article, Pictorial Essay, Brief Research Article, Technical Note, In-Depth Review, Case Report, Images in Radiology, and Editorial.

EDITORIAL BOARD

EDITOR-IN-CHIEF

Mauricio Figueroa-Sanchez, M.D.

Department of Radiology, Antiguo Hospital Civil de Guadalajara "Fray Antonio Alcalde", Guadalajara, Jal., Mexico

ASSOCIATE EDITORS

Gerardo E. Ornelas-Cortinas, M.D.

Centro Universitario de Imagen Diagnostica, Hospital Universitario "Dr. Jose E. Gonzalez", Monterrey, N.L., Mexico

Araceli Cue-Castro, M.D.

Department of Computed Tomography, Hospital General "Dr. Enrique Cabrera" SEDESA, Mexico City, Mexico

Oscar A. Chavez-Barba, M.D.

Department of Radiology,

Antiguo Hospital Civil de Guadalajara "Fray Antonio Alcalde",

Guadalajara, Jal., Mexico

Ana M. Contreras-Navarro, M.D., M.Sc., Ph.D.

Scientific Writing Workshop, JMeXFRI, Zapopan, Jal., Mexico

David Garza-Cruz, M.D.

Department of Radiology, Hospital Angeles, Torreon, Coah., Mexico

J. Mario Bernal-Ramirez, M.D.

Department of Medical Clinics, Centro Universitario de Ciencias de la Salud, Universidad de Guadalajara, Guadalajara, Jal., Mexico

SCIENTIFIC TRANSLATOR EDITOR

Sergio Lozano-Rodriguez, M.D.

Research Office of the Vice Dean, Hospital Universitario "Dr. Jose E. Gonzalez", Monterrey, N.L., Mexico

BIOSTATISTICS ADVISER

Cesar N. Cristancho-Rojas, M.D., M.Sc.

School of Public Health, Oregon Health & Science University, Portland, OR., USA

DESIGN ADVISER

Jorge Mendez-Palacios, B.Sc.

Design Area, JMeXFRI. Zapopan, Jal., Mexico

NATIONAL EDITORIAL BOARD

HEAD AND NECK RADIOLOGY

Mario A. Campos-Coy, M.D.

Centro Universitario de Imagen Diagnostica, Hospital Universitario "Dr. Jose E. Gonzalez", Monterrey, N.L., Mexico

Eduardo D. Sarda-Inman, M.D.

Diagnostico Especializado por Imagen, Zapopan, Jal., Mexico

GASTROINTESTINAL RADIOLOGY

Araceli Cue-Castro, M.D.

Department of Computed Tomography, Hospital General "Dr. Enrique Cabrera" SEDESA, Mexico City, Mexico

Adrian Negreros-Osuna, M.D., Ph.D.

Departamento de Radiologia, Hospital Regional ISSSTE Monterrey, Monterrey, N.L., Mexico

Oscar A. Chavez-Barba, M.D.

Department of Radiology, Antiguo Hospital Civil de Guadalajara "Fray Antonio Alcalde", Guadalajara, Jal., Mexico

OBSTETRIC AND GYNECOLOGIC RADIOLOGY

Dante R. Casale-Menier, M.D.

Department of Radiology and Imaging, Hospital Angeles, Ciudad Juarez, Chih., Mexico

Roberto J. Carrales-Cuellar, M.D.

Department of Ecographic Diagnosis, Radiologia Especializada, Guadalajara, Jal., Mexico

BREAST RADIOLOGY

David F. Perez-Montemayor, M.D.

General Direction, Centro de Imagenologia Integral IMAX, Tampico, Tamps., Mexico

Beatriz Gonzalez-Ulloa, M.D. Department of Breast Imaging,

Department of Breast Imaging, Diagnostico Especializado por Imagen, Guadalajara, Jal., Mexico

Margarita L. Garza-Montemayor, M.D.

Departamento de Imagen Diagnostica, Centro de Cancer de Mama, Hospital Zambrano Hellion, Tec Salud, Monterrey, N.L., Mexico

Karla M. Nuñez-Barragan, M.D.

Women's Imaging Department, Doctors Hospital East Auna Monterrey, N. L., Mexico

Yazmin A. Ramirez-Galvan, M.D., Ph.D.

Breast Imaging Section Department of Radiology and Imaging, University Hospital "Dr. Jose Eleuterio Gonzalez" Monterrey, N.L. Mexico

NUCLEAR AND MOLECULAR MEDICINE

Hugo E. Solis-Lara, M.D.

Centro de Imagen Molecular, Hospital Christus Muguerza Alta Especialidad, Monterrey, N.L., Mexico

NEURORADIOLOGY

Jorge Paz-Gutierrez, M.D.

Department of Magnetic Resonance, Centro Medico Puerta de Hierro, Zapopan, Jal., Mexico

Azalea Garza-Baez, M.D.

Department of Radiology and Imaging, Hospital Zambrano Hellion, Tecnologico de Monterrey, Monterrey, N.L., Mexico

Perla M. Salgado-Lujambio, M.D.

Direccion de Enseñanza, Instituto Nacional de Neurologia y Neurocirugia "Manuel Velasco Suarez" Mexico City, Mexico

Rebeca de J. Ramos-Sanchez. M.D.

Department of Neuroimaging, Instituto Nacional de Neurologia y Neurocirugia "Manuel Velasco Suarez" Mexico City, Mexico

PEDIATRIC RADIOLOGY

Aida Perez-Lara, M.D.

Department of Radiology, Hospital Español, Mexico City, Mexico

MUSCULOSKELETAL RADIOLOGY

Oscar A. Chavez-Barba, M.D.

Department of Radiology, Antiguo Hospital Civil de Guadalajara "Fray Antonio Alcalde", Guadalajara, Jal., Mexico

J. Francisco Diaz-Fernandez, M.D.

Department of Radiology, Hospital General "Agustin O'Horan", Merida, Yuc., Mexico

CHEST AND CARDIOVASCULAR RADIOLOGY

Sergio A. Criales-Vera, M.D.

Department of Radiology and Imaging, Instituto Nacional de Cardiologia "Ignacio Chavez", Mexico City, Mexico

Harold Goerne, M.D.

Department of Radiology, Hospital de Pediatria, Instituto Mexicano del Seguro Social, Guadalajara, Jal., Mexico

Luis F. Alva-Lopez, M.D.

Department of Radiology, Hospital Medica Sur, Mexico City, Mexico

GENITOURINARY RADIOLOGY

Sergio B. Peregrina-Gonzalez, M.D.

Consultorio de Imagen, Guadalajara, Jal., Mexico

Araceli Cue-Castro, M.D.

Department of Computed Tomography, Hospital General "Dr. Enrique Cabrera" SEDESA, Mexico City, Mexico

Adrian Negreros-Osuna, M.D.

Departamento de Radiologia, Hospital Regional ISSSTE Monterrey, Monterrey, N.L., Mexico

Benjamin Conde-Castro, M.D.

Faculty of Medicine, Universidad Nacional Autónoma de Mexico, Mexico City, Mexico

ULTRASOUND

Rosa M. Alanis-Salazar, M.D.

Departamento de Radiologia, UMF Guadalupe, ISSSTE, Monterrey, NL., Mexico

Victor M. Rodriguez-Peralta, M.D.

Department or Radiology, Fundacion de Cancer de Mama (FUCAM), Oaxaca, Oax., Mexico

David Garza-Cruz, M.D.

Department of Radiology, Hospital Angeles, Torreon, Coah., Mexico

Manuel Hernandez-Cruz, M.D.

Area de Ultrasonido, Unidad de Ultrasonido Diagnostico, Puebla, Pue. Mexico

VASCULAR AND INTERVENTIONAL RADIOLOGY

Guillermo Elizondo-Riojas, M.D., Ph.D.

Centro Universitario de Imagen Diagnostica, Hospital Universitario "Dr. Jose E. Gonzalez", Monterrey, N.L., Mexico

Raul A. De Luna-Vega. M.D.

Centro Universitario de Imagen Diagnostica, Hospital Universitario "Dr. Jose E. Gonzalez", Monterrey, N.L., Mexico

ARTIFICIAL INTELLIGENCE

Guillermo Elizondo-Riojas, M.D., Ph.D.

Centro Universitario de Imagen Diagnostica, Hospital Universitario "Dr. Jose E. Gonzalez", Monterrey, N.L., Mexico

Adrian Negreros-Osuna, M.D.

Departamento de Radiología, Hospital Regional ISSSTE Monterrey, Monterrey, N.L., Mexico

J. Mario Bernal-Ramirez, M.D.

Department of Medical Clinics, Centro Universitario de Ciencias de la Salud, Universidad de Guadalajara, Guadalajara, Jal., Mexico

Benjamin Conde-Castro, M.D.

Faculty of Medicine, Universidad Nacional Autonoma de México, Mexico City, Mexico

JUNIOR EDITORIAL BOARD

J. Mario Bernal-Ramirez, M.D.

Department of Medical Clinics, Centro Universitario de Ciencias de la Salud, Universidad de Guadalajara, Guadalajara, Jal., Mexico

Ana K. Luna-Marroquin, M.D.

Centro Universitario de Imagen Diagnostica, Hospital Universitario "Dr. Jose E. Gonzalez", Monterrey, N.L., Mexico

M. Lourdes Garcia-Colmenero, M.D.

Departamento de Radiologia, CID Centro de Imagen y Diagnostico Guadalajara, Jal., Mexico

Xavier A. Gonzalez-Ballesteros, M.D.

Departamento de Radiologia, Hospital San Angel Inn Universidad, Ciudad de Mexico, Mexico

Adriana Parada-Gallardo, M.D.

Department of Radiology, Hospital General de Zapopan, Zapopan, Jal., Mexico

A. Sofia Sanchez-Gomez, M.D.

Department of Radiology, Grupo RIO Centro Integral de Diagnostico Medico Guadalajara, Jal., Mexico

INTERNATIONAL EDITORIAL BOARD

HEAD AND NECK RADIOLOGY

Richard H. Wiggins, M.D.

Department of Radiology and Imaging Sciences, School of Medicine, University of Utah, Salt Lake City, UT., USA

Amy Juliano, M.D.

Department of Radiology, Massachusetts Eye and Ear, Harvard Medical School, Boston, MA., USA

GASTROINTESTINAL RADIOLOGY

Luis Martí-Bonmatí, M.D., PH.D.

Grupo de Investigación Biomédica en Imagen (GIBI230) Instituto de Investigación Sanitaria La Fe Área Clínica de Imagen Médica, Hospital Universitario y Politécnico La Fe, Valencia, Spain

Jorge A. Soto, M.D.

Department of Radiology, Boston Medical Center, Boston, MA., USA

Jorge Elias Jr. Ph.D.

Departamento de Imagenes Medicas, Oncologia e Hematologia, Faculdade de Medicina Ribeirao Preto, Universidade Sao Paulo Ribeirao Preto, Sao Paolo, Brazil

Valdair F. Muglia, M.D.

Faculdade de Medicina de Ribeiraõ Preto, Universidade de Saõ Paulo, Ribeiraõ Preto, Sao Paolo, Brazil

Carlo Catalano, M.D.

Department of Diagnostic Radiology La Sapienza University of Rome Rome. Italv

OBSTETRIC AND GYNECOLOGIC RADIOLOGY

Luciana Pardini Chamie, M.D., Ph.D.

Centro de Diagnostico Ultrasonografico Especializado en Imagen de la Mujer, Sao Paolo, Brazil

BREAST RADIOLOGY

Javier Romero-Enciso, M.D.

Department of Radiology, Fundacion Santa Fe, Bogota, Colombia

NUCLEAR AND MOLECULAR MEDICINE

Begoña Martinez-Sanchis, M.D.

Department of Nuclear Medicine, Hospital Universitario y Politecnico La Fe, Valencia, Spain

Cesar N. Cristancho-Rojas, M.D., M.Sc.

School of Public Health, Oregon Health & Science University, Portland, OR., USA

NEURORADIOLOGY

Roy F. Riascos-Castaneda, M.D.

Department of Radiology and Neurosurgery, Memorial Hermann Hospital System, Houston, TX., USA

Rafael Rojas-Jasso, M.D.

Department of Radiology, Beth Israel, Deaconess Medical Center, Boston, MA., USA

Henrique Carrete Jr., M.D., Ph.D.

Department of Diagnostic Imaging, Universidad de Sao Paulo, Sao Paulo, Brazil

Carlos Torres, M.D.

Department of Diagnostic Imaging, The Ottawa Hospital, Ottawa, Canada

MUSCULOSKELETAL RADIOLOGY

Javier Fernandez-Jara, M.D.

Department f Radiology, Hospital Universitario Sanitas La Zarzuela, Madrid, Spain

Jose Luis del Cura, M.D.

Radiodiagnosis Service, Hospital Universitario Donostia, San Sebastian-Donostia, Spain

Diego F. Lemos, M.D.

Department of Radiology, University of Vermont Medical Center, Burlington, VT, USA

PEDIATRIC RADIOLOGY

George Bisset, M.D.

Department of Radiology, Children's Hospital Pennsylvania, PA., USA

Sara Reis Teixeira, M.D., Ph.D.

Department of Radiology, Children's Hospital Pennsylvania, PA. USA

CHEST AND CARDIOVASCULAR RADIOLOGY

Fernando R. Gutierrez, M.D.

Department of Radiology and Cardiothoracic Imaging, The Mallickroat Institute of Radiology, St. Louis, MO., USA

Jorge Carrillo-Bayona, M.D.

Department of Radiology, Hospital Universitario Mayor, Bogota, Colombia

Carlos S. Restrepo, M.D.

Department of Cardiothoracic Radiology, Texas University, San Antonio, TX., USA

Sebastian Rossini, M.D.

Department of Radiology, Instituto Radiologico Mater Dei, Buenos Aires, Argentina

Santiago Martinez-Jimenez, M.D.

Department of Radiology, Saint Luke's Hospital of Kansas City, Kansas City, KS., USA

L. Antonio Sosa-Lozano, M.D.

Department of Cardiothoracic Radiology, Medical College of Wisconsin, Milwaukee, WI., USA

GENITOURINARY RADIOLOGY

Daniela Stoisa, M.D.

Department of Radiology, Diagnostico Medico Oroño, Rosario, Santa Fe, Argentina

Valdair F. Muglia, M.D.

Faculdade de Medicina de Ribeirao Preto, Universidade de Sao Paulo Ribeirao Preto, Sao Paulo, Brazil

ULTRASOUND

Edward G. Grant, M.D.

Department of Radiology, USC Norris Cancer Center, Los Angeles, CA., USA

Juan P. Niedmann-Espinosa, M.D.

Department of Ecotomography, Clinica Alemana de Santiago, Santiago de Chile, Chile

VASCULAR AND INTERVENTIONAL RADIOLOGY

Manuel Cifrian-Perez, M.D., Ph.D.

Imaging Clinic Department, Hospital Universitario y Politecnico La Fe, Valencia, Spain

ARTIFICIAL INTELLIGENCE

Luis Martí-Bonmatí, M.D., Ph.D.

Grupo de Investigación Biomédica en Imagen (GIBI230) Instituto de Investigación Sanitaria La Fe Área Clínica de Imagen Médica, Hospital Universitario y Politécnico La Fe Valencia, Spain

Leonor Cerda-Alberich, Ph.D

Imaging Clinic Department, Hospital Universitario y Politecnico La Fe, Valencia, Spain

Felipe Campos Kitamura, M.D., Ph.D.

Dasalnova, Dasa, Sao Paulo, Brazil

WEBSITE ADMINISTRATION COMMITTEE

David Garza-Cruz, M.D.

Coordinator, Department of Radiology, Hospital Angeles, Torreon, Coah., Mexico

Ana Karen Luna-Marroquin, M.D.

Head and Neck Radiology Section Centro Universitario de Imagen Diagnostica, Hospital Universitario "Dr. Jose E. Gonzalez", Monterrey, N.L., Mexico

Hugo E. Solis-Lara, M.D.

Gastrointestinal Radiology Section and Nuclear And Molecular Medicine Section Centro de Imagen Molecular, Hospital Christus Muguerza Alta Especialidad, Monterrey, N.L., Mexico

Dante R. Casale-Menier, M.D.

Gynecology and Obstetrics Radiology Section Genitourinary Radiology Section Department of Radiology and Imaging, Hospital Angeles, Ciudad Juarez, Chih., Mexico

Beatriz Gonzalez-Ulloa, M.D.

Breast Radiology Section Department of Breast Imaging, Diagnostico Especializado por Imagen, Guadalajara, Jal., Mexico

Yazmin A. Ramirez-Galvan, M.D., Ph.D.

Breast Radiology Section Breast Imaging Section Department of Radiology and Imaging, University Hospital "Dr. Jose Eleuterio Gonzalez" Monterrey, N.L. Mexico

Rebeca de J. Ramos-Sanchez, M.D.

Neuroradiology Section Department of Neuroimaging, Instituto Nacional de Neurologia y Neurocirugia "Manuel Velasco Suarez" Mexico City, Mexico

Aida Perez-Lara, M.D.

Pediatric Radiology Section Department of Radiology, Hospital Español, Mexico City, Mexico

Gerardo E. Ornelas-Cortinas, M.D.

Musculoskeletal Radiology Section Centro Universitario de Imagen Diagnostica, Hospital Universitario "Dr. Jose E. Gonzalez", Monterrey, N.L., Mexico

Cesar N. Cristancho-Rojas, M.D., M.Sc.

Chest and Cardiovascular Radiology Section School of Public Health, Oregon Health & Science University, Portland, OR., USA

J.M. Ignacio Lopez-Mendez, M.D.

Ultrasound Section
Department of Radiology and Imaging,
Hospital de Especialidades, CMNO
Instituto Mexicano del Seguro Social,
Guadalajara, Jal., Mexico.

Mauricio Figueroa-Sanchez, M.D.

Vascular and Interventional Radiology Section Department of Radiology, Antiguo Hospital Civil de Guadalajara "Fray Antonio Alcalde", Guadalajara, Jal., Mexico

J. Mario Bernal-Ramirez, M.D.

Artificial Intelligence Radiology Section Department of Medical Clinics, Centro Universitario de Ciencias de la Salud, Universidad de Guadalajara, Guadalajara, Jal., Mexico

Diana Camorlinga-Ornelas, M.D

General Radiology Section, Imaging Department Hospital General Regional Num. 2 Mexican Social Security Institute Ciudad Juarez, Chih., Mexico.

GRAPHICAL ABSTRACTS COMMITTEE

Oscar A. Chavez-Barba, M.D.

Department of Radiology, Antiguo Hospital Civil de Guadalajara "Fray Antonio Alcalde", Guadalajara, Jal., Mexico

Adriana Parada-Gallardo, M.D.

Department of Radiology, Hospital General de Zapopan, Zapopan, Jal., Mexico

J.M. Ignacio Lopez-Mendez, M.D.

Department of Radiology and Imaging, Hospital de Especialidades, CMNO Instituto Mexicano del Seguro Social, Guadalajara, Jal., Mexico.

Juan Pablo Lopez-Gutierrez, M.D.

Department of Radiology and Imaging, Hospital General de Zona 3, Instituto Mexicano del Seguro Social Aguascalientes, Ags., Mexico

Gerardo Llamas-Linares, M.D.

Centro Universitario de Imagen Diagnostica, Hospital Universitario "Dr. Jose E. Gonzalez", Monterrey, N.L., Mexico

Alejandra I. Castillo-Cervantes, M.D.

Centro Universitario de Imagen Diagnostica, Hospital Universitario "Dr. Jose E. Gonzalez", Monterrey, N.L., Mexico

A. Sofia Sanchez-Gomez, M.D.

Department of Radiology, Grupo RIO Centro Integral de Diagnostico Medico, Guadalaiara, Jal., Mexico

SOCIAL MEDIA COMMITTEE

Guillermo Elizondo-Riojas, M.D., Ph.D.

Centro Universitario de Imagen Diagnostica, Hospital Universitario "Dr. Jose E. Gonzalez", Monterrey, N.L., Mexico

Oscar A. Chavez-Barba, M.D.

Department of Radiology, Antiguo Hospital Civil de Guadalajara "Fray Antonio Alcalde", Guadalajara, Jal., Mexico

J. Mario Bernal-Ramirez, M.D.

Department of Medical Clinics, Centro Universitario de Ciencias de la Salud, Universidad de Guadalajara, Guadalajara, Jal., Mexico

Adriana Parada-Gallardo, M.D.

Department of Radiology, Hospital General de Zapopan, Zapopan, Jal., Mexico

A. Sofia Sanchez-Gomez, M.D.

Department of Radiology, Grupo RIO Centro Integral de Diagnostico Medico. Guadalajara, Jal., Mexico

RADIOLOGICAL AND CLINICAL CORRELATION BOARD

GASTROENTEROLOGY

Linda E. Muñoz-Espinosa, M.D., Ph.D.

Liver Unit, Hospital Universitario "Dr. Jose E. Gonzalez", Monterrey, N.L., Mexico

David Marti-Aguado, M.D., Ph.D.

Servicio Medicina Digestiva, Hospital Clinico Universitario, Valencia, Spain

GASTROINTESTINAL AND GENERAL SURGERY

Carlos Nuño-Guzman, M.D., M.Sc.

Department of Surgery, Antiguo Hospital Civil de Guadalajara "Fray Antonio Alcalde", Guadalajara, Jal., Mexico

OBSTETRICS AND GINECOLOGY

Sergio Fajardo-Dueñas, M.D., M.Sc.

Division of Obstetrics and Ginecology, Nuevo Hospital Civil de Guadalajara, Guadalajara, Jal., Mexico

NEUROLOGY

Jose L. Ruiz-Sandoval, M.D., M.Sc.

Department of Neurology, Antiguo Hospital Civil de Guadalajara "Fray Antonio Alcalde", Guadalajara, Jal., Mexico

RHEUMATOLOGY

Monica Vazquez del Mercado-Espinosa, M.D., Ph.D.

Division of Medicine, Nuevo Hospital Civil de Guadalajara, Guadalajara, Jal., Mexico.

CARDIOI OGY-PNFUMOI OGY

Jose M. Hernandez, M.D.

Department of Ecocardiography, Doctors Hospital, Monterrey, N.L., Mexico

PATHOLOGICAL ANATOMY

Marco A. Ponce-Camacho, M.D., Ph.D.

Department of Cytopathology, Doctors Hospital, Monterrey, N.L., Mexico

ENDOCRINOLOGY

Jesus Zacarias Villarreal-Perez. M.D.

Department of Endocrinology, Hospital Universitario "Dr. Jose E. Gonzalez", Monterrev. N.L.. Mexico

HEMATOLOGY

Carlos R. Best-Aguilera, M.D.

Department of Hematology, Hospital General de Occidente. Secretaria de Salud Zapopan, Jal., Mexico

GYNECOLOGICAL UROLOGY

Patricia I. Velazquez-Castellanos, M.D., M.Sc.

Department of Gynecology and Obstetrics, Antiguo Hospital Civil de Guadalajara "Fray Antonio Alcalde", Guadalajara. Jal., Mexico

PEDIATRIC NEUROLOGY

Daniel Perez-Rulfo Ibarra, M.D., Ph.D.

Departamento de Pediatria, Antiguo Hospital Civil de Guadalajara "Fray Antonio Alcalde", Guadalajara, Jal., Mexico

Follow us



https://instagram.com/jmexfri

https://facebook.com/jmexfri

https://youtube.com/@jmexfri

https://x.com/jmexfri



Original papers should be deposited in their electronic version through the following URL:

https://publisher.jmexfri.permanyer.com





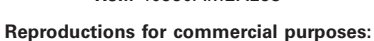
Permanyer Mexico

Temistocles, 315 Col. Polanco, Del. Miguel Hidalgo 11560 Ciudad de Mexico mexico@permanyer.com

Permanyer

Mallorca, 310 - Barcelona (Cataluña), España permanyer@permanyer.com

> ISSN: 2696-8444 Ref.: 10990AMEX253



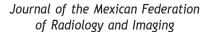
Without the prior written consent of the publisher, no part of this publication may be reproduced, stored in a retrievable medium or transmitted, in any form or by any means, electronic, mechanical, photocopying, recording or otherwise, for commercial purposes.



The opinions, findings, and conclusions are those of the authors. The editors and publisher are not responsible and shall not be liable for the contents published in the journal.

© 2025 Federacion Mexicana de Radiologia e Imagen, AC. Published by Permanyer.









EDITORIAL

Are workforce radiologists concerned about ethical issues in artificial intelligence use?

Gerardo E. Ornelas-Cortinas^{1,2}* and Ana K. Luna-Marroquin lo

¹Department of Diagnostic and Imaging, University Hospital "Dr. Jose E. Gonzalez", Universidad Autonoma de Nuevo Leon; ²Doctors Hospital Auna. Monterrey, Nuevo Leon, Mexico

Artificial intelligence (AI) in medical practice is increasing. No one denies its significant benefits: a futuristic vision of tools that can provide more accurate and faster diagnoses of pathologies that medical professionals face daily. Radiology has had a major impact on Al due to its interaction with digital images. The number of publications on AI applied to different imaging modalities has increased significantly over the last 10 years, from 100 to 150 articles per year to around 800 per year in 2017¹. Al with deep learning algorithms has been studied and used to diagnose breast and colon cancer, detect lung nodules, and Alzheimer disease, among others². Other AI applications include the importance given to oncological imaging in nuclear medicine studies to assess tumor aggressiveness, treatment response, and prognosis3.

Al is on everyone's lips. Something about Al is shared almost daily on various social media platforms, to the point that it overwhelms us. Due to the extensive information and research being conducted by numerous developers of these systems, there has been considerable discussion regarding the ethical issues that arise when using Al in radiology. There is a consensus in Europe, the United States, Canada, and other countries⁴ that researchers are concerned about the honest use of Al in patient care. Particular attention has been paid to questions such as: Who owns the data? Were the patients whose data was used informed

that their images and data would be used for an Al algorithm? How was this data used? And, very importantly, how was it acquired and by whom? Is it those who are financial stakeholders, even if they have no medical knowledge? In other words, do you have access to the data if you have the necessary funds? Another bias that has been considered is explainability, reliability, and the infamous black box where no one knows exactly how the decision-making process was conducted. Some speak of an oracle that makes decisions without justification due to the convoluted nature of this process⁵.

We cannot overlook liability, i.e., when at the end of the decision-making process to conclude a radiology report using AI for diagnosis, an error occurs because AI has overdiagnosed a pathological entity, or vice versa, when the AI interprets an opacity as a composite image, and, after months, it turns out to be a neoplasm. The radiologist confirms this diagnosis without discussing the findings and gives the result, which is not wrong. Who is responsible? The radiologist who trusted the algorithm, the person who bought the tool for the institution, the person who sold it, the person who developed it, or the person who used the data to arrive at the final diagnosis⁶. In the end, we will all be held accountable.

While, as previously mentioned, much has already been written about the consensus and ethical measures to be considered regarding data use, information gathering,

the black box, and the fair and beneficial use of AI in its implementation and application in daily practice, we are left with another question. Are radiologists who are responsible for the day-to-day tasks prepared for the integration of AI into their daily work? We are not talking about using a tool that we know we can learn to operate by pressing a button, selecting a region of interest, and learning the different patterns to interpret the information the tool gives us. Ultimately, that's our job: to interpret imaging information so that we can make a diagnosis that's useful for the patient, allowing doctors to make informed treatment decisions. That's not what we're getting at. The question is whether we are aware of the ethical dilemmas that surround this process. Those who write about ethics know this, of course, but the radiologist, who does their best every day to dictate numerous examinations that sometimes exceed their capacity due to the time devoted to each exam, is where diagnostic errors can occur...is the radiologist aware of this? Perhaps an administrator has not considered using an Al tool available from one of the many companies that claim to be better than the competition. Have they asked the physician who will be using it which tool would be most useful for that facility's operations that best fits their daily work?

Hospitals are competing and promoting the use of Al, but is this competition a genuine concern for the benefit of patients, or is it just business? Is it about being the first in town or the first in the country? It is clear that medicine is a business, but it must be conducted honestly and in accordance with the basic principles of bioethics. Reference is made to a survey of radiologists and residents that attempted to determine the level of knowledge of bioethical principles. The result was that the level of knowledge was in the middle range, which is representative of what can occur in the field of radiology⁷.

Despite all the excellent observations and recommendations mentioned in the various consensus reports and publications, there is one aspect we consider fundamental, education before implementation. In our view, this would be the basis for the ethical use of AI, because in hospitals, someone makes the decision to implement AI for the radiology group, and it turns out that they did not consider implementing a methodology to educate the ethics of using diagnostic tools. AI should not replace the radiologist's work, but rather complement it, and it should always be under their supervision. Unfortunately,

some colleagues believe that AI will make their work easier and faster, allowing them to work less and continue to be paid while someone else does their work without supervision. It has been considered that a conflict of interest could arise by rushing into this technology without assessing its scope and responsibility. We need to act responsibly, knowing that technology is constantly evolving and prone to errors. We must protect ourselves from unethical situations before they arise.

As many AI models are relatively easy to create and train, AI-supported research and commercial solutions can be produced by sometimes naïve or unprofessional actors⁴.

Conscious ethical values should guide decisions about when to use AI, define metrics to describe it appropriately and responsibly, and warn the community about the risks of unethical AI⁴. In our opinion, there is an urgent need to demonstrate knowledge of AI; otherwise, you are obsolete. There is a need for it to happen, but we don't know how. There's a need not only to buy AI, but also to sell it, justifying that it benefits patients without knowing whether it is a tool whose development has been guided by bioethical principles.

Radiologists, who are the workforce, need to be trained in the ethical use of AI tools; otherwise, we will make mistakes that could put patients at risk. What training and skills are needed to decide whether to use AI on patients and to use it safely and effectively when appropriate?⁴ This is a foundation for implementing AI in institutions. We need to be cautious about patients who are at risk due to the need for a diagnosis, so they are not subjected to interventions that may not be warranted but incur costs that many may not be willing to authorize if asked. We believe we are ready for AI. We want it. However, most radiologists are not ready to use it with the knowledge of the bioethical principles that enable us to use it responsibly, fairly, and ethically.

Funding

Not applicable.

Conflicts of interest

The authors disclose no potential conflicts of interest.

REFERENCES

- Pesapane F, Volonté C, Codari M, Sardanelli F. Artificial intelligence as a medical device in radiology: ethical and regulatory issues in Europe and the United States. Insights Imaging. 2018;9(5):745-753. doi:10.1007/ s13244-018-0645-y.
- Mudgal KS, Das N. The ethical adoption of artificial intelligence in radiology. BJR Open. 2020;2(1):20190020. doi:10.1259/bjro.20190020.
- Kujawa MJ, Cerdá-Alberich L, Martí-Bonmatí L. Artificial intelligence in oncologic imaging: enhancing diagnostic precision towards facilitating clinical decision-making. J Mex Fed Radiol Imaging. 2025;4(2):69-83. doi:10.24875/JMEXFRI.M25000101.
- Geis JR, Brady A, Wu CC, Spencer J, Ranschaert E, Jaremko JL, et al. Ethics of artificial intelligence in radiology: summary of the joint European and North American Multisociety Statement. Insights Imaging. 2019; 10(1):101. doi:10.1186/s13244-019-0785-8.
- Goisauf M, Cano-Abadía M. Ethics of Al in radiology: a review of ethical and societal implications. Front Big Data. 2022;5:850383. doi:10.3389/ fdata.2022.850383.
- Mazurowski MA. Artificial intelligence in radiology: some ethical considerations for radiologists and algorithm developers. Acad Radiol. 2020; 27(1):127-129. doi:10.1016/j.acra.2019.04.024.
- (1).127-129. doi.10.1016/j.adat.2019.04.204.
 Ornelas-Cortinas GE, Cantú-Salinas AC, Luna-Marroquín AK. Knowledge of bioethical principles and elements of responsibility in radiology. J Mex Fed Radiol Imaging, 2023;2(1):98-105. doi:10.24875/JMEXFRI.M23000047.





IN DEPTH REVIEW

Endometriosis in magnetic resonance imaging: essentials for radiologists and clinicians

Laura M. Olarte-Bermudez¹*, Ana M. Rendon-Garavito¹, Andres F. Herrera-Ortiz^{1,2}, Sara Paris-Zorro¹, Diana Romero-Mavorga¹ and Javier Romero-Enciso¹

ABSTRACT

Endometriosis is a chronic disease, characterized by the growth and implantation of endometrial tissue outside the uterus, usually in deep pelvic structures, often resulting in inflammation, fibrosis and pain. The ovaries, the uterosacral ligaments, the rectovaginal septum, and, less frequently, other parts outside of the pelvis such as the diaphragm and the sciatic nerve are frequently affected. Timely diagnosis remains a challenge despite the high prevalence due to the heterogeneous clinical presentation. Magnetic resonance imaging (MRI), provides better resolution compared to other imaging modalities and helps identify different forms of the disease, including superficial, deep infiltrative endometriosis (DIE) and endometriomas. This review describes the recommended MRI protocol, descriptions of key imaging findings, the Deep Pelvic Endometriosis Index (dPEI) and the MRI consensus lexicon, and the ENDOVALIRM group's compartment-based approach an MRI-based system that helps classify disease by severity and location for guiding clinical decisions, support preoperative planning and predict surgical outcomes. According the compartment-based approach an MRI-based system, two horizontal lines divide the pelvis into an anterior, a middle and posterior region. In addition, vertical lines divide the pelvis into a central, a left and a right compartment. This anatomical framework creates 9 compartments: anterolateral, anteroventral, mediolateral, midcentral, posterolateral, posterior-central with additional extrapelvic areas. This review aims to support radiologists and gynecology teams in the accurate detection and classification of endometriosis through standardized MRI interpretation, increasing diagnostic confidence and contributing to better surgical and clinical outcomes.

Keywords: Endometriosis. Magnetic resonance imaging. Deep pelvic endometriosis index. ENDOVALIRM group. MRI protocol.

INTRODUCTION

Endometriosis is a common chronic inflammatory disease, characterized by abnormal growth of endometrial tissue outside the uterus, which is usually benign but with a heavy health burden. Ectopic endometrial tissue consists of normal endometrial stroma and glands that react to the hormonal changes that occur during the menstrual cycle. These periodic hormonal changes are associated with cyclic bleeding, and fibrosis¹. This condition occurs

in approximately 5-10% of women of childbearing age, with the global burden estimated to be around 176 million women worldwide. According to some studies, the prevalence in some populations is as high as 20% of women^{2,4}. Endometriosis is present in up to 90% of patients presenting with infertility and chronic pelvic pain. Despite this, around 65% of cases are misdiagnosed^{5,6}.

There have been major advances in the detection and characterization of different patterns and locations using diagnostic modalities such as magnetic resonance

*Corresponding author:

Laura M. Olarte-Bermudez E-mail: lauraolbe@unisabana.edu.co Received for publication: 23-04-2025 Accepted for publication: 15-09-2025 DOI: 10.24875/JMEXFRI.25000008 Available online: 10-10-2025 J Mex Fed Radiol Imaging. 2025;4(3):142-153 www.JMeXFRI.com

2696-8444 / © 2025 Federación Mexicana de Radiología e Imagen, A.C. Published by Permanyer. This is an open access article under the CC BY-NC-ND (https://creativecommons.org/licenses/by-nc-nd/4.0/).

¹Department of Radiologia, Fundacion Santa Fe de Bogota; ²Facultad de Medicina, Universidad del Bosque. Bogota, Colombia

imaging (MRI). However, timely and accurate diagnosis of endometriosis remains a challenge as the disease presents very differently in terms of both symptoms and imaging findings⁵. This contributes to the fact that it typically takes 10 years between the onset of symptoms and diagnosis, with most women seeing 3 or more doctors and healthcare professionals before receiving the correct diagnosis. Typically, the diagnosis is not made until the fourth decade of life, although symptoms usually begin in the early twenties⁶. In light of these cases, this review compiles updates for radiologists, trainees, and gynecologists to take a better approach to endometriosis by introducing a standardized scale that allows radiologists to appropriately communicate their findings to gynecologists.

NORMAL GYNECOLOGICAL ANATOMY

The uterus is a pear-shaped reproductive organ located in the female pelvis between the rectum in the posterior region and the bladder in the anterior region. This organ can be divided into three main segments: the fundus, the body and the cervix. The body and the fundus are mostly composed of the myometrium, the main muscle layer, which is made up of layered and interwoven smooth muscles interspersed with arterioles, nerves and areolar tissue, which ensures their contractile function and better structural integrity. Distally, the uterine body narrows, and opens into the vagina via the cervical canal. The fibers of the outer layer of the body and the fundus are arranged transversely and continue into the surrounding structures. including the fallopian tubes, the round ligament and the ovary ligament⁷. The uterus is covered on the outside by the serosa, a thin layer derived from the peritoneum. Inside, the uterine cavity is lined by the endometrium, an epithelial stroma containing tubular endometrial glandular tissue, that changes cyclically with the phases of the menstrual cycle8. In approximately 80% of women, the uterus is in anteversion.

Above and anteriorly, the peritoneum covers the uterine body and the bladder and forms the vesicouterine pouch. Posteriorly, the peritoneum covers the fundus, the cervix and the upper part of the vagina, and form the rectouterine pouch, also known as the Douglas pouch. On MRI, the endometrium can be visualized as a hyperintense structure on T2-weighted images and shows homogeneous, low-signal, non-contrastenhanced T1-weighted imaging⁷.

The cervix, which acts as a connecting duct between the uterine cavity and the vagina, normally measures approximately 4 cm in length and 3 cm in diameter in non-pregnant women. On high-resolution T2-weighted MRI of the pelvis, the cervix can be differentiated into three zones: a central hyperintense zone formed by the endocervical mucosa, a hypointense middle layer, and an outer layer with low to moderate signal intensity, both consisting of fibromuscular stroma⁹. A unique anatomical structure that requires special attention is the uterine torus, a small transverse thickening in the posterior part of the cervix where the uterosacral ligaments converge¹⁰.

The broad ligament, a lateral peritoneal fold that surrounds the fallopian tubes, is the most important of the various ligamentous structures that support the uterus. The fallopian tubes consist of 5 anatomically different segments: The intramural portion, the isthmus, the ampulla, the infundibulum, and the fimbriae, which are finger-like projections connected to the ovaries⁸.

The ovaries are ovoid organs, that are normally have a volume of 6-7 ml in premenopausal women. However, great variability can occur. They are located in the ovarian fossa, are supported by several ovarian ligaments and are connected to the fallopian tubes via the fimbriae. On MRI, the ovarian cortex appears hypointense on T2-weighted images, while the medulla shows intermediate to high signal intensity, reflecting its vascular and stromal composition⁷.

PATHOGENESIS AND CLINICAL MANIFESTATIONS

Despite continuous research, the exact etiology and pathophysiology of endometriosis are still not fully understood, which significantly hinders the development of definitive curative therapies. Several environmental, immunologic, genetic and endocrine risk factors have been identified, including short menstrual cycle duration, young age at menarche, low body mass index. nulliparity and congenital obstructive müllerian defects¹¹. Exposure to certain toxins such as bisphenol A and phthalates, alcohol consumption and low physical activity have also been associated with an increased risk of this condition¹². Some studies also suggest a familial predisposition, with twin studies showing a 50% heritability and an increased risk (3-15 times) in first-degree relatives with the disease¹³⁻¹⁵. Among the proposed mechanisms, the most widely accepted theory for the pathogenesis of endometriosis is the "retrograde menstrual phenomenon". This theory proposes that fragments of the endometrium migrate through the fallopian tubes into the peritoneum, implant, grow and invade the pelvic structures, leading to inflammation and fibrosis. In addition, it has been suggested that

hematogenous and lymphatic dissemination of endometrial cells may be a mechanism for the occurrence of ectopic lesions in distant organs^{16,17}.

There are various forms of the disease, including superficial peritoneal endometriosis, deep infiltrative endometriosis (DIE) and endometriomas. The clinical manifestations of patients with endometriosis vary depending on the location of the disease. Superficial peritoneal endometriosis is usually characterized by being asymptomatic, while DIE is associated with pelvic pain, dysmenorrhea, dyspareunia, urinary symptoms and infertility¹⁸. Studies have shown that there is no direct correlation between the severity of symptoms and the extent of impairment of the lesion, as some patients with full-blown disease are unaware of their condition, adding to the mystery of the disease¹⁹. It is important to consider the sensory innervation of endometriotic lesions, as deeply infiltrating lesions can affect nerve fibers, resulting in current pain¹⁸.

The definitive diagnosis of endometriosis should be made by laparoscopy. Histologic examination of the biopsied tissue should show ectopic endometrial glands and stroma²⁰. However, several international guidelines recommend a more conservative, image-based initial approach. Transvaginal ultrasound (TVUS) is considered the imaging technique of choice due to its easy accessibility and low cost. MRI is a very useful tool for diagnosis and preoperative planning as it offers better contrast resolution, and more detailed anatomy. With an overall sensitivity of 91% to 93.5% and a specificity of 86% to 87.5%, it is an excellent tool for diagnosis, mapping and preoperative planning¹¹.

The anatomical forms of presentation such as superficial peritoneal endometriosis, DIE and endometriomas show different imaging findings²¹. Endometriomas are cystic lesions of the ovary characterized by high T1 signal intensity and intermediate T2 signal intensity with the classic shading appearance, reflecting hemorrhagic content and cyclic blood breakdown. Several imaging signs have been described in large endometriomas. One of the most common signs is the "kissing ovary" sign, in which periovarian adhesions pull the ovaries together near the midline²². Another feature of endometriomas is the double level of fluid— inside the endometrioma, indicating blood in various stages of degradation within the endometrioma¹⁷.

Acute endometriosis lesions shows high T1 signal intensity but with variable T2 signal due to different bleeding and glandular contents. Chronic or fibrotic endometriosis shows low signal intensity on both T1 and T2, indicating replacement of active tissue with fibrosis and scar tissue.

MULTIMODALITY IMAGING FOR ENDOMETRIOSIS

Endometriosis requires imaging as a fundamental tool for diagnosis, disease monitoring, and preoperative planning. TVUS is the imaging modality of choice for the evaluation of suspected endometriosis because it is easily accessible, does not require ionizing radiation, has high diagnostic accuracy, and is cost-effective²³. Further advantages are the possibility of real-time assessment and its non-invasive nature²³.

The diagnostic performance of TVUS varies depending on the type and location of endometriotic lesions. A 2016 Cochrane review, which included 17 studies reported a sensitivity of 93% and specificity of 96% for the detection of endometriomas in the ovaries, while the sensitivity for DIE, was 79% and specificity 94%. Recent guidelines from the European Society of Human Reproduction and Embryology (ESHRE) recommend that imaging techniques, especially TVUS, should replace diagnostic laparoscopy as the first line of investigation due to the advantages mentioned above. Accordingly, laparoscopy is now reserved for cases where imaging is inconclusive or when therapeutic intervention is planned.

Expert-guided transvaginal ultrasound (ETVUS) is defined as a dynamic real-time ultrasound examination performed by a clinician with expertise in endometriosis. It has been shown to improve detection rates and provide better information for preoperative assessment of the extent of disease²⁴. ETVUS has a sensitivity of 77.5% for deep endometriosis, comparable to a sensitivity of 78.5% reported by Bazot et al.¹¹ in similar cohorts²⁴.

Contrast-enhanced ultrasound (CEUS) has become a complementary method in some selected cases. CEUS provides a better imaging approach to characterize endometriotic lesions by using microbubble contrast agents to assess tissue perfusion and vascular architecture in real time, especially in differentiating solid endometriotic implants from other adnexal or pelvic masses²⁵. Endometriotic nodules may have different enhancement patterns, typically showing moderate to low vascularity due to associated fibrosis and chronic inflammation. CEUS may also be helpful to detect vascular involvement in DIE or to guide targeted biopsies of atypical or suspicious lesions²⁵.

MRI ENDOMETRIOSIS PROTOCOL

The literature has shown that the MRI protocol for endometriosis should be performed in a superconducting 1.5T (Tesla) system²⁶. An axial and sagittal T2 single-shot

Table 1. MRI 1.5T and 3.0T protocol for the assessment of endometriosis

Field strength	Sequence	FOV ^a mm	Matrix	TR ms	TE ms	Flip angle, degrees	Slice thickness, mm
1.5T	Cor T2 FSE panoramic	40 × 60	468 × 468	9480	136	140	4
	Axial Dual Echo	43 × 1	288 × 160	120	2.2	85	4
	Axial DWI	40 × 40	112 × 128	8270	72	-	4
	Sag T2FSE spin eco	20 × 20	300 × 224	7.2	120	140	3
	Cor T2 FSE	20 × 20	300 × 224	7.2	120	110	3
	T1 LAVA 3D Sag	24 × 24	300 × 176	7.5	2.1	12	2.2
3.0T	Cor T2 PROPELLER	20 × 20	320 × 320	442	112	111	5
	Sag T2 FRSE	20 × 20	320 × 200	442	54.6	110	3
	Axial T2 FRSE	20 × 20	320×256	5510	112	100	3
	DWI	34 × 34	80 × 128	5510	112	-	5
	Dual Eco	36 × 36	240 × 140	5510	112	-	5
	LAVA 2D Sag	24 × 24	188 × 128	112	112	12	2.30 × 1.03

^aVaries according to the width of the patient's pelvis. MRI: magnetic resonance imaging; T: tesla; TI: time inversion; FOV: field of view; TR: time repetition; TE: time echo; ms: milliseconds; FSE: fast spin echo; FRSE: fast recovery spin echo; DWI: diffusion-weighted imaging; LAVA: liver acquisition with volume acceleration; 3D: three-dimensional; 2D: two-dimensional; PROPELLER: periodically rotated overlapping parallEL lines with enhanced reconstruction; Sag: sagittal; Cor: coronal.

fast spin echo (SSFSE) sagittal plane aligned parallel to the longitudinal axis of the uterus. In addition, the examination requires an oblique coronal and oblique axial T2-weighted Fast Recovery Fast Spin Echo (FRFSE) sequence²⁶. T2-weighted sequences without fat suppression are the preferred sequences for detecting pelvic endometriosis, as they are considered the most effective method due to their superior anatomical delineation and sensitivity to fibrotic changes²⁶.

In order to maximize the quality of the diagnostic method, preparation for the examination is crucial. We recommend that patients fast for approximately 4-6 hours prior to MRI and undergo bowel preparation to reduce peristaltic artifacts. In addition, the examination should be performed outside the patient's menstrual cycle, as this can be a confounding factor²⁶. In our institution, the protocol indicates the use of antispasmodic drugs (glucagon or hyoscine) to minimize bowel peristalsis. We also ask patients to keep the bladder full to detect endometriosis lesions near the bladder. An endovaginal gel is also inserted to dilate the vaginal canal and improve the view of the adjacent structures. Table 1 shows the MRI protocol at our institution: coronal T2-weighted images covering the entire pelvis and extending from the lesions of the kidneys to the pelvic floor; axial, sagittal, and coronal T2-weighted images; axial T1-weighted in-phase and out-of-phase images; coronal T1-weighted fat-saturated images without contrast; and post-contrast T1-weighted fatsaturated images acquired in the axial, coronal, and sagittal planes.

Several authors^{18,27,28} have proposed improved MRI protocols specifically designed for the detection of DIE. These protocols include T2-weighted images without fat suppression in the axial, coronal, and sagittal planes for a clear view of the round ligaments and pelvic region^{27,28}. The protocols also recommend T1-weighted images with fat-suppression to detect hemorrhagic foci smaller than 1 cm. T2-weighted fat-suppressed images, either in the axial or coronal plane, help to better identify small amounts of free fluid adjacent to lesions²⁸. Gadolinium contrast agent is generally discouraged as there is currently insufficient evidence of its significant added benefit¹⁸.

ENDOMETRIOSIS LOCATIONS BY COMPARTMENTS

Endometriosis in the anterolateral compartment: round ligament

The round ligament is part of the upper edge of the broad ligament, which is covered by a peritoneal fold. Its main anatomical function is to support the uterus by anchoring it to the mons pubis and labia majora via the inguinal canal. This canal obliterates physiologically between the eighth month of gestation and the first

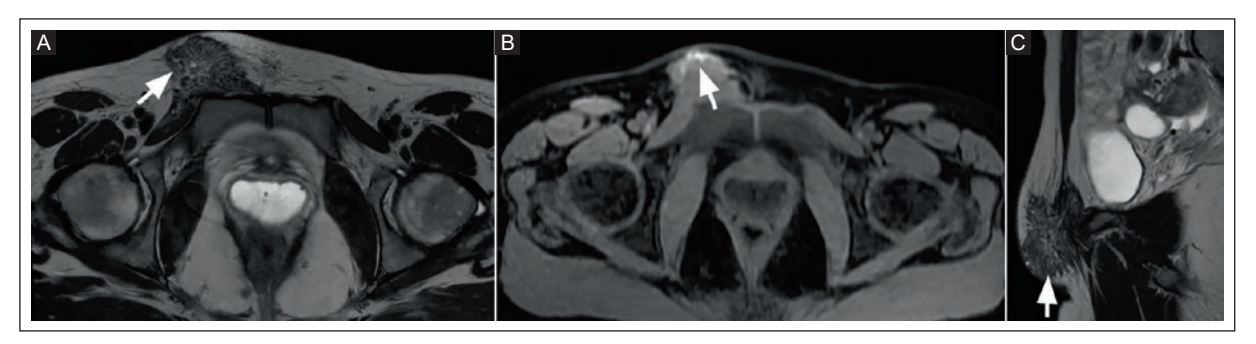


Figure 1. MRI of the pelvis of a 44-year-old woman with pelvic pain associated with the perception of a mass in the right groin. A: axial view, T2-weighted sequence shows a round, poorly defined predominantly hypointense lesion, and to a lesser extent, multiple small hyperintense regions, giving a heterogeneous appearance (white arrow). B: axial T1-weighted sequence with fat suppression, without contrast, shows hyperintense foci within the endometrial lesion (white arrow), representing a blood component. C: sagittal T2-weighted view shows fibrotic bands, with poorly defined borders (white arrow), involving the right inguinal canal. The MRI findings are consistent with the diagnosis of endometriosis of the right inguinal canal.

MRI: magnetic resonance imaging.

postnatal year. This ligament also helps to maintain the anteversion of the uterus throughout the reproductive period. The round ligament is a 10-12 cm long cord-like structure, composed of fibromuscular tissue. It is considered clinically relevant to endometriosis due to its anatomical proximity to the fallopian tubes, vessels, and nerves contained within the broad ligament^{29,30}.

On MRI, it usually appears as a thin, generally smooth, hypointense structure on T1- and T2 weighted images, extending from the uterine horns to the pelvic wall and running anterior to the external iliac vessels, which are highlighted by the surrounding fat.

Endometriosis of the round ligament is rare, with an estimated incidence of 0.3% to 0.6% of cases, most of which occur in the extrapelvic region and on the right side. Signs and symptoms may vary depending on the location of the lesion, with pain usually localized to the lower abdomen³¹. Endometriotic involvement may cause asymmetric thickening, typically larger than 1 cm, with either a smooth or nodular morphology. The segment adjacent to the uterus is most commonly affected. Figure 1 shows an MRI of the pelvis of a 44-year-old woman with pelvic pain associated with the perception of a mass in the right groin. T2-weighted images show a poorly defined heterogeneous lesion in the right inguinal canal that is predominantly hypointense. There are also irregular fibrotic bands with blurred borders suggestive of endometriotic infiltration. Hyperintense foci suggestive of blood content are seen on the T1-weighted fat-suppressed sequences without contrast. The MRI findings are consistent with the diagnosis of endometriosis of the right inguinal canal.

Endometriosis of the round ligament exhibits variable MRI signal characteristics depending on the composition of the lesion, including stromal tissue, glandular elements, hemorrhage, inflammatory reaction, or fibrosis. Purely fibrotic lesions appear hypointense on both T1- and T2-weighted images, whereas hemorrhagic foci show hyperintensity on T1-weighted and/or fat-suppressed T1-weighted sequences. However, lesions are usually a mixture of both components and visual surgical findings such as shortening, deviation or thickening of the round ligaments of the uterus (RLUs) have a high positive predictive value (83.3%) for the diagnosis of endometriosis in these ligaments; these findings may facilitate the decision to excise these ligaments¹⁸.

Although the prevalence of endometriosis in RLUs is not as high as in other structures, endometriosis in RLUs may have clinical implications for the persistence of postoperative symptoms, as comprehensive resection of all visible lesions increases the likelihood of improvement in symptoms and quality of life^{32,33}.

Endometriosis in the anteroventral compartment: bladder

Bladder endometriosis is the most common form of urinary tract involvement in endometriosis, and accounts for about 70% to 85% of genitourinary cases. However, only 1% of cases present with isolated urinary tract foci^{33,34}. This form of the disease is clinically significant as it is associated with chronic, often debilitating symptoms such as dysuria, hematuria, increased urinary frequency, and voiding dysfunction. Therefore, timely

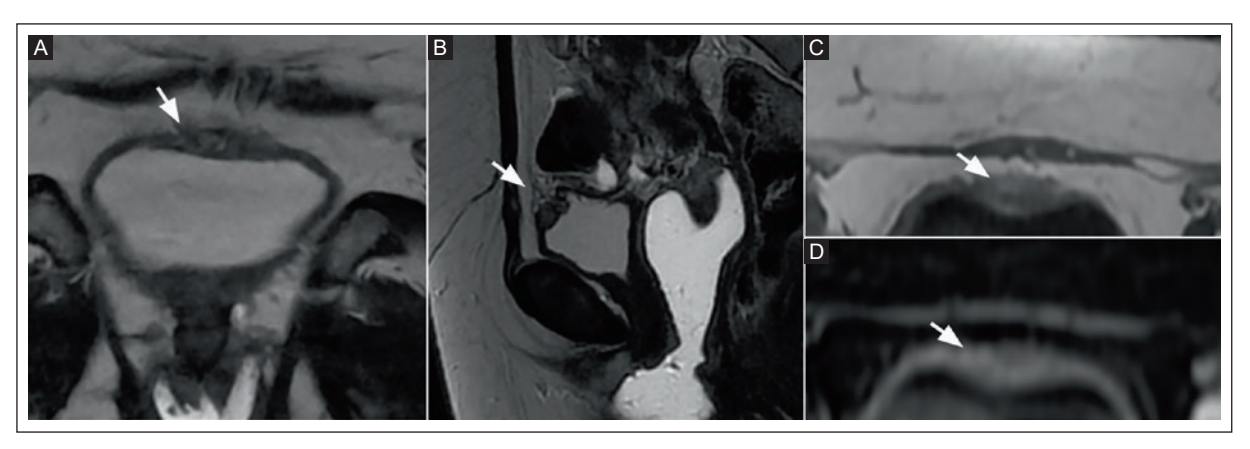


Figure 2. MRI of the pelvis of a 45-year-old woman with hypogastric pain and dysmenorrhea, who had a history of hysterectomy. A: coronal T2-weighted MRI shows a poorly defined, pseudonodular lesion in the anterior bladder wall (white arrow), extending to the bladder serosa and infiltrating the anterior perivesical fat (space of Retzius). B: sagittal T2-weighted MRI shows an irregular, predominantly hypointense lesion (white arrow) involving the bladder dome. The distended vagina is visible due to the presence of intravaginal gel. C: T1-weighted image without fat suppression showing a hypointense, pseudonodular lesion in the anterior bladder wall (white arrow). D: contrast-enhanced T1-weighted image with fat suppression shows a pseudonodular lesion of the bladder wall, that appears hyperintense due to contrast uptake (white arrow). The MRI findings are consistent with the diagnosis of DIE involving the bladder.

DIE: deep infiltrative endometriosis; MRI: magnetic resonance imaging.

imaging is required for diagnosis, as it may be associated with the risk of renal failure due to urinary tract obstruction.

In bladder endometriosis, MRI typically shows localized or diffuse wall thickening with associated signal abnormalities. Findings include nodular thickening with T2-weighted low signal intensity fibrotic stranding; sometimes, hyperintense hemorrhagic foci may be present in T1-weighted sequences. Figure 2 shows an MRI of the pelvis of a 45-year-old woman with hypogastric pain and dysmenorrhea, who had undergone a hysterectomy. On coronal T2-weighted images, the lesion extends to the bladder serosa and infiltrates the anterior perivesical fat in the Retzius space. On sagittal T2-weighted images, an irregular, predominantly hypointense lesion is seen at the level of the bladder dome with distention of the vagina due to the use of intravaginal gel. On T1-weighted images without fat suppression, the lesion is hypointense and pseudonodular, whereas contrast-enhanced T1-weighted images with fat suppression show heterogeneous hyperintensity due to contrast uptake, The MRI findings are consistent with the diagnosis of DIE involving the bladder. In most cases, lesions are confined to the serosal layer of the bladder, although extension into the muscularis propria may occur in advanced disease. The mucosa in particular is often spared, which may result in cystoscopy showing normal findings despite significant extramucosal disease.

TVUS, especially in combination with transabdominal views and bladder filling, can also help to detect endometriomas. This technique may reveal hypoechoic mural nodules or irregularities along the bladder dome or posterior wall. In some cases, loss of the normal interface between the posterior bladder wall and the anterior uterine surface may serve as an additional clue. Cystoscopy can be used to confirm mucosal involvement and rule out malignancy, although it is of limited use in detecting lesions outside the mucosa. Accurate identification of bladder endometriosis is critical for planning surgical intervention, as complete resection or partial cystectomy may be required to improve symptoms, particularly in invasive disease that is unresponsive to medical therapy.

Endometriosis of the middle central compartment: uterosacral ligament

The uterosacral ligaments are paired fibromuscular structures that extend from the posterolateral cervix and upper vagina to the anterior aspect of the sacrum, providing important support to the uterus and maintaining pelvic floor the stability. These ligaments are commonly affected in DIE, which often involves the mid-central compartment of the posterior pelvic cavity. DIE is defined as invasion > 5 mm of the peritoneal surface by endometriotic lesions, most commonly located at the uterosacral ligaments, rectovaginal space, pararectal space and vesico-uterine fold³⁵.

The most common site of DIE is the uterosacral ligaments, which are affected in up to 70% of cases³⁶. The differential diagnosis of ureteral endometriosis includes ureteral invasion by cervical cancer. On MRI, the main findings are asymmetric shortening, thickening, and nodularity involving the ligaments³⁷. Figure 3 shows an MRI of the pelvis of a 32 -year-old woman with pelvic pain and dysmenorrhea. The axial T2-weighted image shows smooth thickening of the right uterosacral ligament. The MRI findings are consistent with the diagnosis of DIE in the uterosacral ligament.

Impairment of the uterosacral ligament typically presents as fibrotic thickening with low signal on T2-weighted images, which may be spiculated, nodular, or smooth. In some cases, focal areas of high signal intensity may be present on T1-weighted images, suggesting hemorrhagic components. Although specific diameter thresholds have been proposed for the diagnosis of endometriosis of the uterosacral ligament, these are not yet well validated³⁷.

Endometriosis of the posterolateral compartment: rectovaginal septum

Endometriosis of the rectovaginal septum is a serious condition with clinical manifestations such as abdominal pain, colonic obstruction, and, in some cases, renal obstruction. The diagnostic difficulty of multifocal endometriosis begins with its similarity to other pathologies³⁸. Deep dyspareunia, dyschezia, and chronic pelvic pain are common symptoms that intensify during menstruation. In some cases, rectovaginal endometriosis may mimic irritable bowel syndrome, inflammatory bowel disease, or pelvic inflammatory disease, leading physicians to misdiagnose. A thorough clinical history, with particular attention to cyclical symptoms, is crucial to raise suspicion and prompt appropriate referral for imaging and avoid unnecessary surgery^{21,39}.

A meta-analysis found that the sensitivity and specificity of MRI for the diagnosis of rectovaginal septal endometriosis were 82% and 77%, respectively. On MRI, rectovaginal endometriosis may present as ill-defined lesions, soft tissue thickening, or obliteration of the pouch of Douglas. On MRI these lesions typically show low signal intensity on T1- and T2-weighted images with late contrast enhancement due to the fibrotic component^{40,41}. Occasionally, punctate hyperintense foci may be present on T1-weighted images, indicating subacute hemorrhage or highly viscous fluid. Figure 4 shows an MRI of the pelvis of a 39-year-old woman with chronic pelvic pain, constipation and



Figure 3. MRI of the pelvis of a 32 -year-old woman with pelvic pain and dysmenorrhea. The axial T2-weighted image shows smooth thickening of the right uterosacral ligament (white arrow). The MRI findings are consistent with the diagnosis of DIE in the uterosacral ligament.

DIE: deep infiltrative endometriosis; MRI: magnetic resonance imaging.

dyspareunia. Sagittal T2-weighted images show irregular, hypointense lesions involving the rectovaginal septum, with a distended vagina visible due to the presence of intravaginal gel. The MRI findings are consistent with the diagnosis of DIE involving the rectovaginal septum.

Although MRI is superior to other imaging modalities in the overall visualization of the pelvis, its diagnostic accuracy in the detection of superficial peritoneal lesions is limited. In this context, laparoscopy remains the gold standard for the diagnosis of superficial endometriosis and is more accurate than MRI, TVUS or physical examination for this particular subset of lesions⁴⁰.

Endometriosis of the posterior-central compartment: rectosigmoid colon

Deep endometriosis is an entity that poses a challenge for the gynecologist. The rectosigmoid colon is most commonly affected by intestinal endometriosis, which mainly affects the central posterior compartment (65.7%). In the rectum, it usually affects the middle and upper third of the organ³⁹. On MRI, endometriosis appears as T2 hypointense thickening of the muscle layer, ranging from plaque-like involvement to nodular, mass-like lesions. A classic sign of rectal involvement is the 'mushroom cap' appearance, caused by T2-hypointense fibromuscular hypertrophy of the muscularis, with wrinkling and retraction of the serosa or adventitia resembling the appearance of a mushroom. Figure 5 shows an MRI of the pelvis of a 40-year-old woman with pelvic pain and rectal bleeding during menstruation. a lesion of the mucosa of the

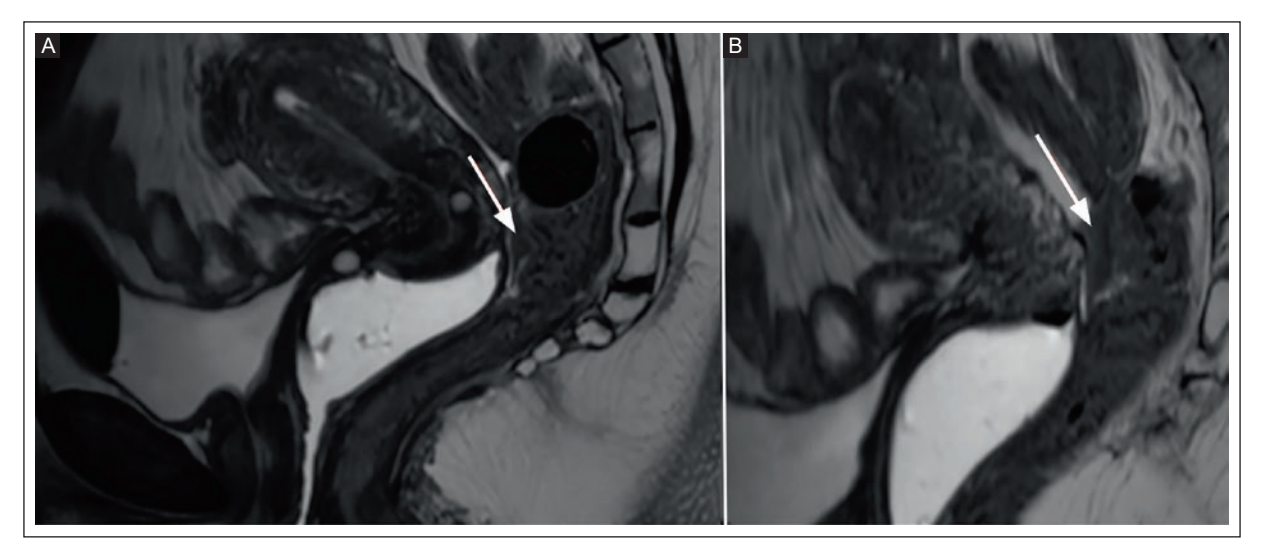


Figure 4. MRI of the pelvis of a 39-year-old woman with chronic pelvic pain associated with constipation and dyspareunia. A-B: sagittal T2-weighted MRI shows irregular, hypointense lesions involving the rectovaginal septum (white arrows). The distended vagina is visible due to the presence of intravaginal gel. The MRI findings are consistent with the diagnosis of DIE involving the rectovaginal septum.

DIE: deep infiltrative endometriosis; MRI: magnetic resonance imaging.

mid-rectum with thickening of the muscularis propria, forming the mushroom cap sign. The axial and sagittal T2-weighted MRI images show the finding of this mushroom cap lesion is a reliable predictor of infiltration of the muscularis. The MRI findings are consistent with the diagnosis of DIE with involvement of the rectosigmoid colon and show the mushroom cap sign.

A typical imaging finding for sigmoid involvement is the 'fortune cookie' sign, which appears as a T2-weighted mass with low signal intensity, central retraction, and delayed homogeneous enhancement that resembles the appearance of a fortune cookie. T1-hyperintense foci corresponding to hemorrhagic components can also be observed in the fortune cookie and mushroom cap sign⁴². Assessment of rectal segments, classified as low (< 5 cm), middle (5-10 cm), and high (> 10 cm) from the anal verge is essential when assessing the anal margin⁴².

Extrapelvic endometriosis: diaphragmatic and perihepatic

Extrapelvic endometriosis is rare and has several localizations, such as the abdominal, thoracic and hepatic capsule. The most common location of thoracic endometriosis is the diaphragm, with an incidence of 0.15% to 1.5%, followed by the pleura and lung⁴¹. Diaphragmatic endometriosis can manifest clinically as catamenial or non-catamenial pneumothorax. Initial imaging modalities include chest X-ray and computed tomography (CT);

however, MRI provides better imaging, with a reported sensitivity of 78% and specificity of 83%^{41,43}.

A catamenial pneumothorax is defined as a pneumothorax occurring three days before or after menstruation. It accounts for 3-6% of spontaneous cases in women and is associated with endometriotic diaphragmatic foci extending into the thorax. These foci can irritate and perforate the pleura. Endometriotic nodules are found in 78% of catamnestic cases. This disease mainly affects the right side (90%)⁴³.

The main challenge in the diagnosis of diaphragmatic endometriosis is its potential rarity, in addition to its asymptomatic nature, which can reach almost 70% of cases⁴⁴. When symptomatic, it manifests by pain in the arm, shoulder or right upper quadrant and is often diagnosed incidentally during surgical procedures, although the exact mechanism is still unclear⁴⁵. Some theories such as retrograde menstruation, hematogenous spread, lymphatic dissemination, and coelomic metaplasia have been proposed as possible causes⁴⁶.

On MRI, endometrial foci may appear hyperintense in all sequences. Figure 6 of an abdomino-pelvic MRI of a 36-year-old woman with dyspareunia, and dysmenorrhea and cyclic right upper quadrant pain shows a subcapsular lesion with intermediate signal intensity and internal hypointense septa on T2-weighted images. On T1-weighted fat-suppressed (LAVA) sequences, a hyperintense nodule within the lesion suggests an endometrioma with blood derivatives. Post-contrast

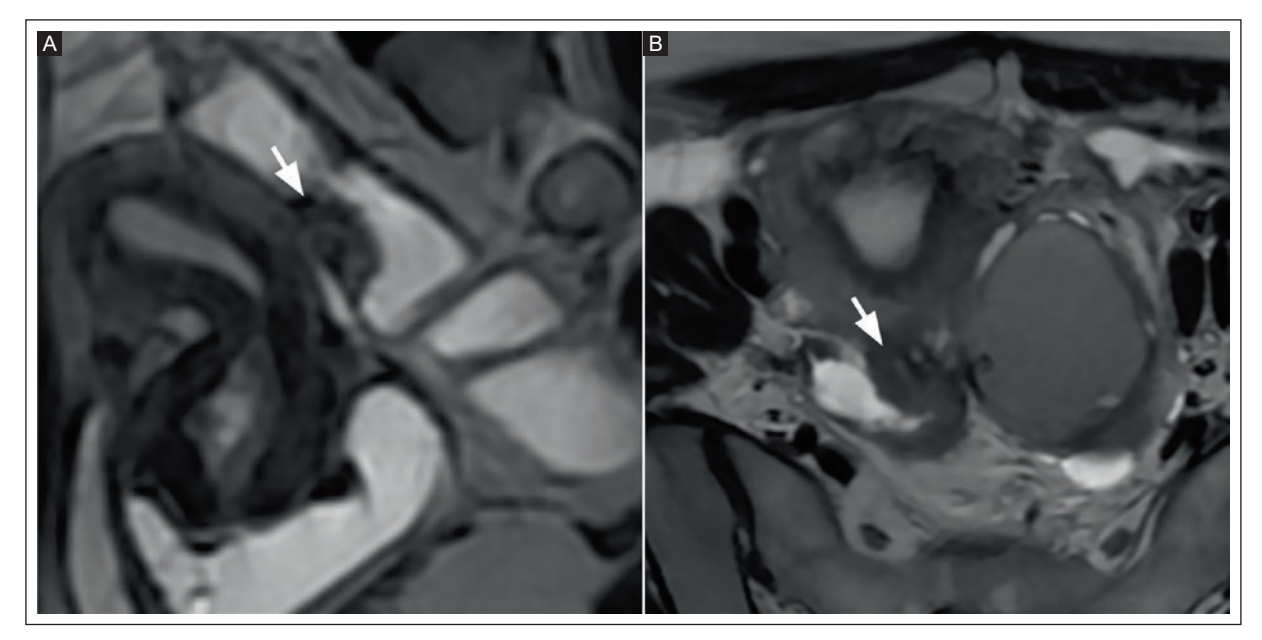


Figure 5. MRI of the pelvis of a 40 -year-old woman with pelvic pain associated with rectal bleeding during menstruation. A: sagittal and B: axial T2-weighted MRI views show a lesion of the mucosa of the mid-rectum with thickening of the muscularis propria forming the mushroom cap sign (white arrows). The distended vagina and rectum are visible due to the presence of intravaginal and intrarectal gel. The MRI findings are consistent with the diagnosis of DIE with involvement of the rectosigmoid colon and show the mushroom cap sign.

DIE: deep infiltrative endometriosis; MRI: magnetic resonance imaging.

T1-weighted imaging with subtraction shows heterogeneous enhancement of the lesion. The MRI findings are consistent with the diagnosis of extrapelvic extension of the endometriosis to the diaphragm and the perihepatic region.

Susceptibility artifacts in the thorax can lead to distortions that obscure the diagnosis due to the proximity to the air in the lungs. Recognizing the typical linear shape, that runs parallel to the diaphragm, can be helpful in distinguishing true endometriosis lesions from artifacts⁴⁷.

Extrapelvic endometriosis: sciatic nerve

Isolated, DIE of the sacral nerve roots or pelvic nerves such as the sciatic nerve is a rare entity that usually causes back pain, buttock pain with radiation to the dorsal region of the thigh and lateral aspect of the leg. Physical examination may reveal a positive Lasegue's sign, loss of sensation, reflex changes, muscle weakness and paresis¹⁸. The sciatic nerve is rarely affected by endometriosis. It is usually a case of cyclic sciatica that does not respond to the usual conservative treatment⁴⁸. Cyclic sciatica is a reactive, self-limiting inflammatory reaction to deposits and bleeding of endometrial glands and stroma in the sciatic nerve.

Early and timely diagnosis is essential, as untreated and unrecognized cases carry the risk of permanent neuronal damage if left untreated²⁷. Given the complexity of the condition, treatment requires a multidisciplinary approach, involving the specialties of gynecology, orthopedics, neurology and radiology. MRI and/or myelography are of paramount importance for preoperative assessment, especially for the localization of the lesion, which must be confirmed by immunohistochemistry²². A study by Kale et al.⁴² showed that endometriosis isolated to the sciatic nerve root is more commonly found on the right side.

MRI findings suggestive of neural involvement include neural thickening, abnormal signal intensity, and increased enhancement on contrast-enhanced MRI. Sciatic endometriosis foci can be identified by the stage of hemorrhage, as they typically have high signal intensity on T1-weighted images, and variable signal intensity on T2-weighted images⁴⁹. Figure 7 shows an MRI of the pelvis of a 36-year-old woman with chronic pelvic pain, and unilateral shooting pain that extended from the buttock down to the posterior thigh, suggesting sciatic nerve involvement. Axial T2-weighted images show an ill-defined, spiculated, hypointense lesion in the right lateral wall of the pelvis with involvement of the sciatic nerve

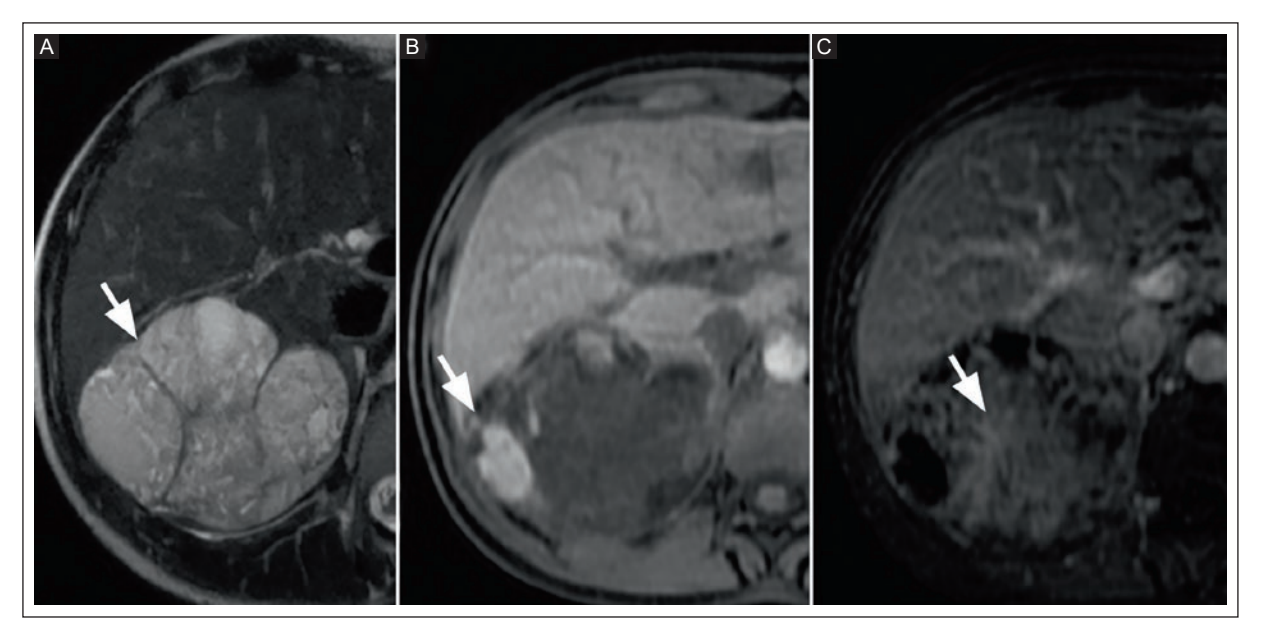


Figure 6. MRI of the abdomen and pelvis of a 36-year-old woman with right upper quadrant pain, dyspareunia, and dysmenorrhea, and cyclic right upper quadrant pain. A: T2-weighted image shows a subcapsular hepatic lesion with intermediate signal intensity and multiple internal hypointense septa (white arrow). B: T1-weighted image with fat suppression (LAVA) with a hyperintense nodule inside the lesion, showing an endometrioma with blood derivatives (white arrow). C: post-contrasted T1-weighted image with subtraction shows heterogeneous enhancement of the lesion (white arrow). The MRI findings are consistent with the diagnosis of extrapelvic extension of the endometriosis to the diaphragm and the perihepatic region.

MRI: magnetic resonance imaging; LAVA: Liver Acquisition with Volume Acceleration.

roots. The MRI findings are consistent with the diagnosis of DIE with sciatic nerve.

It is important to note that the absence of pelvic endometriosis does not exclude the diagnosis of sciatic nerve endometriosis, which emphasizes the importance of high clinical suspicion in patients. In women of child-bearing age who complain of sudden sciatic symptoms that correlate in time with the menstrual cycle and exacerbation of symptoms, nerve involvement secondary to endometriosis should be considered⁵⁰. MRI is a helpful tool in determining the cause.

ENDOVALIRM group MRI consensus lexicon and compartment-based approach

According to the ENDOVALIRM group, the pelvis can be divided into 9 compartments based on important structural landmarks⁴¹. Two horizontal lines divide the pelvis into an anterior, a middle and posterior region (Figure 8). The anterior horizontal line is drawn anterior to the cervix or vagina, while the posterior line is located anterior to the rectum. In addition, vertical lines divide the pelvis into a central, left and right compartment. These lines run from posterior to anterior, through the uterosacral ligament, the mesorectal fascia, the lateral

walls of the cervix and the bladder. This anatomical framework creates 9 compartments: right anterolateral, right mediolateral, right posterolateral, anterocentral, mediocentral, posterocentral, left anterior, left medial, and left posterior with additional extrapelvic areas⁴¹.

The Deep Pelvic Endometriosis Index (dPEI) is an MRI-based system, developed for DIE, the aims to comprehensively describe all localizations of deep endometriosis by creating structured reports with diagrams and scores. This scale is valuable for predicting operative time, length of hospital stay and possible subsequent complications, making it an excellent tool for clinical and surgical management^{22,24,41}. This scale has shown high diagnostic performance, with a sensitivity of 91% and a specificity of 90%^{22,24}. According to the dPEI, one point is awarded for each affected compartment, resulting in a total of 10 points, as extrapelvic sites are also taken into account. The severity is interpreted as follows: mild (< 2 points), moderate (3-4 points), and severe (> 5 points)⁴¹.

Although the sensitivity of MRI is considered to be better than that of TVUS or laparoscopy, its diagnostic performance varies depending on the type of endometriosis present. Accordingly, laparoscopy was found to be the better method for detecting superficial endometriosis compared to MRI, TVUS, or physical examination⁴¹.

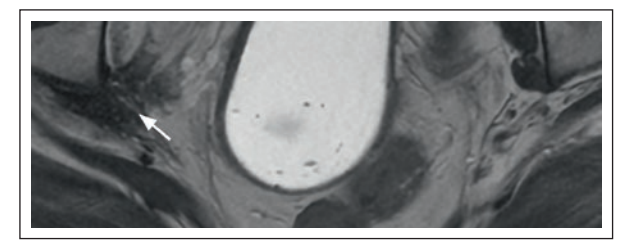


Figure 7. MRI of the pelvis of a 36-year-old woman with chronic pelvic pain, and unilateral shooting pain extending from the buttocks to the posterior thigh, suggesting involvement of the sciatic nerve. Axial T2-weighted images show an ill-defined, spiculated, hypointense lesion in the right lateral pelvic wall (white arrow) with involvement of the sciatic nerve roots. The MRI findings are consistent with the diagnosis of DIE with sciatic nerve.

DIE: deep infiltrative endometriosis; MRI: magnetic resonance imaging.

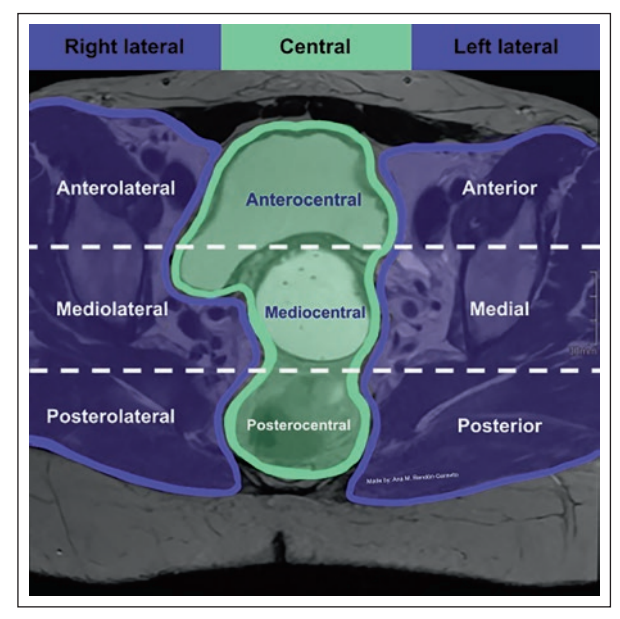


Figure 8. Anatomy of the female pelvic floor based on the MRI consensus lexicon and the compartment-based approach of the ENDOVALIRM group. The axial drawing shows two horizontal lines representing the anterior, middle and posterior compartments. There are also two vertical lines separating the right and left lateral (purple) and central (green) compartments. This anatomical framework creates 9 compartments: right anterolateral, right mediolateral, right posterolateral, anterocentral, mediocentral, posterocentral, left anterior, left medial, and left posterior with additional extrapelvic areas. MRI: magnetic resonance imaging.

CONCLUSION

Endometriosis is a disease with a wide spectrum of symptoms, signs and imaging findings, represents a major burden worldwide due to its high prevalence, debilitating effects, and usually delayed diagnosis. MRI plays an invaluable in the non-invasive assessment of

endometriosis, providing unmatched anatomical detail and sensitivity in the localization of DIE. The introduction of standardized reports and protocols for MRI, such as the MRI consensus lexicon and the ENDOVALIRM group's compartment-based approach to the assessment of dPEI, strengthens understanding between radiologists and clinicians, and provides tremendous help in surgical and clinical planning, improving patient outcomes, especially when combined with clinical findings and additional imaging modalities. It is important that radiologists are familiar with the anatomical landmarks, potential pitfalls and key imaging signs, as this is essential for disease compromise. This review highlights the key MRI features of endometriosis and emphasizes the importance of close collaboration between radiologists and clinicians to optimize the outcome for the patient.

Acknowledgment

The authors thank Professor Ana M. Contreras-Navarro for her guidance in preparing and writing this scientific paper.

Funding

The authors declare that they have not received funding.

Conflicts of interest

The authors have no conflicts of interest to disclose.

Ethical considerations

Protection of humans and animals. The authors declare that no experiments involving humans or animals were conducted for this research.

Confidentiality, informed consent, and ethical approval. The study does not involve patient personal data nor requires ethical approval. The SAGER guidelines do not apply.

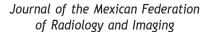
Declaration on the use of artificial intelligence. The authors declare that no generative artificial intelligence was used in the writing of this manuscript.

REFERENCES

- Alonzo L, Cannella R, Gullo G, Piombo G, Cicero G, Lopez A, et al. Magnetic resonance imaging of endometriosis: the role of advanced techniques. J Clin Med. 2024;13(19):5783. doi:10.3390/jcm13195783.
- Chaggar P, Tellum T, Thanatsis N, De Braud LV, Setty T, Jurkovic D. Prevalence of deep and ovarian endometriosis in women attending a general gynecology clinic: prospective cohort study. Ultrasound Obstet Gynecol. 2023;61(5):632-641. doi:10.1002/uog.26175.

- Dinu MD, Haj Hamoud B, Amza M, Gorecki GP, Sima RM, Gică N, et al. Endometriosis in menopausal women—A new age is coming? Literature review. Life (Basel). 2024;14(4):485. doi: 10.3390/life14040485.
- Zondervan KT, Becker CM, Koga K, Missmer SA, Taylor RN, Viganò P. Endometriosis. Nat Rev Dis Primers. 2018;4(1):9. doi: 10.1038/s41572-018-0008-5.
- Chamie L. Imaging diagnosis of endometriosis. J Mex Fed Radiol Imaging. 2022;1(3):138-150. doi:10.24875/JMEXFRI.M22000019.
- As-Sanie S, Mackenzie SC, Morrison L, Schrepf A, Zondervan KT, Horne AW, et al. Endometriosis: a review. JAMA. 2025;334(1):64-78. doi: 10.1001/jama.2025.2975.
- Ryan S, McNicholas M, Eustace SJ. Anatomy for diagnostic imaging. 3rd ed. Edinburgh: Saunders/Elsevier; 2011.
- Brüel A, Christensen El, Tranum-Jensen J, Qvortrup K, Geneser F. Geneser histología. 4th ed. Madrid: Panamericana; 2015.
- Devine C, Gardner C, Sagebiel T, Bhosale P. Magnetic resonance imaging in the diagnosis, staging, and surveillance of cervical carcinoma. Semin Ultrasound CT MR. 2015;36(4):361-368. doi:10.1053/j.sult.2015. 05 004
- Prendiville W, Sankaranarayanan R. Anatomy of the uterine cervix and the transformation zone. 1st ed. Lyon: International Agency for Research on Cancer: 2017.
- Bazot M, Daraï E. Diagnosis of deep endometriosis: clinical examination, ultrasonography, magnetic resonance imaging, and other techniques. Fertil Steril. 2017;108(6):886-894. doi: 10.1016/j.fertnstert.2017.10.026.
- Rahman MS, Park Y, Hosseinirad H, Shin JH, Jeong JW. The interplay between endometriosis and obesity. Trends Endocrinol Metab. 2025. Epub ahead of print. doi: 10.1016/j.tem.2025.03.011.
- Saha R, Pettersson HJ, Svedberg P, Olovsson M, Bergqvist A, Marions L, et al. Heritability of endometriosis. Fertil Steril. 2015;104(4):947-952. doi: 10.1016/j.fertnstert.2015.06.035.
- Seli E, Berkkanoglu M, Arici A. Pathogenesis of endometriosis. Obstet Gynecol Clin North Am. 2003;30(1):41-61. doi: 10.1016/s0889-8545(02)00052-9.
- Wang Y, Nicholes K, Shih IM. The origin and pathogenesis of endometriosis. Annu Rev Pathol. 2020;15:71-95. doi: 10.1146/annurev-pathmechdis-012419-032654
- Chapron C, Chopin N, Borghese B, Foulot H, Dousset B, Vacher-Lavenu MC, et al. Deeply infiltrating endometriosis: pathogenetic implications of the anatomical distribution. Hum Reprod. 2006;21(7):1839-1845. doi: 10.1093/humrep/del079.
- Souza D, Aráujo Jr JE, Ferreira C, Velloni F, Elias Junior J, de Barros N, et al. Imaging in endometriosis: current concepts. Curr Radiol Rep. 2022;10:393. doi: 10.1007/s40134-022-00393-x.
- Gui B, Valentini AL, Ninivaggi V, Marino M, Iacobucci M, Bonomo L, et al. Deep pelvic endometriosis: don't forget round ligaments. Review of anatomy, clinical characteristics, and MR imaging features. Abdom Imaging. 2014;39(3):622-632. doi: 10.1007/s00261-014-0091-3.
- Allaire C, Bedaiwy MA, Yong PJ. Diagnosis and management of endometriosis. CMAJ. 2023;195(10):E363-E371. doi: 10.1503/cmaj. 220637
- Zuber M, Shoaib M, Kumari S. Magnetic resonance imaging of endometriosis: a common but often hidden, missed, and misdiagnosed entity. Pol J Radiol. 2022;87:e448-e461. doi: 10.5114/pir.2022.119032.
- Fleischer K, Bachi A, Kam J, Narayanan P, Nair R, Khazali S. Bladder endometriosis: what do we know and what is left to find out? A narrative review. Best Pract Res Clin Obstet Gynaecol. 2024;96:102536. doi: 10.1016/j.bpobgyn.2024.102536.
- Hoyos LR, Johnson S, Puscheck E. Endometriosis and imaging. Clin Obstet Gynecol. 2017;60(3):503-516. doi: 10.1097/GRF.00000000000000305.
- Quesada J, Härmä K, Reid S, Rao T, Lo G, Yang N, et al. Endometriosis: a multimodal imaging review. Eur J Radiol. 2023;158:110610. doi: 10.1016/i.eirad.2022.110610.
- Fraser MA, Agarwal S, Chen I, Singh SS. Routine vs. expert-guided transvaginal ultrasound in the diagnosis of endometriosis: a retrospective review. Abdom Imaging. 2015;40(3):587-594. doi: 10.1007/s00261-014-0243-5
- Zheng Z, Zhang S, Zheng C, Wang R, Zhang Y, Chen P, et al. Qualitative and quantitative features of deep endometriosis in contrast-enhanced ultrasound: an initial experience and literature review. Clin Hemorheol Microcirc. 2023;85(1):73-82. doi: 10.3233/CH-231843.
- Foti PV, Farina R, Palmucci S, Vizzini IAA, Libertini N, Coronella M, et al. Endometriosis: clinical features, MR imaging findings and pathologic correlation. Insights Imaging. 2018;9(2):149-172. doi: 10.1007/s13244-017-0591-0.
- Sonavane SK, Kantawala KP, Menias CO. Beyond the boundaries endometriosis: typical and atypical locations. Curr Probl Diagn Radiol. 2011;40(6):219-232. doi:10.1067/j.cpradiol.2011.01.003.
- Jaramillo-Cardoso A, Shenoy-Bhangle A, Garces-Descovich A, Glickman J, King L, Mortele KJ. Pelvic MRI in the diagnosis and staging of pelvic endometriosis: added value of structured reporting and expertise. Abdom Radiol (NY). 2020;45(6):1623-1636. doi: 10.1007/s00261-019-02199-6.

- Saguintaah M, Eulliot J, Bertrand M, Prodhomme O, Béchard N, Bolivar-Perrin J, et al. Canal of Nuck abnormalities in pediatric female patients. RadioGraphics. 2022;42(2):541-558. doi:10.1148/rg.210145.
- Brainwood M, Beirne G, Fenech M. Persistence of the processus vaginalis and its related disorders. Australas J Ultrasound Med. 2020;23(1): 22-29. doi:10.1002/ajum.12195.
- VanBuren W, Feldman M, Shenoy-Bhangle AS, Sakala MD, Young S, Chamie LP, et al. Radiology state-of-the-art review: endometriosis imaging interpretation and reporting. Radiology. 2024;312(3):e233482. doi: 10.1148/radiol.233482.
- Crispi CP, de Souza CA, Oliveira MA, Dibi RP, Cardeman L, Sato H, et al. Endometriosis of the round ligament of the uterus. J Minim Invasive Gynecol. 2012;19(1):46-51. doi: 10.1016/j.jmig.2011.09.006.
- Bourgioti C, Preza O, Panourgias E, Chatoupis K, Antoniou A, Nikolaidou ME, et al. MR imaging of endometriosis: spectrum of disease. Diagn Interv Imaging. 2017;98(11):751-767. doi: 10.1016/j.diii.2017.05.009.
- Guerriero S, Ajossa S, Pagliuca M, Borzacchelli A, Deiala F, Springer S, et al. Advances in imaging for assessing pelvic endometriosis. Diagnostics (Basel). 2022;12(12):2960. doi:10.3390/diagnostics12122960.
- Mabrouk M, Raimondo D, Arena A, Iodice R, Altieri M, Sutherland N, et al. Parametrial endometriosis: the occult condition that makes the hard harder. J Minim Invasive Gynecol. 2019;26(5):871-876. doi:10.1016/j. jmig.2018.08.022.
- Moro F, Ianieri MM, De Cicco Nardone A, Carfagna P, Mascilini F, Vizzielli G, et al. Comparison of clinical and ultrasound examinations in assessing the parametria in patients with deep infiltrating endometriosis: a multicentre prospective study. Reprod Biomed Online. 2024;48(4):103733. doi:10.1016/j. rbmo.2023.103733.
- Kinkel K, Frei KA, Balleyguier C, Chapron C. Diagnosis of endometriosis with imaging: a review. Eur Radiol. 2006;16(2):285-298. doi:10.1007/ s00330-005-2882-y.
- Xiao L, White D, Kruger LF, Alwatari Y, Blackmon S, Burnett T, et al. Thoracic endometriosis syndrome: imaging findings and the value of a dedicated MRI protocol. Abdom Radiol (NY). 2025. Epub ahead of print. doi:10.1007/s00261-025-04835-w.
- Zamurovic M, Tomic A, Djordjevic K, Simanic S, Sopta J, Rasulic L, et al. Isolated deep infiltrating endometriosis of the sciatic nerve: a case report and overview of the literature. Medicina (Kaunas). 2023;59(12):2161. doi:10.3390/medicina59122161.
- Hosseiny M, Khoshpouri P, Cledera T, Brun-Vergara ML, Avalos F, Bartlett DJ. Endometriosis of the diaphragm. Radiographics. 2024;44(11): e240153. doi:10.1148/rg.240153.
- Thomassin-Naggara I, Rousset P, Touboul C, Razakamanantsoa L, Manganaro L. Reasons why it is time to change imaging guidelines on endometriosis. Eur Radiol. 2024;34(9):6175-6181. doi:10.1007/s00330-024-10595-w.
- Kale A, Baydili KNS, Keles E, Gundogdu E, Usta T, Oral E. Comparison of isolated sciatic nerve and sacral nerve root endometriosis: a review of the literature. J Minim Invasive Gynecol. 2022;29(8):943-951. doi:10.1016/ j.imiq.2022.05.017.
- Barra F, Ferrero S, Zorzi C, Evangelisti G, Perrone U, Valente I, et al. From the tip to the deep of the iceberg: parametrial involvement in endometriosis. Best Pract Res Clin Obstet Gynaecol. 2024;94:102493. doi:10.1016/j.bpobgyn.2024.102493.
- Ceccaroni M, Roviglione G, Farulla A, Bertoglio P, Clarizia R, Viti A, et al. Minimally invasive treatment of diaphragmatic endometriosis: a 15-year single referral center's experience on 215 patients. Surg Endosc. 2021; 35(12):6807-6817. doi:10.1007/s00464-020-08186-z.
- Thomassin-Naggara I, Monroc M, Chauveau B, Fauconnier A, Verpillat P, Dabi Y, et al. Multicenter external validation of the deep pelvic endometriosis index magnetic resonance imaging score. JAMA Netw Open. 2023;6(5):e2311686. doi:10.1001/jamanetworkopen.2023. 11686.
- Hirata T, Koga K, Osuga Y. Extra-pelvic endometriosis: a review. Reprod Med Biol. 2020;19(4):323-333. doi:10.1002/rmb2.12340.
- Rousset P, Rousset-Jablonski C, Alifano M, Mansuet-Lupo A, Buy JN, Revel MP. Thoracic endometriosis syndrome: CT and MRI features. Clin Radiol. 2014;69(3):323-330. doi:10.1016/j.crad.2013.10.014.
- Agarwal N, Subramanian A. Endometriosis morphology, clinical presentations and molecular pathology. J Lab Physicians. 2010;2(1):1-9. doi:10.4103/0974-2727.66699.
- Chin S, Kitzing YX, Quesada J, Lo G. Endometriosis MRI: atypical cases, pitfalls and mimics. J Med Imaging Radiat Oncol. 2024;68(4):427-433. doi:10.1111/1754-9485.13670.
- Lomoro P, Simonetti I, Nanni A, Cassone R, Di Pietto F, Vinci G, et al. Extrapelvic sciatic nerve endometriosis, the role of magnetic resonance imaging: case report and systematic review. J Comput Assist Tomogr. 2019;43(6):976-980. doi:10.1097/RCT.0000000000000916.







FULL RESEARCH ARTICLE

Five-year mortality analysis of cirrhotic Mexican patients after a transjugular intrahepatic portosystemic shunt with or without a liver transplant

Miguel A. Hinostroza-Sanchez^{1,2,3*} Guillermo A. Negrete-Gomez⁴. Miguel A. Carrillo-Martinez^{1,5}. Aldeir Fonseca-Rodriguez^{6,7}, Francisco E. Puente-Gallegos^{1,5}, Samuel E. Kettenhofen-Jimenez^{1,5,7} Laura E. Cisneros-Garza⁸, Carlos A. Rodriguez-Montalvo⁹, Francisco Bosques-Padilla⁴ and Carlos A. Cortez-Hernandez⁸

¹Department of Interventional Radiology, Hospital Zambrano Hellion, TecSalud; ²Department of Radiology and Imaging, Hospital Angeles Valle Oriente, San Pedro Garza Garcia, Nuevo Leon; 3Department of Radiology and Imaging, Hospital Christus Muguerza Alta Especialidad; 4School of Medicine and Health Sciences, Tecnologico de Monterrey; 5 Department of Interventional Radiology, Hospital San Jose, TecSalud; 6 Department of Radiology and Imaging, Hospital San Jose, TecSalud, Monterrey, Nuevo Leon; ⁷Department of Radiology and Imaging, Hospital Zambrano Hellion, TecSalud, San Pedro Garza Garcia, Nuevo Leon; 8Department of Gastroenterology, Hospital Christus Muguerza Alta Especialidad, Monterrey, Nuevo Leon; ⁹Department of Surgery, Centro de Enfermedades Hepaticas y Nutricion, Hospital Angeles Valle Oriente, San Pedro Garza Garcia, Nuevo Leon, Mexico

ABSTRACT

Introduction: The impact of a transjugular intrahepatic portosystemic shunt (TIPS) on mortality in cirrhotic patients remains controversial. Some reports show an improvement in outcome, while others indicate an increased mortality risk. This study evaluated 5-year mortality in cirrhotic patients with TIPS and compared patients with TIPS with or without liver transplantation (LT) and risk factors as predictors of mortality. Material and methods: This retrospective cohort study was conducted at two private tertiary-care hospitals from March 2014 to March 2025. Cirrhotic patients with TIPS were included. Demographic, clinical, and procedural variables were collected. Mortality was analyzed up to 5 years using Kaplan-Meier and log-rank tests. Cox proportional hazards models-both standard and time-dependent-were performed to identify mortality predictors and estimate the survival effect of TIPS alone and TIPS with LT. Results: Ninety cirrhotic patients with TIPS were included, with a mean age of 56 ± 12.5 years; 56 (62.2%) were men and 34 (37.8%) were women. The primary etiology was metabolic-associated fatty liver disease (n = 30, 33.4%), and the primary indication for TIPS was variceal bleeding (n = 52, 57.8%). The 5-year overall mortality rate was 32.3% (n = 24). Overt hepatic encephalopathy (OHE) was associated with a significantly higher 5-year mortality (60%, p = 0.001). Cirrhotic patients > 65 years had increased 5-year mortality (53.1%, p = 0.05), and this finding was the only independent predictor in the multivariable analysis (HR 1.06/year, p = 0.009). Sixteen patients (17.8%) underwent LT. No significant difference in mortality was found between cirrhotic patients with TIPS or TIPS and LT (p = 0.074). Conclusions: In this Mexican cirrhotic cohort, 5-year mortality after TIPS was 32.3%. OHE and older age were significant predictors of mortality. Cirrhotic patients with TIPS or with TIPS and LT showed comparable mortality.

Keywords: Transjugular intrahepatic portosystemic shunt. TIPS. Cirrhosis mortality. Hepatic encephalopathy. Liver transplantation.

E-mail: doc.hinostroza@gmail.com

Received for publication: 24-04-2025 Accepted for publication: 22-05-2025 DOI: 10.24875/JMEXFRI.M25000113

Available online: 10-10-2025 J Mex Fed Radiol Imaging. 2025;4(3):154-162 www.JMeXFRI.com

2696-8444 / © 2025 Federación Mexicana de Radiología e Imagen, A.C. Published by Permanyer. This is an open access article under the CC BY-NC-ND (https://creativecommons.org/licenses/by-nc-nd/4.0/).

INTRODUCTION

A transjugular intrahepatic portosystemic shunt (TIPS) is a cornerstone in the management of complications of portal hypertension^{1,2}. TIPS effectively reduces the hepatic venous pressure gradient by creating a low-resistance channel between the portal and systemic venous systems, reducing the risk of variceal bleeding, refractory ascites, hepatic hydrothorax, Budd-Chiari syndrome, portal vein thrombosis, and other portal hypertension complications¹⁻⁹. In addition, TIPS has been accepted as a bridging therapy for liver transplantation (LT) in cirrhotic patients^{4,9}.

The direct impact of TIPS on the survival of patients with cirrhosis is controversial. Some authors have demonstrated improved outcomes in carefully selected patients^{10,11}; others have highlighted the increased risk of overt hepatic encephalopathy (OHE) and procedure-related mortality, reflecting the heterogeneity of the underlying liver disease and comorbidities^{3,5,6,8,9}. Mortality after TIPS is influenced by several clinical and hemodynamic factors such as the Child-Pugh score, active bleeding, right-sided heart failure, and pulmonary hypertension, emphasizing the importance of appropriate patient selection^{1,12}.

Data on the efficacy of TIPS in preventing complications due to decompensation after the procedure have been described^{13,14}. To date, there is no conclusive evidence of a patient survival benefit after TIPS, even with the exclusive use of covered stents such as the Viatorr¹³. TIPS effectively controls portal hypertension complications. However, its association with OHE and age-related mortality with or without LT warrants further evaluation. This study evaluated 5-year mortality in cirrhotic patients after TIPS, compared patients after TIPS with or without LT, and identified risk factors as predictors of mortality.

MATERIAL AND METHODS

This retrospective cohort study was conducted from March 2014 to March 2025 in the Department of Interventional Radiology of the Hospital San Jose and Hospital Zambrano Hellion, TecSalud, a private tertiary-care institution in Monterrey, Nuevo Leon, Mexico. Patients with cirrhosis and decompensated portal hypertension who required TIPS were included. Exclusion criteria were LT before TIPS, incomplete information in the medical records, and patients who had undergone TIPS in other centers. Informed consent was not required for data collection as part of routine medical

care. The institutional ethics and research committees approved the study protocol.

Study development and variables

Patients' medical records and monthly follow-up visits after TIPS were analyzed. Age, sex, indications for the TIPS procedure, the Child-Pugh score, the Model for End-Stage Liver Disease (MELD) score, and the final portosystemic pressure gradient (PSPG) during the TIPS procedure were recorded. The referring hepatologists determined the etiology of cirrhosis by laboratory analysis and/or liver biopsy results. Cirrhotic patients with TIPS who underwent LT during the study were recorded.

Technical TIPS procedure

All TIPS procedures were performed with a RUPS-100 Transjugular Liver Access Set (Cook Medical, Bloomington, IN, USA). The corrected sinusoidal pressure was calculated as the difference between the wedged hepatic venous pressure (WHVP) and the free hepatic venous pressure, with WHVP determined in the right hepatic vein by advancing the sheath or catheter until contrast injection produced no venous reflux. Under fluoroscopic guidance, the intrahepatic puncture was directed from the right hepatic vein towards the right portal vein. Splenoportography and sizing of the shunt were performed with a 4-5F pigtail catheter, followed by tract predilatation with 6-8 mm angioplasty balloons. Bare-metal stents were used from 2004 to 2011; a Viatorr™ expanded polytetrafluoroethylene (ePTFE)-lined stent-graft endoprosthesis (W.L. Gore & Associates, Newark, DE, USA) has been used since 2012. After placement of the stent, 8-10 mm high-pressure angioplasty balloons were used until the PSPG between the portal and hepatic veins reached the target value. The inferior vena cava and right atrial pressures were also measured before sheath removal. Hemostasis was achieved by manual compression, and large-volume paracentesis was performed immediately after the procedure in patients with ascites. Figure 1 shows digital subtraction angiography after performing a TIPS in a 39-year-old man with cirrhosis and variceal bleeding. A covered stent and hepatofugal flow with multiple venous collaterals, including gastric and renal shunts, are seen. Trans-TIPS embolization of the fugal shunts was performed with helical coils and ethanol + Gelfoam®. A team of three interventional radiologists with 31 years (MCM), 11 years (FPG), and two years (SKJ) of experience performed the TIPS procedures.

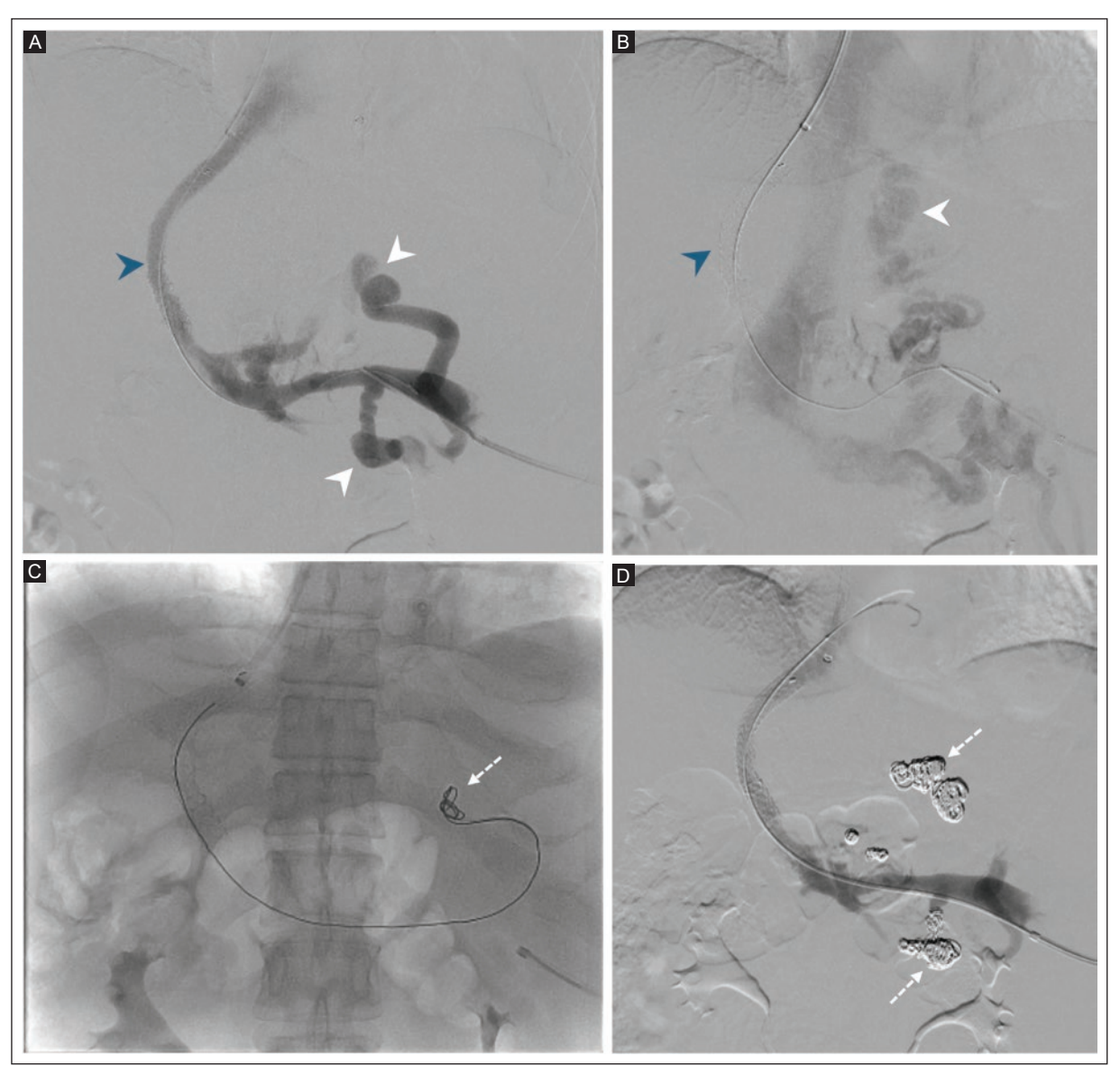


Figure 1. Digital subtraction angiography after TIPS placement in a 39-year-old man with cirrhosis and variceal bleeding. A-B: a covered stent (blue arrowheads) with hepatofugal flow, with multiple venous collaterals, and gastric and renal shunts are seen (white arrowheads). C-D: trans-TIPS embolization of the fugal shunts performed with helical coils (dashed arrows) and ethanol + Gelfoam®.

TIPS: transjugular intrahepatic portosystemic shunt.

Statistical analysis

The statistical normality of the continuous variables was determined with the Shapiro-Wilk test. Non-normal distributions are presented as median and interquartile range (IQR). Categorical data are summarized as frequencies and percentages. The primary endpoint was all-cause mortality. Mortality time, measured in years from the time of TIPS to death or last follow-up, censored patients at the time of LT. All-cause mortality was estimated using Kaplan-Meier analysis, with group

differences evaluated using the log-rank test. Multivariable Cox proportional hazards models were used to identify predictors of mortality and evaluate the effect of LT. Variables were selected for clinical relevance and univariate associations. All models were tested for proportional hazards assumptions. A standard Cox regression model was initially used to assess baseline predictors of cirrhotic patients with TIPS. To estimate the survival benefit of LT, a time-dependent Cox model treated LT patients as time-varying covariates, resulting in hazard ratios adjusted for baseline characteristics.

A two-sided p value ≤ 0.05 was significant. Statistical analysis and plotting were performed using Python (v3.13) (Python Software Foundation, Wilmington, DE, USA) with the pandas, lifelines, and matplotlib libraries.

RESULTS

A total of 101 cirrhotic patients were eligible, but eleven were excluded due to incomplete medical records or missing follow-up. A cohort of 90 cirrhotic patients with a mean age of 56 ± 12.5 years who underwent TIPS was included (Table 1). The majority were men (n = 56, 62.2%), and the most common etiology of cirrhosis was metabolic-associated fatty liver disease (n = 30, 33.4%), followed by autoimmune hepatitis (n = 16, 17.8%) and alcohol-related liver disease (n = 14, 15.6%). The main indication for TIPS was variceal bleeding (n = 52, 57.8%), followed by refractory ascites (n = 36, 40.0%). The mean MELD score at the time of the TIPS procedure was 17 \pm 7. Pre-TIPS encephalopathy was found in 21 (23.3%), and OHE was present in 14 (15.6%) of the 90 cirrhotic patients during a follow-up period of 5 years. The median final PSPG was 8 mmHg with an IQR of 6 to 10 mmHg.

Five-year overall mortality in cirrhotic patients with TIPS

The estimated all-cause mortality for the cohort after the TIPS procedure is shown in figure 2. Mortality was 15.6% at 1 year, 21.1% at 3 years, and 32.3% at 5 years.

Comparison of mortality in cirrhotic patients with TIPS with or without OHE

Cirrhotic patients with OHE had higher mortality than patients without OHE (p = 0.001) (Figure 3A). Patients with OHE had a mortality of 35.7% at 1 year, 50.0% at 3 years and 60.0% at 5 years after the TIPS procedure. In contrast, mortality in cirrhotic patients without OHE with TIPS was 11.9% at 1 year, 15.2% at 3 years, and 26.2% at 5 years.

Univariate analysis of mortality associated with age in cirrhotic patients with TIPS

A Kaplan-Meier analysis using the log-rank test was performed to identify individual factors associated with mortality (Figure 3B). Cirrhotic patients with TIPS aged ≤65 years had a mortality of 13.8% at 1 year, 18.9% at

Table 1. Characteristics of 90 cirrhotic patients with TIPS

Description	Parameter
Age, years, mean ± SD	56 ± 12.5
Sex, n (%)	
Men	56 (62.2)
Women	34 (37.8)
Etiology of cirrhosis, n (%)	
Metabolic-associated fatty liver disease	30 (33.4)
Autoimmune hepatitis	16 (17.8)
Alcohol-related liver disease	14 (15.6)
Viral hepatitis	8 (8.9)
Primary biliary cholangitis	3 (3.3)
Non-cirrhotic portal hypertension	3 (3.3)
Idiopathic	3 (3.3)
Overlap syndrome	2 (2.2)
Not classified	11 (12.2)
Indication for TIPS, n (%)	
Variceal bleeding	52 (57.8)
Refractory ascites	36 (40.0)
Hepatic hydrothorax	2 (2.2)
Child-Pugh score, n (%)	
A	13 (14.4)
В	43 (47.8)
C	34 (37.8)
MELD score, per point, mean ± SD	17 ± 7
Encephalopathy, n (%)	
PTE	21 (23.3)
OHE	14 (15.6)
Final PSPG, mmHg, median (IQR)	8 (6-10)

TIPS: transjugular intrahepatic portosystemic shunt; MELD: model for end-stage liver disease; PTE: pre-TIPS encephalopathy; PSPG: portosystemic pressure gradient; OHE: overt hepatic encephalopathy; IQR: interquartile range.

3 years and 26.5% at 5 years. In contrast, cirrhotic patients older than 65 years had increased mortality compared to younger patients, who had a mortality of 23.5% at 1 year, 30.5% at 3 years, and 53.1% at 5 years after TIPS. Patients older than 65 years had a significantly higher mortality than younger patients (p = 0.05).

A non-significant trend towards increased mortality was found in patients who underwent TIPS for variceal bleeding compared to patients with refractory ascites and hepatic hydrothorax (p = 0.09). Univariate analysis showed no significant association between other baseline characteristics and mortality. These included sex

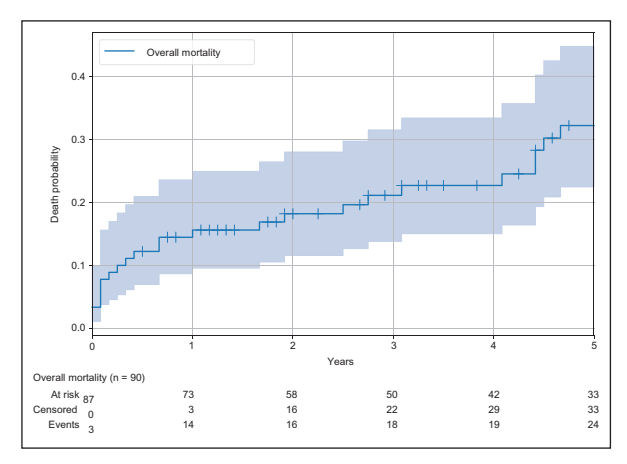


Figure 2. Estimated overall mortality of 90 cirrhotic patients with TIPS during a 5-year follow-up. Mortality was 15.6% at 1 year, 21.1% at 3 years, and 32.3% at 5 years.

TIPS: transjugular intrahepatic portosystemic shunt.

(p = 0.55), etiology of liver disease (metabolic-associated fatty liver disease vs. other, p = 0.17), a MELD score greater than 15 points (p = 0.16), or the presence of pre-TIPS encephalopathy (p = 0.19).

Multivariable analysis of mortality predictors in cirrhotic patients after TIPS

To identify independent risk factors for mortality, a multivariable Cox proportional hazards model was constructed focusing on the "TIPS-alone" therapeutic pathway. The model was fitted on the entire cohort of 90 patients. For this analysis, patient follow-up at the time of LT was censored (n = 16) (Table 2). This data corresponds to a model based on 90 subjects, including 24 deaths, with a concordance index of 0.716. After adjustment for other factors, the patient's age was the only significant independent predictor of mortality (HR: 1.06 per year; 95% CI, 1.01-1.10) (p = 0.009). This finding means that the risk of death increases 6% for each year that age increases. Although a higher MELD score was associated with an increased risk of death (HR, 1.06 per point; 95% CI, 0.99-1.13), this result did not reach statistical significance (p = 0.098). Sex and the presence of pre-TIPS encephalopathy were not significantly associated with mortality in this model.

Mortality in cirrhotic patients after TIPS compared to cirrhotic patients with TIPS and LT

A log-rank test compared cirrhotic patients with TIPS and cirrhotic patients with TIPS and LT. During the

follow-up period, 16 (17.8%) patients underwent LT. There were no significant differences in outcome between the two groups and no evidence of increased mortality (p = 0.074) (Figure 4). The overall mortality in cirrhotic patients with TIPS and LT was 12.5% over 5 years. These were treated as censored events, leaving 24 deaths for the model analysis

A time-dependent Cox regression model was constructed to directly quantify the impact of LT on survival (Table 3). This analysis correctly accounts for a patient's transition from the "pre-transplant" to the "post-transplant" state over time. The model was built on 106 patient-periods with 90 patients, in which 26 deaths occurred (Figure 5). Based on 90 subjects and 106 patient-periods and after adjusting for baseline patient characteristics, patient age was the only significant independent predictor of overall mortality in this final model (HR 1.06 per year; 95% CI, 1.02-1.10; p = 0.006).

LT in cirrhotic patients with TIPS was associated with a non-significant 52.0% reduction in the risk of death (HR, 0.48; 95% CI, 0.11-2.14; p=0.33). The wide confidence interval suggests that although a large beneficial effect of LT in cirrhotic patients with TIPS was possible, the study was underpowered to prove this with statistical certainty. The effects of the MELD score, sex, and pre-TIPS encephalopathy were not statistically significant.

DISCUSSION

In our study, the 5-year mortality in cirrhotic patients with TIPS was 32.3%. We found that OHE and older age were significantly associated with a higher 5-year mortality in these patients, regardless of whether they underwent LT. This study is the first in Mexico on a cohort of cirrhotic patients with TIPS. We believe that TIPS, a more feasible intervention in our healthcare system, should be considered as a recommended therapeutic strategy.

The reported all-cause mortality during follow-up between 1 and 10 years in cirrhotic patients with TIPS varies widely (16.8 to 67.3.%)^{2.8,15-19}. Five-year cumulative mortality and TIPS patency or dysfunction were evaluated in a retrospective single-center cohort study from Germany, including 228 cirrhotic patients with TIPS treated with ePTFE-covered stents (Viatorr®). The authors found a mortality rate of 31.3% (n = 71) at 1 year, 38.7% (n = 88) at 2 years, and a cumulative 5-year mortality of 57.3% (n = 130)¹⁶. Sonavane et al.¹⁷ conducted a prospective observational study in India of 42 patients with Budd-Chiari syndrome managed with TIPS and reported a cumulative mortality of 14% (n = 6) at 1 year,

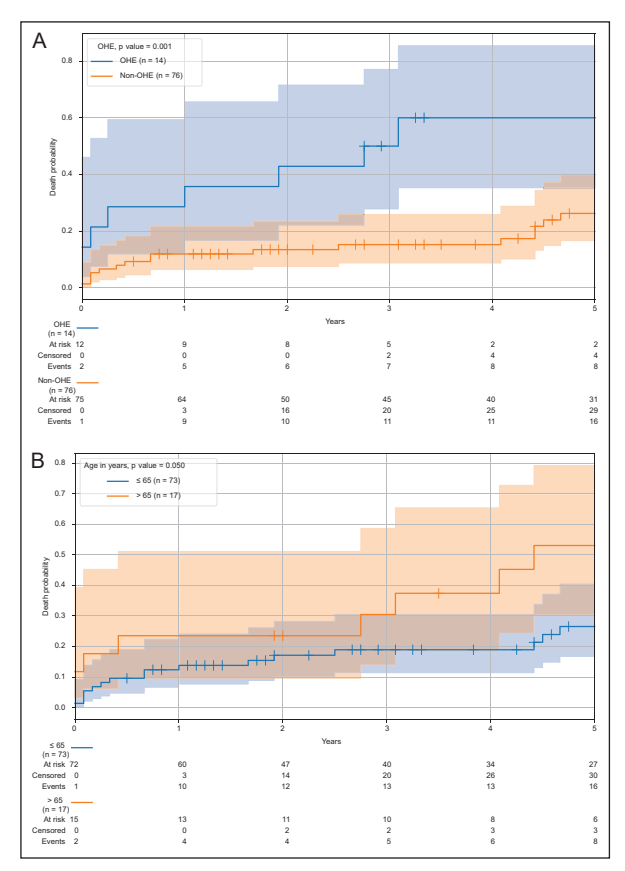


Figure 3. Mortality of cirrhotic patients with TIPS in relation to OHE and age. A: with OHE, mortality was 35.7% at 1 year, 50.0% at 3 years, and 60.0% at 5 years. Cirrhotic patients without OHE had a mortality of 11.9% at 1 year, 15.2% at 3 years, and 26.2% at 5 years. Cirrhotic patients with TIPS and OHE were significantly associated with higher mortality (p = 0.001). B: cirrhotic patients with TIPS \leq 65 years showed a mortality of 13.8% at 1 year, 18.9% at 3 years, and 26.5% at 5 years. In patients aged > 65, mortality was 23.5% at 1 year, 30.5% at 3 years, and 53.1% at 5 years. Older age was significantly associated with mortality at 5-year follow-up (p = 0.05).

OHE: overt hepatic encephalopathy; TIPS: transjugular intrahepatic portosystemic shunt.

19% (n = 8) at 5 years, and 24% (n = 10) at 10 years. Li et al.⁸ published a Chinese retrospective cohort of 132 cirrhotic patients with TIPS. They found a cumulative mortality rate of 7.6% (n = 10) at 1 year, 14.7% (n = 19) at 3 years, and 19.8% (n = 26) at 5 years. In our study, the overall 5-year mortality of 32.3% for cirrhotic patients with TIPS was consistent with internationally reported rates.

OHE is a known event after TIPS in cirrhotic patients due to shunt-induced changes in hepatic clearance of neurotoxins; however, its prognostic impact on mortality remains controversial^{3,5,8,20,21}. Nardelli et al.³ in a multicenter observational study of 614 patients with cirrhosis undergoing TIPS in three Italian hospitals found that 293 (47%) of 614 patients developed at least one

episode of OHE; 27 (9.2%) experienced recurrent/ persistent OHE. The authors concluded that an OHE episode after TIPS was not associated with mortality in patients who underwent TIPS. In contrast, Xiang et al. 20 conducted a multicenter retrospective study in 7 medical centers in China that showed the presence of OHE in 1076 (33.2%) of their 3262 cirrhotic patients with TIPS. Their study showed a mortality of 19.3% in patients with OHE. In our study, 5-year mortality was higher in patients with OHE (60.0%) than in patients without OHE (26.2%), showing a statistically significant association (p = 0.001). Our results, which are consistent with other published data 3,5,20 , showed that OHE is significantly associated with mortality and should not be underestimated as a prognostic factor.

While patient selection has traditionally relied on the severity of liver disease, such as the MELD and Child-Pugh scores, age has not been considered in most prognostic models. However, it has been shown to be an independent determinant of survival after TIPS8,22-24. Multivariate models consistently identify age as a predictor of short- and long-term mortality^{8,23,24}. This effect may be related to a reduced physiologic reserve, a higher burden of comorbid conditions, and increased susceptibility to TIPS-related complications such as OHE. Regarding age in cirrhotic patients, Ascha et al.²⁴, in a retrospective study at the Cleveland Clinic, examined 418 patients with portal hypertension undergoing TIPS. They reported a 2% increased risk of death per year with patient age (HR: 1.02, 95% Cl. 1.01-1.03. p = 0.004). The results of our study are consistent with those of Saad et al.23 and Ascha et al.24 in that older patients have a poor prognosis compared to the ≤ 65year-old Mexican population. The studies differ in the thresholds chosen for prognostic assessment, which limits the direct comparability of the results. In addition, there is no consensus on an upper age limit for TIPS in cirrhotic patients. Consequently, including age in the pre-TIPS risk assessment could improve prognosis and enable individualized decision-making, balancing the potential hemodynamic benefits against the increased mortality risk in older patients.

The role of TIPS in conjunction with LT is being investigated as the two procedures overlap in terms of patient population and prognostic factors. Pre-transplant TIPS may optimize hemodynamics, control ascites, and reduce complications related to portal hypertension at the time of LT, which could facilitate surgery and improve early postoperative stability²⁵. Mumtaz et al.²⁵, in a retrospective cohort in the United States that included 32,783 patients on a United Network for

Table 2. Multivariable Cox regression analysis^a of the predictors of mortality in cirrhotic patients with TIPS

Description	HR	95% CI	р
Age, per year	1.06	1.01-1.10	0.009
Sex, women vs. men	0.62	0.24-1.61	0.325
MELD score, per point	1.06	0.99-1.13	0.098
PTE, yes vs. no	1.43	0.55-3.70	0.462

^aThe model is based on 90 patients with 24 deaths. Concordance index = 0.716. The model fulfilled the proportional hazard assumption. TIPS: transjugular intrahepatic portosystemic shunt; MELD: model for end-stage liver disease; PTE: pre-TIPS encephalopathy; HR: hazard ratio; CI: confidence interval.

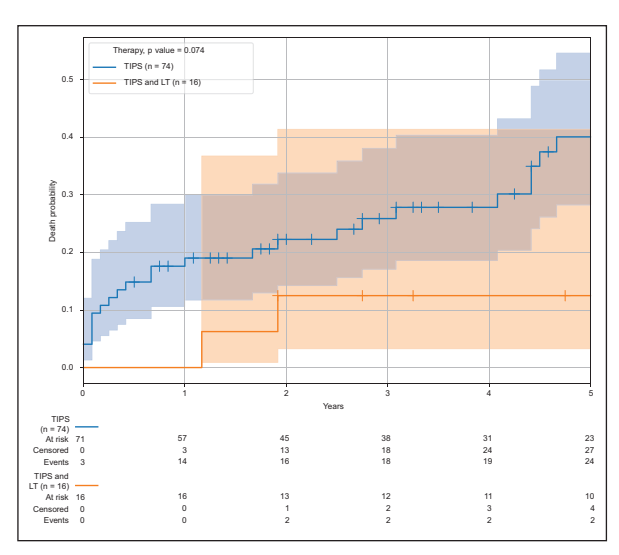


Figure 4. Cirrhotic patients with TIPS had a 5-year mortality of 40.1%. Cirrhotic patients with TIPS and LT had a 5-year mortality of 12.5% (p = 0.074). In 16 (17.8%) cirrhotic patients with TIPS who underwent LT after TIPS had a non-significant reduction of 52.0% in the risk of death. The expected survival benefit of LT in patients with cirrhosis and TIPS did not reach statistical significance.

LT: liver transplantation; TIPS: transjugular intrahepatic portosystemic shunt.

 $\begin{tabular}{ll} \textbf{Table 3.} & \textbf{Time-dependent Cox regression analysis}^a \ of \ mortality \ in cirrhotic patients with TIPS compared to patients with TIPS with or without LT \\ \end{tabular}$

Description	HR	95% CI	р
Age	1.06	1.02-1.10	0.006
Sex, women vs. men	0.52	0.21-1.29	0.160
MELD score, per point	1.05	0.99-1.12	0.100
PTE, yes vs. no	1.14	0.45-2.89	0.785
LT, as an event	0.48	0.11-2.14	0.330

^aModel based on 90 subjects and 106 patient-periods. TIPS: transjugular intrahepatic portosystemic shunt; MELD: model for end-stage liver disease; PTE: pre-TIPS encephalopathy; LT: liver transplantation; HR: hazard ratio; CI: confidence interval.

Organ Sharing (UNOS) LT waiting list, showed that 1366 (4%) had TIPS, while a subset of patients were transplanted. TIPS had no effect on 30-day mortality after LT after logistic regression (OR = 1.26; 95% CI: 0.91-1.75). Another observational study suggested a potential survival benefit in selected candidates, particularly if TIPS effectively controls pre-LT portal hypertension complications²⁶. The survival benefit of LT in cirrhotic patients after TIPS is not statistically proven, probably due to the relatively small number of transplanted patients and the fact that many TIPS studies censor outcomes at the time of LT^{20,22-24}. In a Mexican LT cohort of 92 patients described by Hinojosa-Gonzalez et al.27, 9% (n = 9) had a TIPS before LT; similar mortality rates were found when comparing the TIPS group with the non-TIPS group over 2 years. Heinzow et al.28, in a retrospective single-center study conducted at a tertiary-care referral center in Germany that included 88 patients who underwent TIPS, 8 (10%) had LT. Survival in patients with TIPS before LT of more than 5 years improved in a univariate analysis (p = 0.024), but it was not an independent predictor in multivariate models. Our findings align with the existing literature, showing that LT after TIPS improves patient survival²⁰⁻²⁴. In our cohort, 16 (17.8%) patients who underwent LT after TIPS had a non-significant 52.0% reduced risk of death (HR, 0.48; 95% CI, 0.11-2.14; p = 0.33). Although this result is consistent with the expected survival benefit of LT in patients with cirrhosis and TIPS, the effect did not reach statistical significance. It may be underestimated due to the small sample size and the presence of competing risk factors for mortality.

This study has several strengths. First, it addresses the clinical relevance of TIPS in the Mexican population, a setting for which few data are available. Second, the procedure was performed using a standardized technique by an experienced interventional radiology team, ensuring consistency between cases. Third, validated statistical methods, such as Cox proportional hazards analysis and Kaplan-Meier analysis, were employed to evaluate survival and risk factors, enabling a comprehensive assessment of outcomes in cirrhotic patients with TIPS.

This study also has limitations that need to be considered. The small sample size and the retrospective nature of the study have the potential for selection bias. The lack of a control group without TIPS limits a direct comparison of the results with those of standard of care. There may also be exclusion bias, as patients from remote areas or lower socioeconomic backgrounds often have limited access to healthcare. This fact reflects the general inequalities in access to

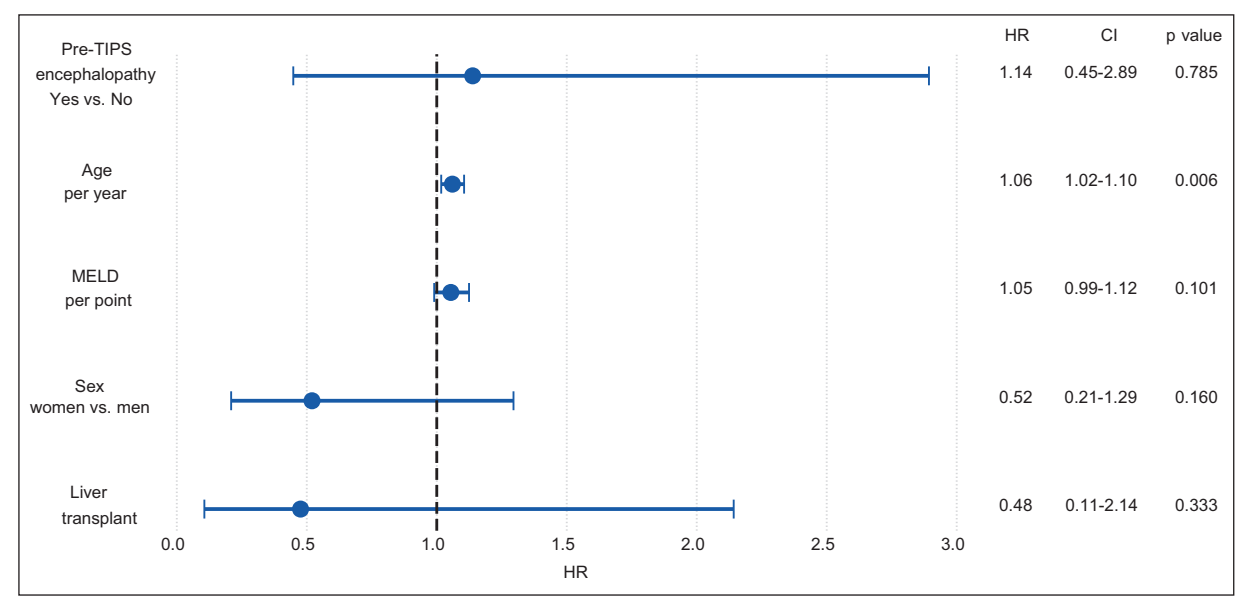


Figure 5. Time-varying covariate analysis. In this model, patient age remains the only significant independent predictor of overall 5-year mortality (HR,1.06 per year; 95% CI, 1.02-1.10; p = 0.006).

LT: liver transplantation; TIPS: transjugular intrahepatic portosystemic shunt; MELD: model for end-stage liver disease; HR: hazard ratio; CI: confidence interval.

advanced procedures such as TIPS within the Mexican public health system, where high costs limit availability. Finally, the study relied on a dichotomous definition of OHE, which may not fully capture the clinical spectrum of this complication. Some recognized predictors of mortality in cirrhotic patients with TIPS were not available due to missing data. On the other hand, the LT analysis was limited by the small number of procedures during the follow-up period.

CONCLUSION

In our study, the 5-year mortality rate for cirrhotic patients with TIPS was 32.3%. Mortality was significantly associated with OHE and older age. We found no significant difference in outcomes in cirrhotic TIPS patients with or without a LT. Our findings are consistent with international mortality rates for TIPS patients and support the use of prognostic factors for monitoring and assessing mortality risk. Further prospective studies with control groups are needed to determine the survival impact of TIPS on cirrhotic patients with and without a LT.

Acknowledgment

The authors thank Professor Ana M. Contreras-Navarro for her guidance in preparing and writing this scientific paper.

Funding

The authors declare that they have not received funding.

Conflicts of interest

The authors declare no conflicts of interest.

Ethical considerations

Protection of humans and animals. The authors declare that the procedures followed complied with the ethical standards of the responsible human experimentation committee and adhered to the World Medical Association and the Declaration of Helsinki (1964). The procedures were approved by the institutional Ethics Committee.

Confidentiality, informed consent, and ethical approval. The authors have obtained approval from the Ethics Committee for the analysis of routinely obtained and anonymized clinical data, so informed consent was not necessary.

Declaration on the use of artificial intelligence. The authors declare that no generative artificial intelligence was used in the writing of this manuscript.

REFERENCES

- Garcia-Pagán JC, Di Pascoli M, Caca K, Laleman W, Bureau C, Appenrodt B, et al. Use of early-TIPS for high-risk variceal bleeding: results of a post-RCT surveillance study. J Hepatol. 2013;58(1):45-50. doi: 10.1016/ j.jhep.2012.08.020.
- Kurmis TP. Transjugular intrahepatic portosystemic shunt: an analysis of outcomes. ANZ J Surg. 2009;79(10):745-749. doi: 10.1111/j.1445-2197. 2009.05093.x.
- Nardelli S, Riggio O, Marra F, Gioia S, Saltini D, Bellafante D, et al. Episodic overt hepatic encephalopathy after transjugular intrahepatic portosystemic shunt does not increase mortality in patients with cirrhosis. J Hepatol. 2024;80(4):596-602. doi: 10.1016/j.jhep.2023.11.033.
- Dissegna D, Sponza M, Falleti E, Fabris C, Vit A, Angeli P, et al. Morbidity and mortality after transjugular intrahepatic portosystemic shunt placement in patients with cirrhosis. Eur J Gastroenterol Hepatol. 2019;31(5):626-632. doi: 10.1097/MEG.000000000001342.
- Chen B, Wang J, Sheng W, Ma B, Xu P, Cheng X, et al. Prognosis of LSPD versus TIPS for the treatment of esophagogastric variceal bleeding in cirrhosis. Surg Endosc. 2024;38(4):2106-2115. doi: 10.1007/s00464-024-10729-7.
- Geschwind JFH, Dake MD. Abrams' angiography: interventional radiology.
 3rd ed. Philadelphia PA, USA. Wolters Kluwer Health Lippincott Williams & Wilkins; 2014.
- Del Rio-Gonzalez M, Carrillo-Martinez MA, Puente-Gallegos FE, Kettenhofen-Jimenez SE, Cisneros-Garza LE, Rodriguez-Montalvo CA, et al. Transjugular intrahepatic portosystemic shunt in a private Mexican medical setting: Indications and hemodynamic and technical outcomes. J Mex Fed Radiol Imaging. 2024;3(3):175-181. doi: 10.24875/JMEXFRI. M24000077.
- Li K, Cheng Y, Zhao R, Jiang H, Zhang L, Tong Y, et al. Prediction of mortality and overt hepatic encephalopathy undergoing transjugular intrahepatic portosystemic shunt: a retrospective cohort study. Abdom Radiol. 2023;49(3):908-918. doi: 10.1007/s00261-023-04086-7.
- Larrue H, D'Amico G, Olivas P, Lv Y, Bucsics T, Rudler M, et al. TIPS prevents further decompensation and improves survival in patients with cirrhosis and portal hypertension in an individual patient data metaanalysis. J Hepatol. 2023;79(3):692-703. doi: 10.1016/j.jhep.2023.04.028.
- Ter Borg PCJ, Hollemans M, Van Buuren HR, Vleggaar FP, Groeneweg M, Hop WCJ, et al. Transjugular intrahepatic portosystemic shunts: longterm patency and clinical results in a patient cohort observed for 3–9 years. Radiology. 2004;231(2):537-545. doi: 10.1148/radiol.2312021797.
- Woerner AJ, Šhin DS, Chick JFB, Koo KSH, Hsu EK, Tang ER, et al. Transjugular intrahepatic portosystemic shunt creation may be associated with hyperplastic hepatic nodular lesions in the long term: an analysis of 18 pediatric and young adult patients. Pediatr Radiol. 2021;51(8):1348-1357. doi: 10.1007/s00247-021-05010-1.
- Gaba RC, Parvinian A, Casadaban LC, Couture PM, Zivin SP, Lakhoo J, et al. Survival benefit of TIPS versus serial paracentesis in patients with refractory ascites: a single institution case-control propensity score analysis. Clin Radiol. 2015;70(5):e51-e57. doi: 10.1016/j.crad.2015. 02.002.
- Huang Y, Wang X, Li X, Sun S, Xie Y, Yin X. Comparative efficacy of early TIPS, Non-early TIPS, and Standard treatment in patients with cirrhosis and acute variceal bleeding: a network meta-analysis. Int J Surg. 2024;110(2):1149-1158. doi: 10.1097/JS9.00000000000000865.
- 14. Xu X, Tang C, Linghu E, Ding H, Chinese Society of Hepatology, Chinese Medical Association; Chinese Society of Gastroenterology, Chinese Medical Association; Chinese Society of Digestive Endoscopy, Chinese Medical Association Guidelines for the Management of Esophagogastric Variceal Bleeding in Cirrhotic Portal Hypertension. J Clin Transl Hepatol. 2023;11(7):1565-1579. doi: 10.14218/JCTH.2023.00061.

- Zhao Y, Yang Y, Lv W, Zhu S, Chen X, Wang T, et al. A modified model for predicting mortality after transjugular intrahepatic portosystemic shunt: a multicentre study. Liver Int. 2024;44(2):472-482. doi: 10.1111/ liv.15790.
- Klinger C, Riecken B, Müller J, Westphal A, Löffler J, Froehlich E, et al. Doppler ultrasound surveillance of TIPS-patency in the era of covered stents – retrospective analysis of a large single-center cohort. Z Für Gastroenterol. 2018;56(09):1053-1062. doi: 10.1055/s-0044-102107.
- Sonavane AD, Amarapurkar DN, Rathod KR, Punamiya SJ. Long term survival of patients undergoing TIPS in Budd-Chiari syndrome. J Clin Exp Hepatol. 2019;9(1):56-61. doi: 10.1016/j.jceh.2018.02.008.
- Artru F, Miquet X, Azahaf M, Labreuche J, Ntandja Wandji LC, Sergent G, et al. Consequences of TIPSS placement on the body composition of patients with cirrhosis and severe portal hypertension: a large retrospective CT-based surveillance. Aliment Pharmacol Ther. 2020;52(9):1516-1526. doi: 10.1111/apt.16080.
- Swersky A, Borja-Cacho D, Deitch Z, Thornburg B, Salem R. Portal vein recanalization-transjugular intrahepatic portosystemic shunt (PVR-TIPS) facilitates liver transplantation in cirrhotic patients with occlusive portal vein thrombosis. Semin Interv Radiol. 2023;40(01):38-43. doi: 10.1055/s-0043-1764409.
- Xiang Y, Tie J, Wang G, Zhuge Y, Wu H, Zhu X, et al. Post-TIPS overt hepatic encephalopathy increases long-term but not short-term mortality in cirrhotic patients with variceal bleeding: a large-scale, multicenter real-world study. Aliment Pharmacol Ther. 2025;61(7):1183-1196. doi: 10.1111/apt.18509.
- Barton R, Rösch J, Saxon R, Lakin P, Petersen B, Keller F. TIPS: shortand long-term results: a survey of 1750 patients. Semin Interv Radiol. 1995;12(04):364-367. doi: 10.1055/s-0028-1082233.
- Piecha F, Vonderlin J, Frühhaber F, Graß JK, Ozga AK, Harberts A, et al. Preoperative TIPS and in-hospital mortality in patients with cirrhosis undergoing surgery. JHEP Rep. 2024;6(1):100914. doi: 10.1016/j.jhepr. 2023.100914.
- Saad N, Rude MK, Darcy M, Hanin JB, Wentworth A, Korenblat KM. Older age is associated with increased early mortality after transjugular intrahepatic portosystemic shunt. Ann Hepatol. 2016;15(2):215-221. doi: doi.org/10.5604/16652681.1193716.
- 24. Ascha M, Abuqayyas S, Hanouneh I, Alkukhun L, Sands M, Dweik RA, et al. Predictors of mortality after transjugular portosystemic shunt. World J Hepatol. 2016;8(11):520. doi: 10.4254/wjh.v8.i11.520.
- Mumtaz K, Metwally S, Modi RM, Patel N, Tumin D, Michaels AJ, et al. Impact of transjugular intrahepatic porto-systemic shunt on post liver transplantation outcomes: study based on the United Network for Organ Sharing database. World J Hepatol. 2017;9(2):99. doi: 10.4254/wjh.v9. i2.99.
- Tejedor-Tejada J, Fuentes-Valenzuela E, García-Pajares F, Nájera-Muñoz R, Almohalla-Álvarez C, Sánchez-Martín F, et al. Long-term clinical outcome and survival predictors in patients with cirrhosis after 10-mm-covered transjugular intrahepatic portosystemic shunt. Gastroenterol Hepatol. 2021;44(9):620-627. doi: 10.1016/j.gastrohep.2020.10.018.
- Hinojosa-González DE, Baca-Arzaga A, Salgado-Garza G, Roblesgil-Medrano A, Herrera-Carrillo FE, Carrillo-Martínez MÁ, et al. Seguridad operatoria en trasplante hepático ortotópico en pacientes con previa derivación portosistémica intrahepática transyugular: experiencia de 20 años. Rev Gastroenterol México. 2024;89(1):4-10. doi: 10.1016/j.rgmx.2021.11.011.
- Heinzow H, Lenz P, Köhler M, Reinecke F, Ullerich H, Domschke W, et al. Clinical outcome and predictors of survival after TIPS insertion in patients with liver cirrhosis. World J Gastroenterol. 2012;18(37):5211-5218. doi: doi:10.3748/wjq.v18.i37.5211.





FULL RESEARCH ARTICLE

Thalamic atrophy correlates with white matter lesion metrics in Mexican patients with multiple sclerosis: an automated MRI volumetry analysis

Eduardo Torres-Olivas*, Rodrigo I. Brito-Delgado, Arturo Hernandez-Medina, and Francisco Avala-Ochoa

Department of Magnetic Resonance, Angeles Lomas Hospital, Huixquilucan, State of Mexico, Mexico

ABSTRACT

Introduction: Magnetic resonance imaging (MRI) can be used to quantify white matter lesion (WML) metrics and volumetric changes in patients with multiple sclerosis (MS). The thalamus is particularly vulnerable in MS progression. This study aimed to explore the correlation between the normalized volume of the total brain, thalamus, and caudate nucleus with WML metrics in Mexican MS patients using automated MRI volumetry. Materials and methods: This cross-sectional study included MRI scans of patients with MS, using 3D-T1 and 3D fluid-attenuated inversion recovery (FLAIR) sequences processed with the automated volBrain system. The normalized volume of the total brain, thalamus, caudate nucleus, and WML metrics such as quantity, normalized volume, and burden were assessed. Sex- based comparisons and Spearman correlation analyses were conducted. Results: MRI scans of 40 Mexican MS patients—29 women (72.5%) and 11 men (27.5%)—with a mean age of 44.6 ± 12.0 years were evaluated. A significant negative correlation was found between thalamic atrophy and WML metrics, WML quantity (r = -0.41; p = 0.009), normalized WML volume (r = -0.52; p < 0.001) and WML burden (r = -0.54; p < 0.001); the higher the quantity, volume, and burden of WML, the lower the normalized thalamic volume. WML burden had the strongest correlation with thalamic atrophy. No significant correlation was found between thalamic atrophy and the quantity, volume, and burden of WML in patients with MS. This study is the first in Mexican MS patients that uses an Albased segmentation and volumetry tool to establish a correlation between thalamic atrophy and WML metrics.

Keywords: Magnetic resonance imaging. Multiple sclerosis. Brain volumetry. White matter. Thalamic atrophy. Automated segmentation.

INTRODUCTION

Multiple sclerosis (MS), a progressive disease of the central nervous system, is characterized by immune-mediated demyelination and neurodegeneration. Magnetic resonance imaging (MRI) plays a central role in clinical practice, allowing detailed assessment of brain volume changes and white matter lesion metrics¹. The extent of T2 hyperintense white matter lesions is

quantified in several ways: as a quantity, an absolute volume, or a normalized volume, either in terms of total intracranial volume (TIV) or total white matter volume (TWMV). The normalized WML volume is the preferred method because TIV normalization accounts for head size variations for brain volume comparisons. TWMV normalization accounts for white matter tissue loss, allowing a more accurate lesion burden comparison²⁻⁴.

Machine learning techniques have revolutionized MRI post-processing, outperforming manual evaluations in segmentation accuracy^{1,5,6}. Moreover, in combination with high-resolution 3T MRI acquisitions and ultrahigh-field 7T MRI, these techniques improve focal damage and volumetric shift detection^{7,8}. There are several automated volumetric MRI analysis platforms, such as FreeSurfer (Laboratory for Computational Neuroimaging. Cambridge, MA, USA), and FIRST (FMRIB Software Library-FSL, University of Oxford, Oxford, UK)8. These tools are robust and widely validated; however, they require advanced computing resources and high user expertise. In contrast, the volBrain platform (Universidad Politecnica de Valencia, Valencia, Spain, and Centre National de la Recherche Scientifique [CNRS], Paris, France) is an open-access, online tool with a userfriendly interface and fully automated processing pipelines. It requires no local installation, no special hardware, and no advanced technical knowledge. In addition, the volBrain platform has high performance, consistency, and accuracy in segmenting subcortical structures and assessing regional atrophy metrics9.

The thalamus, an important brain network hub, is particularly vulnerable in MS. Thalamus atrophy is a reliable indicator of progressive neurodegeneration associated with motor and cognitive dysfunction¹⁰. The relationship between WML accumulation and thalamic volume is partially understood⁸. Most available data on the current state of research come from European and North American cohorts,^{1,5} leading to a significant evidence gap in underrepresented populations such as Mexican MS patients. This study aimed to explore the correlation between normalized total brain, thalamic, and caudate nucleus volume with WML metrics such as quantity, normalized volume, and burden in Mexican MS patients using the volBrain platform for MRI analysis based on automated brain volumetry and segmentation.

MATERIAL AND METHODS

This cross-sectional study was conducted from March to November 2024 in the Department of Magnetic Resonance of the Angeles Lomas Hospital in Huixquilucan, State of Mexico, Mexico. MS patients who underwent a brain MRI scan were included. Low quality MRI scans were excluded based on the segmentation and volumetry reports. Informed consent was not required for this observational study of information collected during routine clinical care. The Institutional Research and Ethics in Research Committees approved the study.

Study development and variables

Data were obtained from clinical records. Age, sex, normalized total brain, thalamic, and caudate nucleus volumes, and WML quantity, normalized WML volume, and WML burden were recorded.

Definitions¹¹

Normalized total brain volume: normalized in relation to the total intracranial volume (TIV), expressed as a percentage.

Normalized thalamic volume: normalized in relation to the TIV, expressed as a percentage.

Normalized caudate nucleus volume: normalized in relation to the TIV, expressed as a percentage.

WML quantity: number of white matter lesions.

Normalized WML volume: space occupied by white matter lesions, divided by the TIV, expressed as a percentage.

WML burden: space occupied by white matter lesions, divided by TWMV, expressed as a percentage.

Image acquisition and processing

A 1.5T MAGNETOM Aera and a 3T MAGNETOM Skyra Fit MRI (Siemens Healthineers, Erlangen, Germany) scanners were used. All images were acquired with a 32-channel head coil. T1-MPRAGE and volumetric FLAIR sequences with standard clinical acquisition parameters were used (Table 1). For the 1.5T scanner, T1-MPRAGE (TR/TE 2200/2.67 ms) and SPACE FLAIR (TR/TE/TI 5000/335/1600 ms) sequences with 1.0 mm isometric voxels were used. For the 3T scanner, T1-MPRAGE (TR/TE 2300/2.32 ms) and SPACE FLAIR (TR/TE/TI 7000/395/2050 ms) sequences with isometric voxels of 0.9 mm were used.

The images were anonymized, exported, and converted to the Neuroimaging Informatics Technology Initiative (NIFTI) format for analysis (Figure 1). Automated brain volumetry and segmentation were performed with the open-access online platform volBrain¹¹ using the DeepLesionBrain pipeline based on convolutional neural networks⁶. Figure 2 shows an NIfTI-formatted brain MRI with structural volumetry and WML segmentation by the algorithm. It illustrates the work performed automatically and highlights thalamus and caudate nucleus segmentation as well as periventricular and deep WML segmentation in the coronal and sagittal planes.

A report is generated after the pipeline process. The normality or abnormality of the total brain, thalamus,

Field strength	Sequence	TI (ms)	FOV (mm)	Matrix	TR (ms)	TE (ms)	Magnetic preparation (ms)	Flip angle (degrees)	Slice thickness (mm)
1.5T	T1-MPRAGE 3D	No	250*250	256*256	2200	2.67	900	8	1.0
	SPACE-FLAIR 3D	1600	260*260	220*256	5000	335	125	120-90	1.0
3T	T1-MPRAGE 3D	No	240*240	256*256	2300	2.32	900	8	0.9
	SPACE-FLAIR 3D	2050	230*230	256*256	7000	395	125	120-90	0.9

Table 1. Brain MRI 1.5T and 3T protocol for total brain, thalamus, and caudate nucleus segmentation and volumetry

MRI: magnetic resonance imaging; T: Tesla; MPRAGE: magnetization-prepared rapid gradient echo; SPACE: sampling perfection with application optimized contrasts using different flip-angle evolutions; FLAIR: fluid attenuated inversion recovery; TI: inversion-recovery time; FOV: field of view; TR: time repetition; TE: time echo; ms: milliseconds.

caudate nucleus, and WML metrics was determined for each patient using the expected cut-off values of normalized volume (95% confidence interval) as a function of sex and age for each measurement for reference purposes. Values outside the cut-off were highlighted.

Statistical analysis

Normally distributed variables were expressed as means and standard deviations (SD). Non-parametric variables were expressed as medians and interquartile range (IQR). The normality of the distribution of quantitative variables was assessed with the Shapiro-Wilk test. Qualitative variables were expressed as absolute and relative frequencies. Comparisons between women and men were performed with Student's t-test for normally distributed variables. Non-parametric variables were analyzed with the Mann-Whitney U-test. Spearman correlation coefficients between the WML metrics and the normalized volumes of the total brain, thalamus, and caudate nucleus were determined. The p value < 0.05 was statistically significant. The analysis was performed with RkWard v0.8.0 (Friedrichsmeier, 2024)¹².

RESULTS

Forty MS patients with a mean age of 44.6 \pm 12.0 years; 29 (72.5%) women and 11 (27.5%) men were included (Table 2). The mean normalized total brain volume was 85.0% \pm 2.9%, the mean normalized thalamic volume was 1.1% \pm 0.09%, and the mean normalized caudate nucleus volume was 0.4% \pm 0.05%. The median WML quantity was 29 lesions per patient (IQR of 25); the median and IQR normalized WML volumes were 0.19% and 0.32%, respectively, while the median WML burden was 0.71% and 1.25%, respectively.

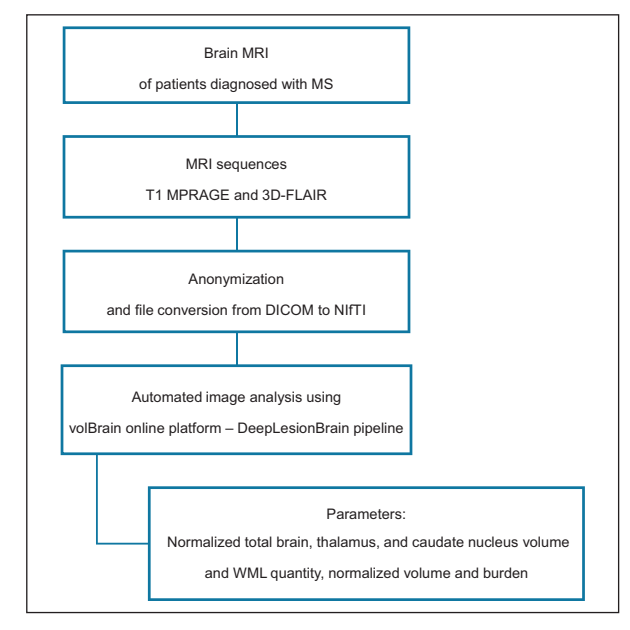


Figure 1. MRI-based brain volumetry and WML analysis workflow in MS patients. The process starts with brain MRI acquisition with T1 MPRAGE and 3D-FLAIR sequences, followed by data anonymization and file conversion from DICOM to NIfTI format and uploading to the volBrain online platform. The parameters evaluated were the normalized total brain, thalamus, and caudate nucleus volumes, and WML quantity, normalized WML volume, and WML burden.

MRI: magnetic resonance imaging; MS: multiple sclerosis; MPRAGE: magnetization prepared rapid gradient echo; 3D-FLAIR: three-dimensional fluid-attenuated inversion recovery; DICOM: digital imaging and communications in medicine; NIfTI: Neuroimaging Informatics Technology Initiative; WML: white matter lesion; TWMV: total white matter volume.

Comparison of the normalized volume of the total brain, thalamus, and caudate nucleus and WML metrics between women and men with MS

The mean normalized total brain volume was 82.11% in women and 84.9% in men (Table 3). The mean normalized thalamic volume was 1.11% in women

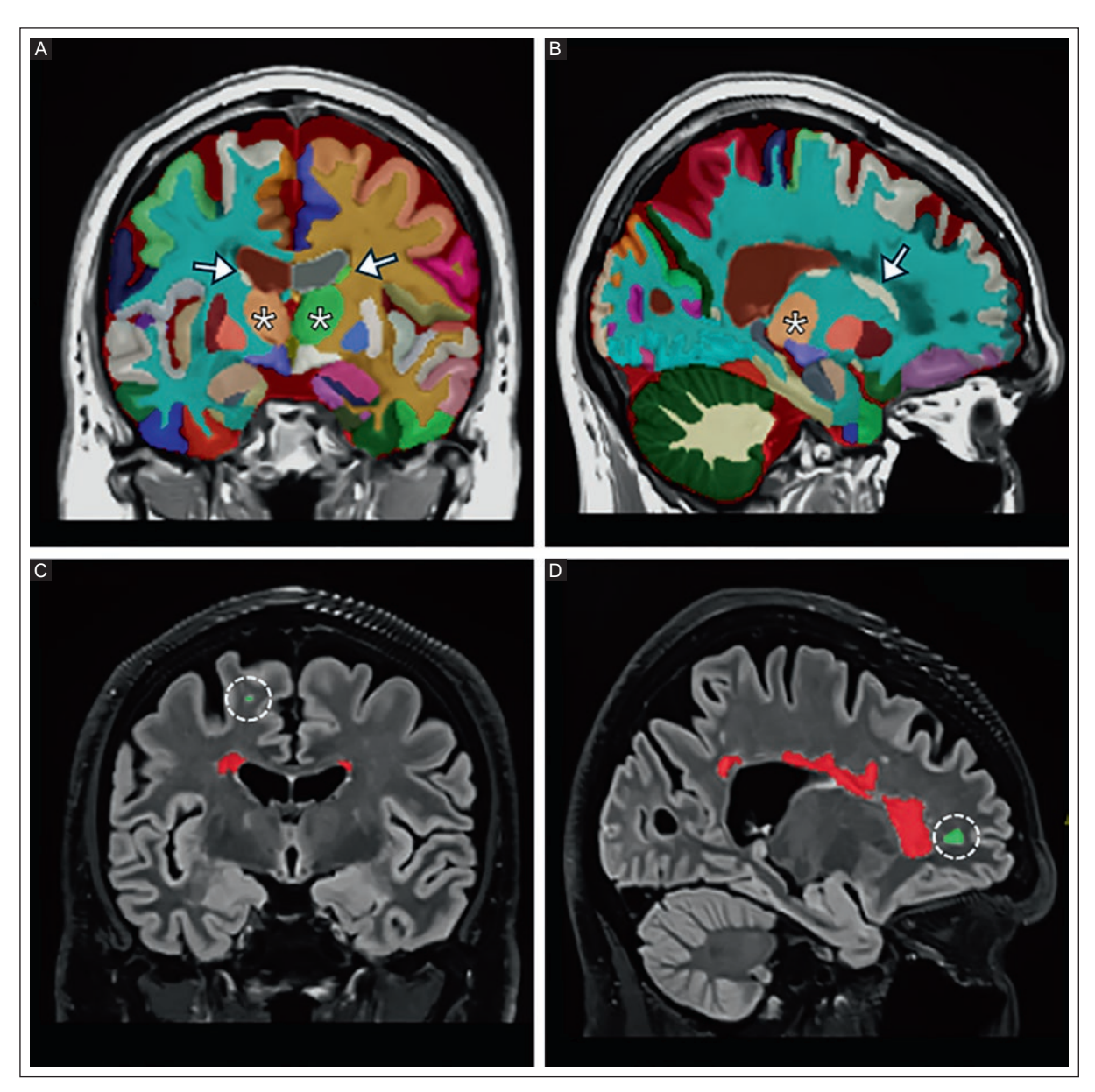


Figure 2. NIfTI-formatted brain MRI with structural volumetry and WML segmentation in a 59-year-old man with MS. A: coronal and B: sagittal plane with detailed brain segmentation. The subregions are color-coded differently for each hemisphere, including the thalamic nuclei (asterisks) and caudate nuclei (arrows). Normalized thalamic volume was 1.04% and normalized caudate nucleus volume was 0.33%. C: coronal and D: sagittal plane with periventricular (red) and deep WML (green, dotted white circle) WML segmentation. The normalized WML volume was 0.75% and the WML burden was 2.55%.

NIFTI: Neuroimaging Informatics Technology Initiative; MRI: magnetic resonance imaging; WML: white matter lesion; MS: multiple sclerosis.

and 1.03% in men, and the normalized caudate nucleus volume was 0.4% in women and 0.38% in men. These parameters were comparable in both sexes. In contrast, all WML metrics were higher in women than in men. The median number of lesions was 32 in women compared to 18 in men. The normalized WML volume was higher in women (median = 0.23%) than in men (median 0.11%), and the WML burden was a

median of 0.86% in women compared to 0.36% in men. However, the differences between women and men were not statistically significant for the WML metrics examined.

Figure 3 shows axial, sagittal, and coronal views and a 3D MRI reconstruction in a 40-year-old woman with MS. A low WML burden (0.42%) and normal total brain (88.14%), thalamus (1.11%), and caudate nucleus (0.50%)

E. Torres-Olivas et al. Thalamic atrophy correlates with WML metrics by MRI volumetry

Table 2. Characteristics of MS patients in relation to normalized total brain, thalamus, and caudate nucleus volumes and WML metrics by automated MRI volumetry analysis

Description	Parameter		
Age, years, mean ± SD (min-max)	44.6 ± 12.0 (20-70)		
Sex			
Women, n (%)	29 (72.5)		
Men, n (%)	11 (27.5)		
Normalized total brain volume, mean ± SD (min-max)	85.0 ± 2.9 (78.5-89.8)		
Normalized thalamic volume, mean ± SD (min-max)	1.1 ± 0.09 (1.0-1.4)		
Normalized caudate nucleus volume, mean ± SD (min-max)	$0.4 \pm 0.05 \ (0.3 \text{-} 0.5)$		
WML metrics			
Quantity, median, IQR (min-max)	29, 25 (2-108)		
Normalized volume, median, IQR (min-max)	0.19, 0.32 (0.002-2.44)		
Burden, median, IQR (min-max)	0.71, 1.25 (0.005-9.80)		

MRI: magnetic resonance imaging; WML: white matter lesion; SD: standard deviation; IQR: interquartile range; MS: multiple sclerosis.

Table 3. Comparison of normalized total brain, thalamus, and caudate nucleus volumes and WML metrics of automated MRI volumetry analysis between women and men with MS

Description	Women (n = 29)	Men (n = 11)	р
Normalized total brain volume, mean ± SD (min-max)	82.11 ± 3.04 (78.4-89.8)	84.9 ± 2.7 (80.2-87.8)	0.83
Normalized thalamic volume, mean ± SD (min-max)	1.11 ± 0.10 (0.96-1.39)	1.03 ± 0.04 (1.02-1.12)	0.12
Normalized caudate nucleus volume, mean \pm SD (min-max)	$0.40 \pm 0.05 \ (0.34 - 0.50)$	$0.38 \pm 0.04 \ (0.28 - 0.43)$	0.17
WML metrics			
Quantity, median, IQR (min-max)	32, 23 (2-108)	18, 26 (6-44)	0.23
Normalized volume, median, IQR (min-max)	0.23, 0.32 (0-1.09)	0.11, 0.32 (0.01-0.75)	0.37
Burden, median, IQR (min-max)	0.86, 1.11 (0.005-9.8)	0.36, 1.17 (0.01-8.17)	0.41

MRI: magnetic resonance imaging; MS: multiple sclerosis; WML: white matter lesion; SD: standard deviation; IQR: interquartile range.

volumes were found. Figure 4 shows axial, sagittal, and coronal views, and the 3D MRI reconstruction in a 41-year-old man with MS. A high WML burden (8.17%) and total brain (79.86%) and thalamus (0.79%) atrophy were found.

Correlation coefficients between WML metrics and the normalized volume of the total brain, thalamus, and caudate nucleus in MS patients

Spearman correlation coefficients showed a negative correlation between WML quantity, normalized WML volume, and WML burden and normalized volume of the total brain, thalamus, and caudate nucleus (Table 4).

The higher the quantity, volume, and burden of WML, the lower the normalized volume of the total brain, thalamus, and caudate nucleus, but only the correlation between the WML metrics and thalamic atrophy showed statistical significance. The heatmap shows the negative correlation coefficients between thalamic volume and WML quantity, normalized WML volume, and WML burden (r = -0.41, -0.52, and -0.54, respectively) (Figure 5). WML burden shows the strongest correlation with thalamic atrophy. The scatterplots show a significant correlation between the WML metrics and thalamic atrophy (p < 0.001) (Figure 6). Correlation coefficients with normalized volume of the total brain and caudate nucleus were not significant, although a negative trend was observed.

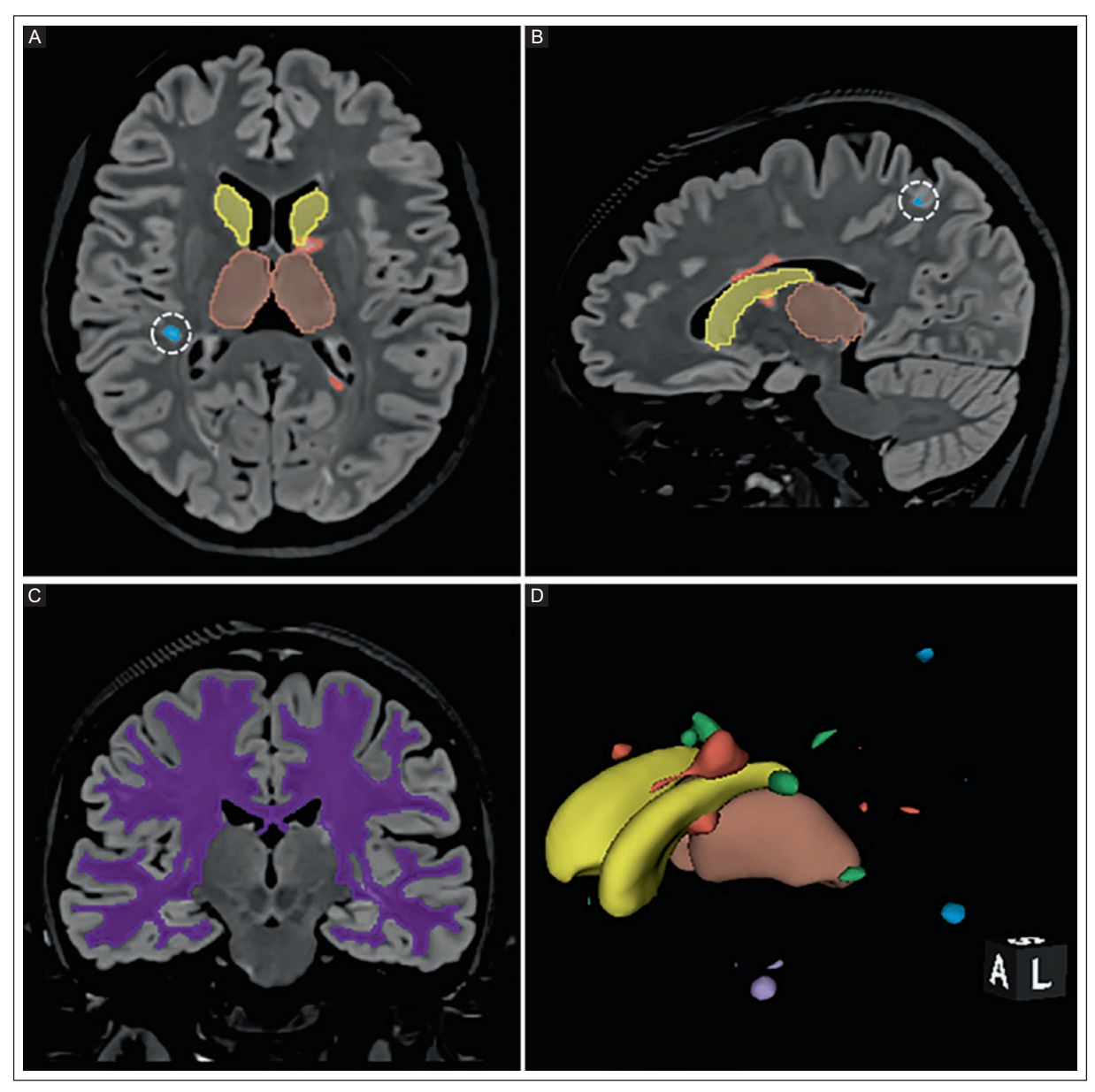


Figure 3. Brain MRI of a 40-year-old woman with MS and low WML burden and normal total brain, thalamus, and caudate nucleus volume^a. A: axial and B: sagittal plane of co-registered 3D-FLAIR fusion showing thalamus (brown) and caudate nucleus (yellow) segmentation and periventricular (red) and juxtacortical WML (blue, dashed white circle). C: coronal co-registered fusion of 3D-FLAIR with segmentation of the total white matter (purple). D: 3D volume rendering showing the volumetric relationship between the normalized thalamic volume (brown, 1.11%) and the normalized caudate nucleus volume (yellow, 0.50%) with a low normalized volume of the WML volume (red, green, blue, and magenta, 0.14%). The normalized total brain volume was 88.14% (not shown).

Nomal values show the expected cut-off (95% confidence interval) of normalized volume as a function of sex and age for reference purposes. MRI: magnetic resonance imaging; MS: multiple sclerosis; WML: white matter lesion; 3D-FLAIR: three-dimensional fluid-attenuated inversion recovery.

DISCUSSION

This study demonstrated a significant negative correlation between thalamic volume and WML quantity, normalized WML volume, and WML burden in MS patients; the higher the WML quantity, volume, and burden, the lower the normalized thalamic volume. To our

knowledge, this study is the first using an Al-based segmentation and volumetry tool in Mexican MS patients to correlate thalamic atrophy and WML metrics. Our ultimate goal is to close the knowledge gap regarding MS-related neurodegeneration in Mexican MS patients.

Several reports have shown that thalamus volume decreases as MS progresses, a phenomenon closely

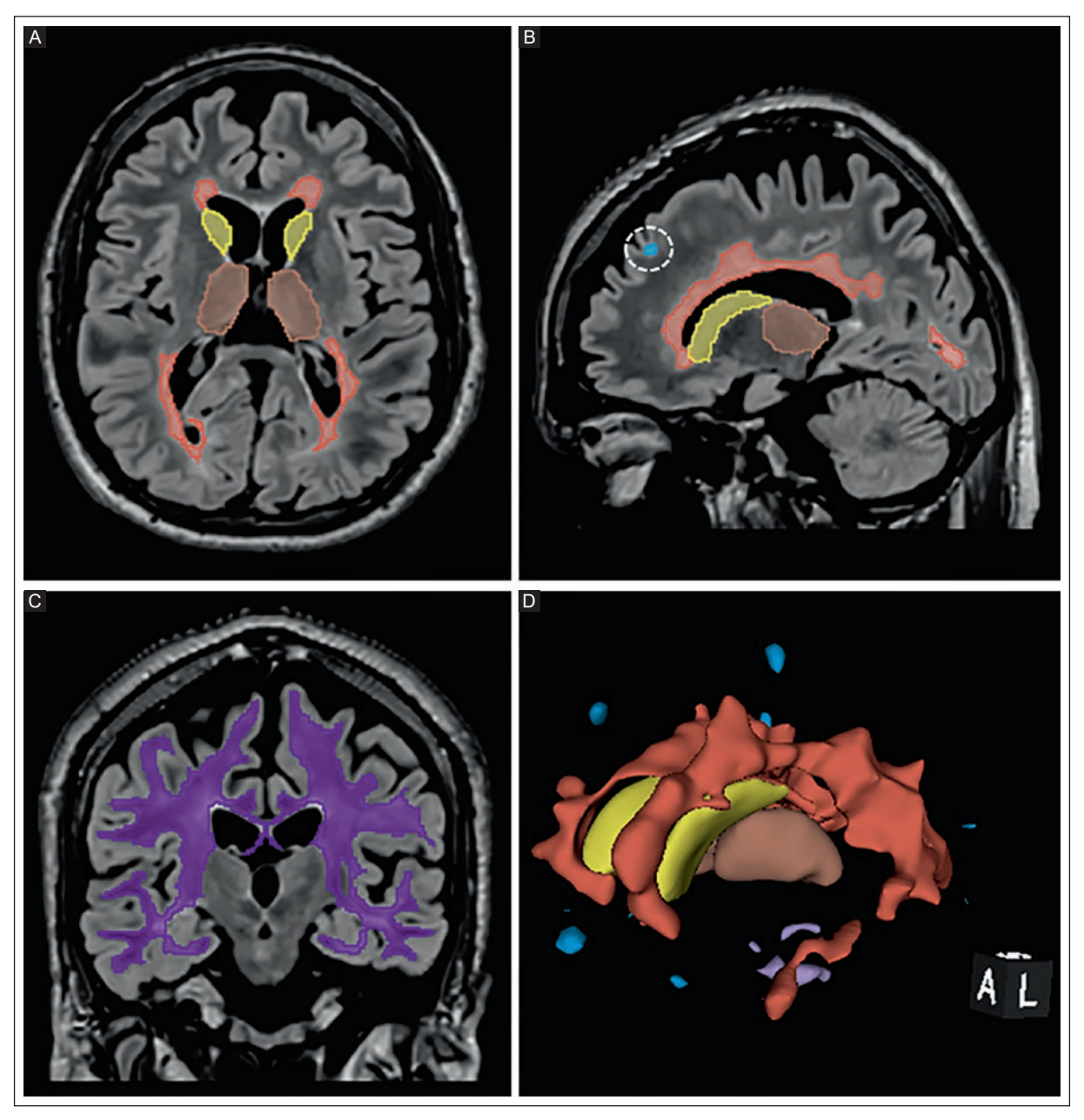


Figure 4. Brain MRI of a 41-year-old man with MS and a high WML burden (8.17%) with brain and thalamus atrophy. A: axial and B: sagittal planes of 3D-FLAIR co-registered fusion showing thalamus (brown) and caudate nucleus (yellow) segmentation and periventricular (red) and juxtacortical WML (blue, dashed circle) segmentation. C: coronal co-registered fusion of 3D-FLAIR with total white matter (purple) segmentation. D: 3D volume rendering showing the volumetric relationship between the normalized thalamus (brown, 0.79%) and caudate nucleus (yellow, 0.38%) volume and the normalized WML volume (red, green, blue, and magenta, 2.26%). The normalized total brain volume was 79.86% (not shown).

MRI: magnetic resonance imaging; MS: multiple sclerosis; WML: white matter lesion; 3D-FLAIR: three-dimensional fluid-attenuated inversion recovery.

related to WML accumulation^{1,5,7,10}. This atrophy process may be due to direct damage and remote effects through axonal transection, causing disconnections of tracts projecting to and from the thalamus. Bergsland et al.⁵ in a longitudinal study of 212 Czech patients with

clinically isolated syndrome and 177 with early relapsing remitting MS using the FIRST platform for automated volumetric 1.5T MRI analysis, showed that thalamus and caudate nucleus atrophy correlated significantly with T2 white matter lesion volume, highlighting the

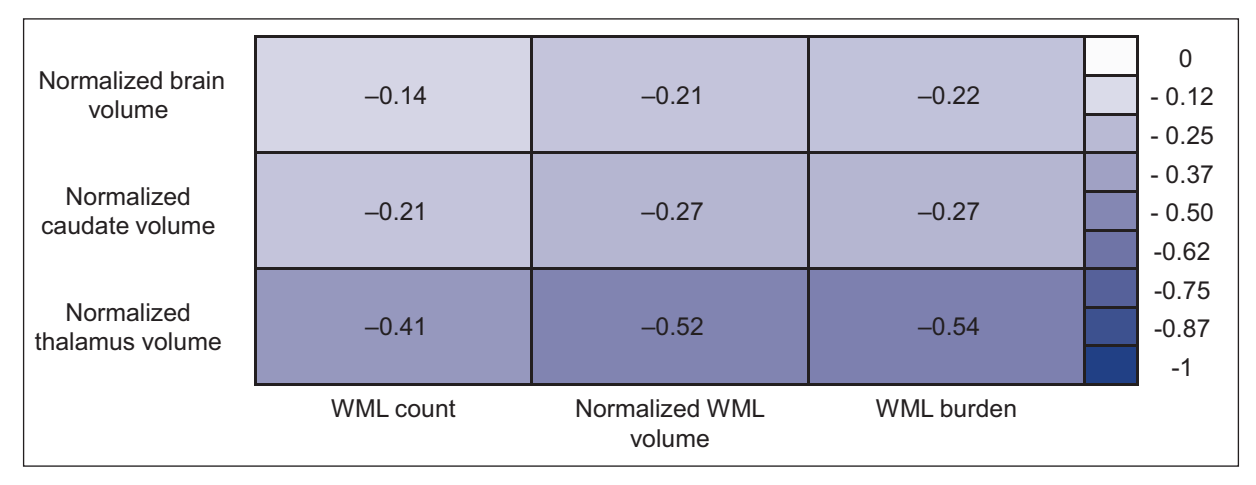


Figure 5. Heatmap showing the Spearman correlation coefficients between the normalized total brain, thalamus, and caudate nucleus volume with WML metrics in MS patients. A significant correlation was found between thalamic atrophy and WML metrics. WML burden showed the strongest correlation with thalamic atrophy. Normalized total brain volume showed the weakest correlation with the extent of WML. MS: multiple sclerosis; WML: white matter lesion.

Table 4. Spearman correlation coefficients between metrics of WML and normalized total brain, thalamus, and caudate nucleus volumes by automated MRI volumetry analysis in patients with MS

Metric	Normalized total brain volume	Normalized thalamic volume	Normalized caudate nucleus volume
WML quantity	-0.14	-0.41	-0.21
р	0.4	0.009	0.19
Normalized WML volume	-0.21	-0.52	-0.27
р	0.2	< 0.001	0.09
WML burden	-0.22	-0.54	-0.27
p	0.16	< 0.001	0.09

MRI: magnetic resonance imaging; MS: multiple sclerosis; WML: white matter lesion.

sensitivity of automated analysis in detecting deep structural damage. Our study using automated analysis from the web-based volBrain platform in MS patients, a significant correlation between reduced normalized thalamic volume and WML quantity (r = -0.41, p = 0.009), normalized WML volume (r = -0.52, p < 0.001), and WML burden (r = -0.54, p < 0.001) was demonstrated. WML burden showed the strongest correlation with thalamic atrophy. Lesion burden, defined as the volume occupied by the WML divided by the TWMV, is a metric directly reported by volBrain software that we consider a sensitive and comparable indicator of the extent of MS. Cagol et al.¹ compared 183 patients with MS and 105 healthy controls in a Swiss population study.

They showed that thalamic volume was reduced in MS patients compared to controls. Azevedo et al. 10 conducted a longitudinal study with 601 subjects and 2632 MRI examinations with T1 3D sequences using a longitudinal pipeline of FreeSurfer software (v5.3). They found that thalamic atrophy precedes global cortical atrophy and progresses significantly faster in MS patients (n = 520) than in healthy controls (n = 81). Thalamic atrophy is considered an MRI marker for neurodegeneration in MS patients.

White matter damage has a measurable structural impact on thalamic volume as a biomarker in the structural assessment of MS using automated MRI volumetry and segmentation. The correlation coefficients between the quantity, volume, and burden of WML and thalamic atrophy suggest a possible interaction between remote axonal damage and localized degeneration of deep gray matter nuclei^{5,8}. Atrophy associated with cumulative WML exposure has been found in subcortical structures such as the thalamus and caudate nucleus. However, individual susceptibility varies according to disease phenotype, clinical stage, and lesion location^{1,5,7}. Mehndiratta et al.¹³ reported the specific morphology of thalamic lesions with a 7T scanner using single-echo FLASH T2* sequences for lesion segmentation and a high-resolution T1-weighted 3D sequence in a 3T scanner for structural assessment in 90 MS patients and 44 healthy controls. Cortical surface reconstruction was performed using FreeSurfer software. Thalamic volume normalized to TIV was determined using the FIRST platform. They found that a larger WML volume was associated with

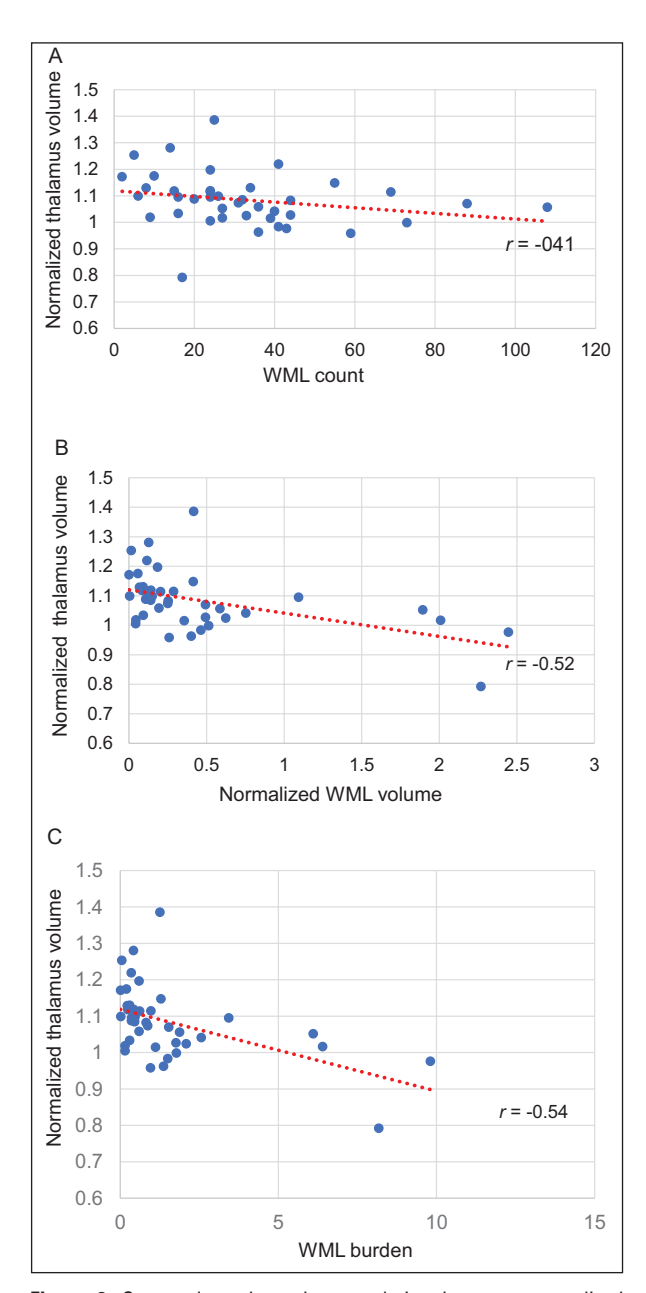


Figure 6. Scatterplots show the correlation between normalized thalamus volume and WML quantity, normalized WML volume, and WML burden. **A:** the correlation coefficient between normalized thalamus volume and WML quantity was r=-0.41 (p=0.009). **B:** the correlation coefficient between normalized thalamus volume and normalized WML volume was r=-0.52 ($p\le0.001$). **C:** the strongest correlation coefficient was found between normalized thalamus volume and WML burden (r=-0.54) with a steeper slope ($p\le0.001$). WML: white matter lesion.

thalamic atrophy, indicating that cortical and thalamic lesions were independent, suggesting that these lesions may have different pathogenetic mechanisms.

Total brain volume may remain relatively normal in early stages of MS even when the WML burden is significantly increased, suggesting that diffuse cortical

neurodegeneration may be a later event¹⁴. Azevedo et al. 10 observed thalamus atrophy in early stages of MS progression preceding volume loss of other deep gray matter structures, even in clinically isolated syndromes. In our study the mean age of MS patients was 44.6 years, representing a relatively young cohort in which no significant volume loss was observed in the total brain volume or caudate nucleus. Our study showed no significant correlation between the normalized volume of the total brain and caudate nucleus and higher WML burden. The lack of atrophy in these structures suggests that not all cortical and subcortical structures respond equally to the extent of WML in MS patients. This relative preservation of the volume of these structures could be due to neuroprotective age-related mechanisms or a short disease duration. This finding emphasizes the importance of assessing WML burden and thalamic volume, even in patients without obvious signs of cerebral atrophy.

The higher prevalence of MS in women has been attributed to hormonal and immunologic mechanisms that may influence inflammatory activity and MS progression¹⁵. However, the findings from quantitative MRI structural analysis by sex are limited. Ceccarelli et al.16 summarized sex-based specific neuroimaging findings in patients with MS. Studies using conventional T1- and T2-weighted MRI found that women with MS tend to have more active inflammatory lesions, while men have more chronic destructive lesions and more neurodegeneration, even with fewer lesions. This finding suggests that women are more likely to develop active lesions, while men have more severe structural damage. Our study found that women had higher values of WML metrics than men in WML quantity (median 32 and 18, respectively), normalized WML volume (median 0.23% and 0.11%, respectively), and WML burden (median 0.86% and 0.36%, respectively). Although the difference was not significant due to the small sample size, these results suggest that women with MS may have a higher inflammatory burden than men.

The strengths of this study are related to the imaging method, especially the automatic segmentation and volumetric analysis of the anatomical structures and WML metrics using the open-access, web-based vol-Brain platform. This deep learning tool provides a straightforward, user-friendly, and reliable way to analyze brain MRI in MS patients. The limitations of the study are related to the small sample size and cross-sectional design. Therefore, it was not possible to define the variability of findings over time and their relationship to clinical manifestations.

CONCLUSION

This study showed a significant correlation between thalamic atrophy and increased WML quantity, normalized WML volume, and WML burden in Mexican MS patients examined with an automated segmentation tool using standard isotropic MRI sequences. Prospective cohort studies with larger samples of Mexican MS patients are needed to determine the utility of automated segmentation and volumetric MRI analysis for establishing prognosis and assessing therapeutic response. The increasing availability of AI-based segmentation and volumetry software will further improve the understanding of MS-related neurodegeneration.

Acknowledgments

The authors thank Professor Ana M. Contreras-Navarro for her guidance in preparing and writing this scientific paper. This original research in the Radiology Specialty field was an awarded thesis at the Tercera Convocatoria Nacional 2024-2025 "Las Mejores Tesis para Publicar en el JMeXFRI".

Funding

This research received no external funding.

Conflicts of interest

The authors declare no conflicts of interest.

Ethical considerations

Protection of humans and animals. The authors declare that the procedures followed complied with the ethical standards of the responsible human experimentation committee and adhered to the World Medical Association and the Declaration of Helsinki (1964).

Confidentiality, informed consent, and ethical approval. The authors have obtained approval from the Ethics Committee for the analysis of routinely obtained and anonymized clinical data, so informed consent was not necessary.

Declaration on the use of artificial intelligence.

The authors declare that no generative artificial intelligence was used in the writing of this manuscript.

REFERENCES

- Cagol A, Ocampo-Pineda M, Lu PJ, Weigel M, Barakovic M, Melie-Garcia L, et al. Advanced quantitative MRI unveils microstructural thalamic changes reflecting disease progression in multiple sclerosis. Neurol Neuroimmunol Neuroinflamm. 2024;11(6):e200299. doi: 10.1212/NXI.0000000000200299.
- Whitwell JL, Crum WR, Watt HC, Fox NC. Normalization of cerebral volumes by use of intracranial volume: implications for longitudinal quantitative MR imaging. AJNR Am J Neuroradiol. 2001;22(8):1483-1489.
- Zhang S, Hu Y, Yang H, Li Q, Chen J, Bai H. Value of white matter hyperintensity volume and TWMV for evaluating cognitive impairment in patients with cerebral small-vessel disease. Front Aging Neurosci. 2023;15:1096808. doi: 10.3389/fnagi.2023.1096808.
- Vernooij MW, Jasperse B, Steketee R, Koek M, Vrooman H, Ikram MA, et al. Automatic normative quantification of brain tissue volume to support the diagnosis of dementia: A clinical evaluation of diagnostic accuracy. Neuroimage Clin. 2018;20:374-379. doi: 10.1016/ji.nicl.2018.08.004.
- Bergsland N, Horakova D, Dwyer MG, Dolezal O, Seidl ZK, Vaneckova M, et al. Subcortical and cortical gray matter atrophy in a large sample of patients with clinically isolated syndrome and early relapsing-remitting multiple sclerosis. AJNR Am J Neuroradiol. 2012; 33(8):1573-1578. doi: 10.3174/ajnr.A3086.
- Kamraoui RA, Ta VT, Tourdias T, Mansencal B, Manjon JV, Coup P. DeepLesionBrain: towards a broader deep-learning generalization for multiple sclerosis lesion segmentation. Med Image Anal. 2022;76:102312. doi:10.1016/j.media.2021.102312.
- Szekely-Kohn AC, Castellani M, Espino DM, Baronti L, Ahmed Z, Manifold WGK, et al. Machine learning for refining interpretation of magnetic resonance imaging scans in the management of multiple sclerosis: a narrative review. R Soc Open Sci. 2025;12(1):241052. doi: 10.1098/ rsos 241052
- Vrenken H, Jenkinson M, Horsfield MA, Battaglini M, van Schijndel RA, Rostrup E, et al. Recommendations to improve imaging and analysis of brain lesion load and atrophy in longitudinal studies of multiple sclerosis. J Neurol. 2013; 260(10):2458-2471. doi: 10.1007/s00415-012-6762-5.
- Tekin A, Rende B, Efendi H, Bunul SD, Çakır Ö, Çolak T, et al. Volumetric and symmetric index analysis of subcortical structures in multiple sclerosis patients: a retrospective study using volbrain software. Cureus. 2024; 16(3): e55799. doi: 10.7759/cureus.55799.
- Azevedo CJ, Cen SY, Khadka S, Liu S, Kornak J, Shi Y, et al. Thalamic atrophy in multiple sclerosis: a magnetic resonance imaging marker of neurodegeneration throughout disease. Ann Neurol. 2018; 83(2):223-234. doi: 10.1002/ana.25150.
- Manjón JV, Coupé P. volBrain: an online MRI brain volumetry system. Front Neuroinform. 2016;10:30. doi: 10.3389/fninf.2016.00030.
- Friedrichsmeier, T and the RKWard Team (2024). RKWard: graphical interface to the statistical language R. Version 0.8.0. https://rkward.kde.org.
- Mehndiratta A, Treaba CA, Barletta V, Herranz E, Ouellette R, Sloane JA, et al. Characterization of thalamic lesions and their correlates in multiple sclerosis by ultra-high-field MRI. Mult Scler. 2021; 27(5):674-683. doi: 10.1177/1352458520932804.
- Rocca MA, Comi G, Filippi M. The role of T1-Weighted derived measures of neurodegeneration for assessing disability progression in multiple sclerosis. Front Neurol. 2017;8:433. doi: 10.3389/fneur.2017.00433.
- D'Anca M, Buccellato FR, Tartaglia GM, Del Fabbro M, Muti P, Scarpini E, et al. Why is multiple sclerosis more frequent in women? role of the immune system and of oral and gut microbiota. Appl Sci. 2023;13(10):5881. doi:10.3390/app13105881.
- Ceccarelli A. Structural and functional brain damage in women with multiple sclerosis: a mini-review of neuroimaging sex-based studies. Front Neurol. 2022;13:1057446. doi: 10.3389/fneur.2022.1057446.





FULL RESEARCH ARTICLE

Stiffness cut-off value of point-shear wave elastography (pSWE) for predicting malignancy in peripheral lymphadenopathy

Roberto A. Sandoval-Villanueva^{1,2,3,4}, Humberto Cobian-Machuca^{1,2}*, Mauricio Figueroa-Sanchez¹, Christopher J. Lopez-Rodriguez^{2,5}, David F. Perez-Montemayor^{3,4} and Valeria Valdes-Lopez¹

¹Department of Radiology and Imaging, Antiguo Hospital Civil de Guadalajara "Fray Antonio Alcalde"; ²University Center of Health Sciences, Universidad de Guadalajara. Guadalajara, Jalisco; ³Centro de Imagenología Integral IMAX; ⁴Institute of Superior Studies of Tamaulipas, Faculty of Medicine, Universidad de Anahuac. Tampico, Tamaulipas; ⁵Department of Anatomic Pathology, Antiguo Hospital Civil de Guadalajara "Fray Antonio Alcalde", Guadalajara, Jalisco. Mexico

ABSTRACT

Introduction: The cut-off value for stiffness in point-shear wave elastography (pSWE) for the prediction of malignancy in peripheral lymphadenopathy has been insufficiently addressed. The aim of this study was to determine the optimal cut-off value for stiffness in pSWE for the prediction of malignancy in peripheral lymphadenopathy with cytopathologic diagnostic confirmation. Material and methods: Patients with peripheral lymphadenopathy were examined with conventional ultrasound (US), color Doppler US, and pSWE. Stiffness was determined in the region of interest (ROI), and the highest stiffness value was recorded. Fine needle aspiration biopsy (FNAB) and cell block (CB) were performed to confirm the diagnosis. The receiver operating characteristic (ROC) analysis defined the optimal stiffness cut-off value for the prediction of malignancy in peripheral lymphadenopathy. Results: We included 59 patients with peripheral lymphadenopathy in the neck, supraclavicular, axillary, or inguinal region; 23 (38.9%) lymph nodes (LNs) were malignant, and 36 (61.1%) were benign confirmed by cytopathology. The ROC analysis determined a stiffness cutoff value of \geq 3.4 m/s as a predictor of peripheral lymphadenopathy malignancy. Sensitivity was 73.9% (95% CI, 51.5-89.7), specificity 77.7% (95% CI, 60.8-89.8), and accuracy 76.2% (95% CI, 63.4-86.3). The area under the curve (AUC) was 0.72 (95% CI, 0.56-0.88). LNs. Hilar vascularity of peripheral LNs was significantly associated with a stiffness cut-off value < 3.4 in 20 (71.4%) of 28 cases with benign LNs (p = 0.041). Conclusions: The diagnostic accuracy of a pSWE stiffness cut-off value of \geq 3.4 m/s for predicting malignant peripheral lymphadenopathy was good. This study is the first to evaluate peripheral lymphadenopathy in the Mexican population using pSWE.

Keywords: Lymphadenopathy. Point shear wave elastography. Lymph node stiffness. Malignant lymphadenopathy.

INTRODUCTION

Elastography is an additional tool to conventional and color Doppler ultrasound (US) that evaluates tissue stiffness. Various elastography modalities have been used in the diagnostic evaluation of peripheral lymph nodes

(LNs)¹⁻⁵. Point-shear wave elastography (pSWE) uses Virtual Touch Imaging Quantification (VTIQ) technology, which generates shear waves based on the Acoustic Radiation Force Impulse (ARFI)⁶ and quantifies the shear wave velocity in the region of interest (ROI) to determine tissue stiffness in meters per second (m/s)^{7,8}.

Received for publication: 24-03-2025 Accepted for publication: 19-05-2025 DOI: 10.24875/JMEXFRI.M25000112 Available online: 10-10-2025 J Mex Fed Radiol Imaging. 2025;4(3):173-183 www.JMeXFRI.com

2696-8444 / © 2025 Federación Mexicana de Radiología e Imagen, A.C. Published by Permanyer. This is an open access article under the CC BY-NC-ND (https://creativecommons.org/licenses/by-nc-nd/4.0/).

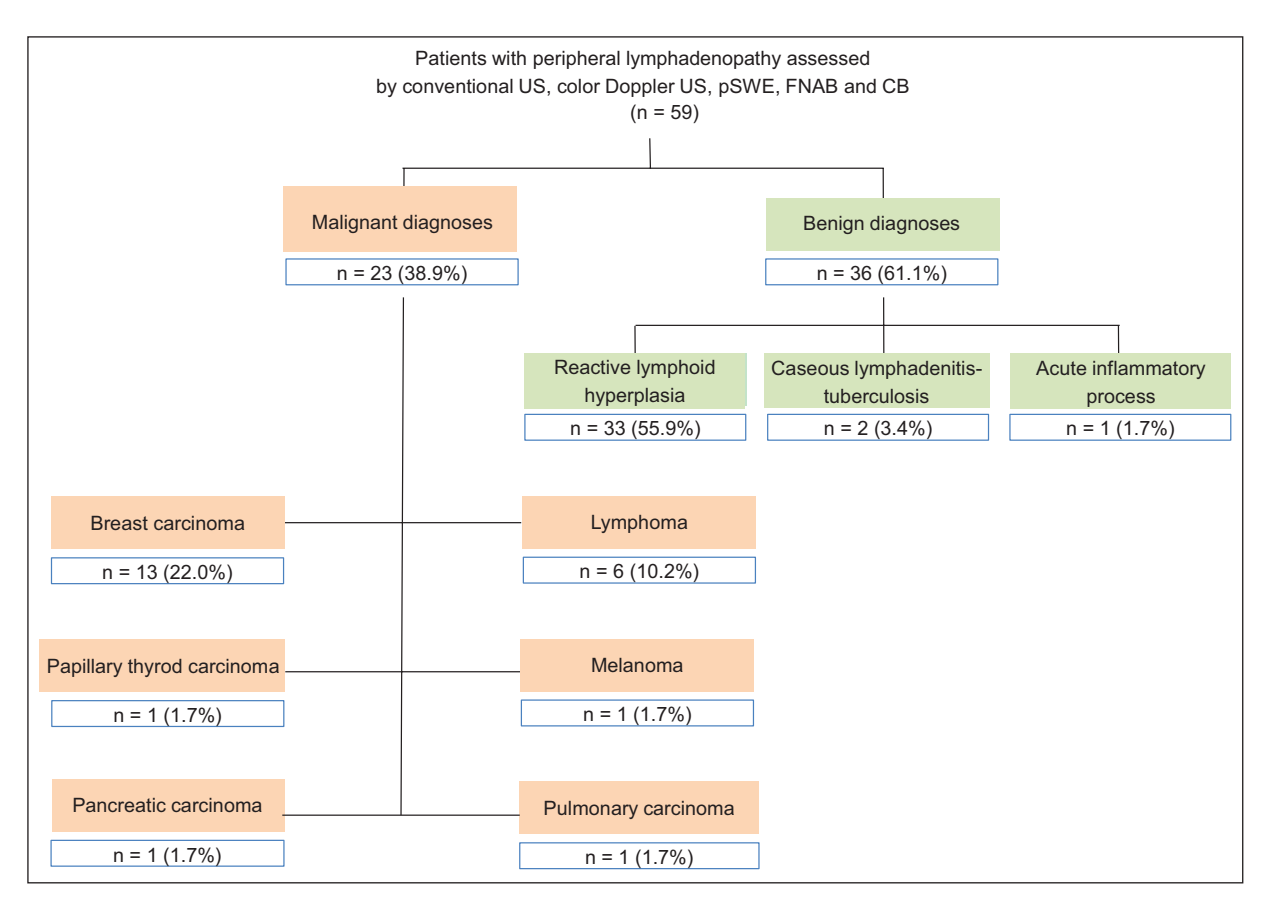


Figure 1. Flow chart of 59 patients with peripheral lymphadenopathy examined by conventional US, color Doppler US, pSWE, FNAB, and CB. Malignant lymphadenopathy was found in 23 (38.9%) of 59 cases. Breast carcinoma was the most common diagnosis (n = 13; 22.0%). Benign disease was found in 36 (61.1%) of 59 cases. Reactive lymphoid hyperplasia was the most common diagnosis (n = 33, 55.9%). pSWE: point-shear wave elastography; FNAB: fine needle aspiration biopsy; CB: cell block; US: ultrasound.

pSWE has been widely used to assess liver disease⁹⁻¹¹. However, there are few reports on the evaluation of peripheral LNs^{1,7}. Two reports on the cut-off values for pSWE stiffness in predicting malignancy of peripheral lymphadenopathy vary from $> 2.7 \text{ m/s}^1$ to $>3.2 \text{ m/s}^7$ with a sensitivity and specificity of 78-79% and 80-81%. The aim of this study was to determine the optimal cut-off value for stiffness in pSWE for the prediction of malignancy in peripheral lymphadenopathy with cytopathologic diagnostic confirmation.

MATERIAL AND METHODS

This prospective, cross-sectional study was conducted from October 2023 to December 2024 in the Department of Radiology and the Department of Pathology of the Antiguo Hospital Civil de Guadalajara "Fray Antonio Alcalde" in Guadalajara, Jalisco, Mexico. Patients of both sexes with peripheral lymphadenopathy detected on clinical examination by the referring physician

or by abnormal incidental imaging were included. Cytopathologic findings other than LNs or patients with coagulation abnormalities were excluded. Written informed consent was obtained from all patients. The institutional research ethics committee and the research committee approved this study.

Development and study variables

Patients with peripheral lymphadenopathy were assessed with conventional grayscale US, color Doppler US, and pSWE. Medical records were reviewed, and clinical diagnoses were recorded. The variables included sex, age, and the location of peripheral lymphadenopathy (neck, supraclavicular, axillary, and inquinal).

The conventional US findings recorded were shape (oval, round, or irregular), echogenicity (heterogeneous or homogeneous), size (mm), cortical thickness > 3 mm (yes/no), echogenic hilum (absent/present), and vascularity (hilum and peripheral/absent).

Table 1. Comparison between conventional US findings and stiffness by pSWE in malignant and benign peripheral lymphadenopathy

Description	Total (n = 59)	Malignant peripheral lymphadenopathy (n = 23)	Benign peripheral lymphadenopathy (n = 36)	р
Sex, n (%)				0.942
Women	49	19 (82.6)	30 (83.3)	
Men	10	4 (17.4)	6 (16.7)	
Age, years, mean ± SD (min-max)	46.1 ± 16.9 (6-73)	48.7 ± 16.8 (13-73)	44.3 ± 16.9 (6-71)	0.334
Detection of lymphadenopathy, n (%)				
Clinical examination	31	12 (52.2)	19 (52.8)	0.964
Incidental imaging finding	28	11 (47.8)	17 (47.2)	
Location of lymphadenopathy, n (%)				
Neck	13	4 (17.4)	9 (25.0)	0.049
Supraclavicular	2	2 (8.7)	-	
Axillary	38	17 (73.9)	21 (58.3)	
Inguinal	6	-	6 (16.7)	
US findings				
Shape, n (%)				
Oval	39	14 (60.9)	25 (69.4)	0.497
Round	19	8 (34.8)	11 (30.6)	
Irregular	1	1 (4.3)	0	
Echogenicity, n (%)				
Heterogeneous	4	2 (8.7)	2 (5.5)	0.640
Homogeneous	55	21 (91.3)	34 (94.5)	
Size, mm, mean ± SD (min-max)	11.5 ± 9.72 (1.6-57.9)	14.0 ± 11.4 (1.6-57.9)	10.0 ± 8.4 (2.5-42.4)	0.131
Cortical thickness >3 (mm), n (%)				
Yes	57	23 (100)	34 (94.5)	0.250
No	2	-	2 (5.5)	
Echogenic hilum, n (%)				
Absent	31	13 (56.5)	18 (50.0)	0.625
Present	28	10 (43.5)	18 (50.0)	
Vascularity, n (%)				
Hilum	28	6 (26.0)	22 (61.1)	0.009
Peripheral/absent	31	17 (74.0)	14 (38.2)	
pSWE				
Stiffness LN (m/s), mean ± SD (min-max)	3.4 ± 1.7 (0.8–8.0)	4.4 ± 2.3 (0.8–0 8.0)	2.8 ± 0.8 (1.4–5.2)	0.001

LN: lymph node; US: ultrasound; SD: standard deviation; pSWE: point-shear wave elastography.

Definitions

Lymphadenopathy: the presence of any of the following abnormalities detected by conventional US in LNs: oval or irregular shape, enlargement of the short axis by more than 10 mm, absent echogenic hilum, peripheral or absent vascularity¹².

pSWE: a US modality that uses shear waves generated by a point acoustic force from ARFI to quantify tissue stiffness in m/s⁹.

Stiffness: a quantitative measure of tissue resistance to deformation in m/s, determined by pSWE⁹.

Peripheral LNs: LNs located in the subcutaneous tissue anterior to the fasciae in the neck, supraclavicular, axillary, or inguinal regions examined with US^{13,14}.

Image acquisition and analysis protocol

Peripheral LN examination was performed using a Siemens ACUSON S2000 ultrasound (2008-2017

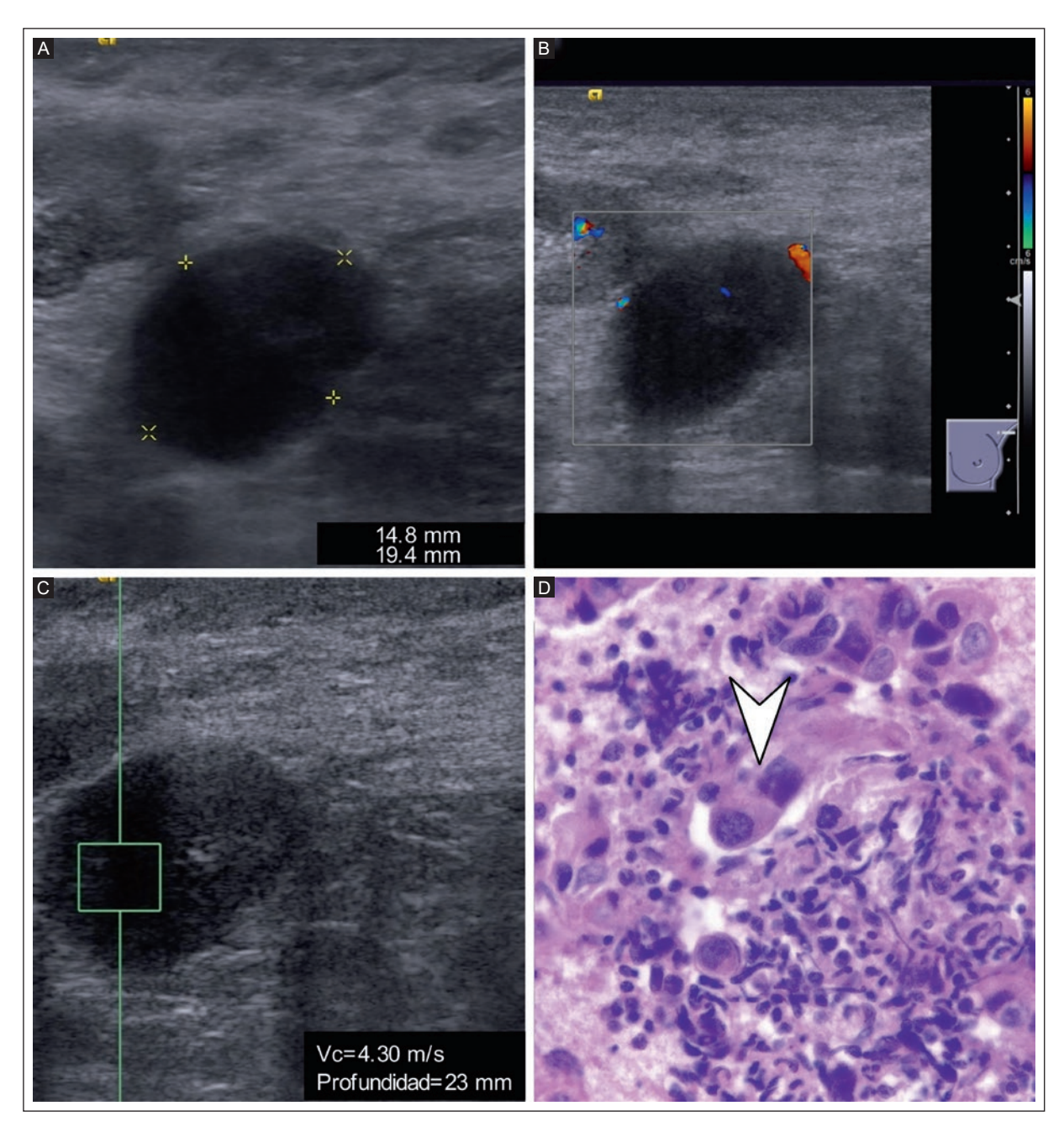


Figure 2. A 28-year-old woman with peripheral lymphadenopathy in the left axillary region. A: conventional US, longitudinal plane, shows an oval, homogeneous LN with a short axis of 14.8 mm, a thickened cortex, and the absence of an echogenic hilum. B: color Doppler US with peripheral vascularity. C: pSWE shows the LN with a stiffness cut-off value of 4.30 m/s. D: FNAB and CB examination shows large neoplastic cells with prominent nuclear pleomorphism characterized by a hyperchromatic, membrane irregularity with glandular formation (white arrowhead). The diagnosis was breast carcinoma.

LN: lymph node; US: ultrasound; pSWE: point-shear wave elastography; FNAB: fine needle aspiration biopsy; CB: cell block.

Siemens Medical Solutions USA, Inc., Mountain View, CA, USA) with a 9-4 MHz linear multi-D matrix transducer. After a conventional US assessment, pSWE images were acquired in different regions of the peripheral LNs. Five to 10 images were acquired in approximately

10 seconds. The number of images was directly related to the size of the LNs. The tissue adjacent to the LNs was not included in the stiffness measurement. The images were selected and stored in a Picture Archiving and Communication System (PACS) (SYNAPSE, Fujifilm

Medical Systems, Morrisville, NC, USA). The image evaluations were performed by a radiologist (HCM) with 20 years of experience.

Cytopathologic diagnosis

Fine needle aspiration biopsy (FNAB)¹⁵ and cell block (CB)¹⁶ were performed using standard techniques. The biopsy was taken from the LN area where the ROI showed the highest stiffness value, regardless of the tissue heterogeneity. The sample material was interpreted by a cytopathologist (CLR) with four years of experience.

Statistical analysis

Measures of central tendency (mean and median) and dispersion (standard deviation and interguartile ranges) were calculated for quantitative variables, according to the data distribution. The Mann-Whitney U test was used to compare these variables. Absolute frequencies and percentages were calculated for qualitative variables. Associations between the categories were assessed using Fisher's exact test. This test was chosen instead of the chi-square test because there were cells with expected values of less than 5. The diagnostic performance of pSWE using the optimal cut-off point of stiffness in distinguishing benign from malignant LNs was estimated using the receiver operating characteristic (ROC) analysis. A p value < 0.05 was considered the threshold for statistical significance. SPSS v.25 (IBM Corp., Armonk, NY. USA) was used for the statistical analysis.

RESULTS

Cytopathologic diagnosis in patients with peripheral lymphadenopathy

A total of 59 patients with peripheral lymphadenopathy were examined with conventional US, color Doppler US, and pSWE. FNAB and CB were performed for cytopathologic diagnosis: 23 (38.9%) of 59 cases were malignant LNs, and 36 (61.1%) were benign LNs (Figure 1). The malignancies diagnosed were 13 (22.0%) breast carcinomas, 6 (10.2%) lymphomas, 1 (1.7%) melanoma, 1(1.7%) papillary thyroid carcinoma, 1 (1.7%) pulmonary carcinoma, and 1 (1.7%) pancreatic carcinoma. Of the benign lymphadenopathies, 33 (55.9%) were reactive lymphoid hyperplasia, 2 (3.4%) were caseous lymphadenitis tuberculosis, and 1 (1.7%) was an acute inflammatory process.

Comparison between conventional US findings and stiffness by pSWE in malignant and benign peripheral lymphadenopathy

Of the 59 patients, 49 (83.1%) were women and 10 (16.9%) were men. The mean age was 46 ± 16.9 years. Malignant peripheral LNs were diagnosed in 23 (39.0%) patients and benign peripheral LNs in 36 (61.0%) (Table 1). The proportion of malignant and benign LNs was comparable in women (n = 19, 82.6%, and n = 30, 83.3%, respectively) and men (n = 4, 17.4%, and n = 6, 16.7%, respectively) (p = 0.942). The most common location was axillary, both for malignant (n = 17, 73.9%) and benign LNs (n = 21, 58.3%). All 6 inguinal LNs were diagnosed as benign (p = 0.049), while malignant supraclavicular LNs (n = 2) were the least common.

US characteristics such as shape, echogenicity, cortical thickening, and echogenic hilum were comparable between malignant and benign LNs. The size of peripheral LNs was larger in malignant cases, averaging 14.0 \pm 11.4 mm, than in benign cases, averaging 10.04 \pm 8.37 mm, but the difference was not significant (p = 0.131). On color Doppler US examination, the presence of hilar vascularity was less common in malignant LNs (n = 6, 26.0%) than in benign LNs (n = 22, 61.1%). In contrast, peripheral or absent vascularity was significantly more frequent in malignant LNs (n = 17, 74.0%) than benign LNs (n = 14, 38.2%) (p = 0.009). The mean stiffness of LNs was significantly different between malignant (4.4 \pm 2.3 m/s) and benign LNs (2.8 \pm 0.8 m/s) (p = 0.001).

Figure 2 of axillary lymphadenopathy shows an oval, homogeneous LN with a short axis of 14.8 mm, a thickened cortex, and an absence of an echogenic hilum and peripheral vascularity. pSWE shows a LN with a stiffness value of 4.3 m/s. The cytopathologic diagnosis was breast carcinoma. Figure 3 of a neck lymphadenopathy shows an oval, homogeneous LN with a short axis of 7.3 mm, a thickened cortex, and an absence of an echogenic hilum and vascularity. pSWE shows a LN with a stiffness value of 1.2 m/s. The cytopathologic diagnosis was reactive lymphoid hyperplasia.

Figure 4 of axillary lymphadenopathy shows an oval, homogeneous LN with a short axis of 48.6 mm, a thickened cortex, and an absence of an echogenic hilum and vascularity. pSWE shows a LN with a stiffness value of 4.57 m/s. The cytopathologic diagnosis was breast carcinoma. Figure 5 of an axillary lymphadenopathy shows an oval, homogeneous LN with a short axis of 28.7 mm, a thickened cortex, and an absence of an echogenic hilum and peripheral vascularity. pSWE shows an LN with a stiffness value of 7.77 m/s. The cytopathologic diagnosis was breast carcinoma.

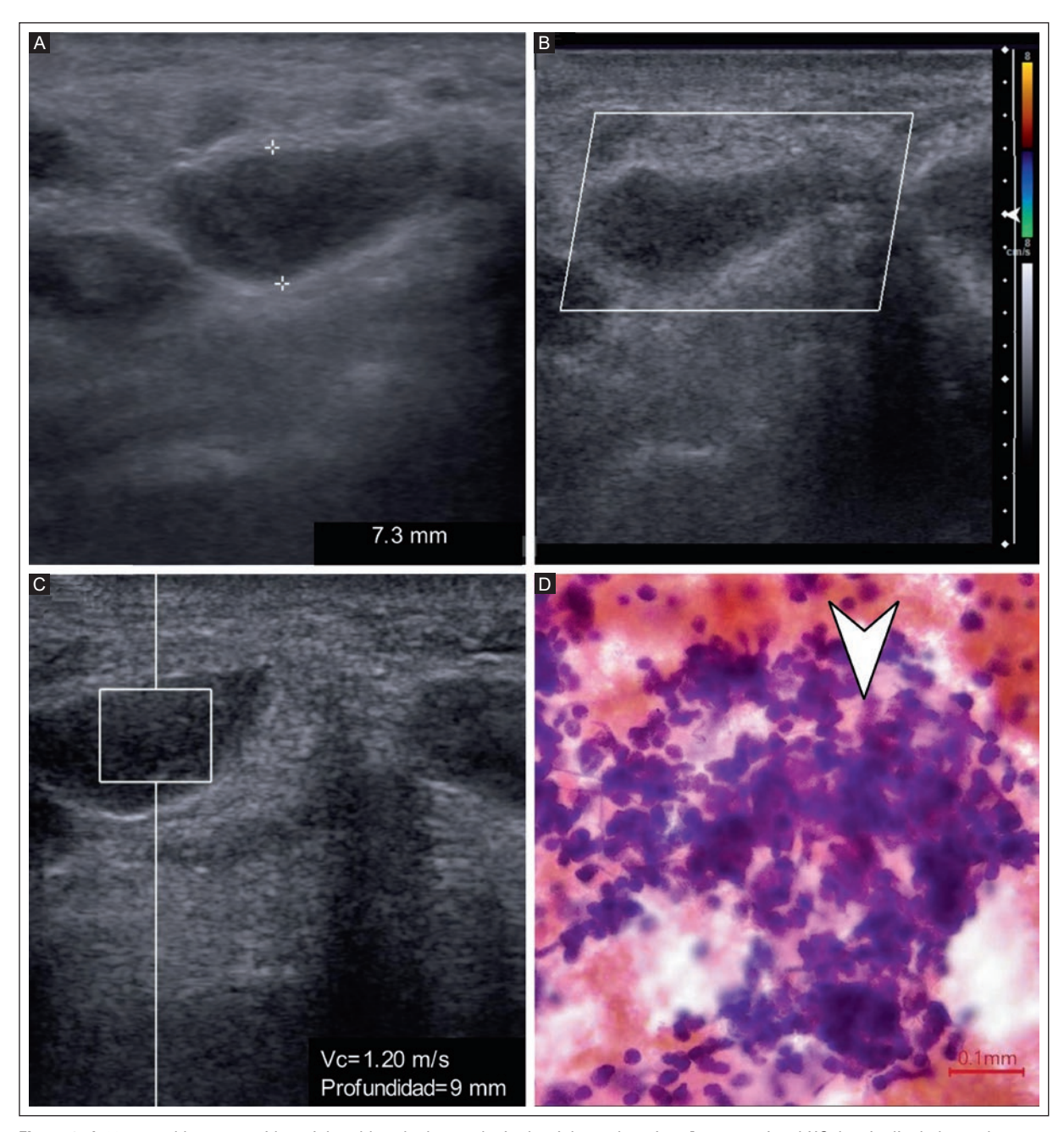


Figure 3. A 66-year-old woman with peripheral lymphadenopathy in the right neck region. A: conventional US, longitudinal plane, shows an oval, homogeneous LN with a short axis of 7.3 mm, a thickened cortex, and the absence of an echogenic hilum. B: color Doppler US shows the absence of vascularity. C: pSWE shows the LN with a stiffness cut-off value of 1.20 m/s. D: FNAB cytopathology shows abundant lymphocytes in different stages of maturation and histocytes (white arrowhead). The diagnosis was reactive lymphoid hyperplasia.

 $LN: Iymph\ node;\ US:\ ultrasound;\ pSWE:\ point-shear\ wave\ elastography;\ FNAB:\ fine\ needle\ aspiration\ biopsy.$

Diagnostic performance of the stiffness cut-off value (≥ 3.4 m/s) on pSWE for the prediction of malignancy in peripheral lymphadenopathy

Figure 6 shows a ROC curve demonstrating that a stiffness cut-off value of \geq 3.4 m/s of LN on pSWE is

the optimum for predicting malignancy of peripheral lymphadenopathy. This cut-off value achieved a sensitivity of 73.9% (95% CI, 51.5-89.7), a specificity of 77.8% (95% CI, 60.8-89.8), and an overall accuracy of 76.2% (95% CI, 63.4-86.3). The area under the curve (AUC) for the prediction of malignant peripheral lymphadenopathy was 0.72 (95% CI, 0.56-0.88) (Table 2).

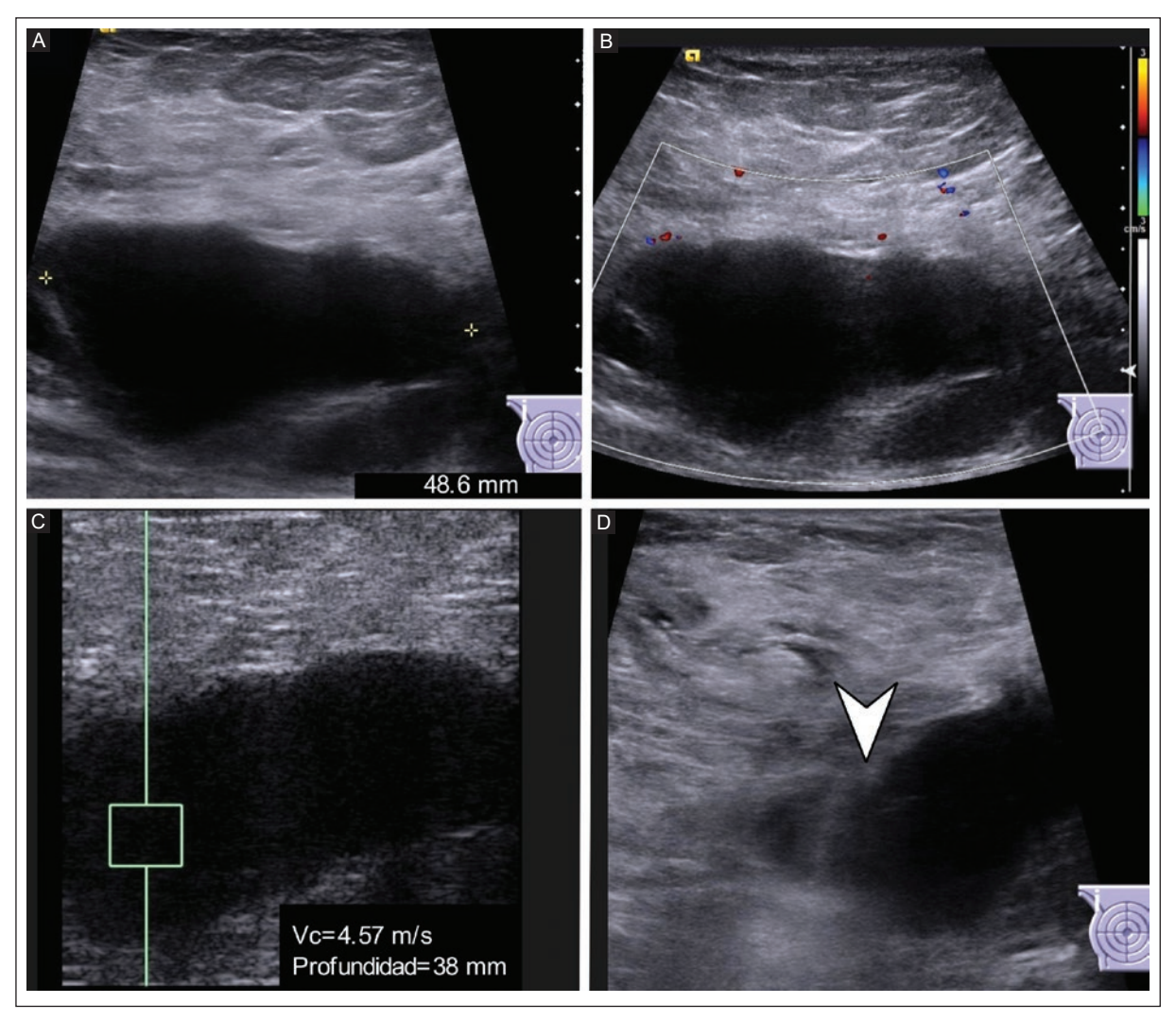


Figure 4. A 52-year-old woman with peripheral lymphadenopathy in the right axillary region. A: conventional US, longitudinal plane, shows an oval, homogeneous LN with a short axis of 48.6 mm, a thickened cortex, and the absence of an echogenic hilum. B: an absence of vascularity in color Doppler US. C: pSWE shows the LN with a stiffness cut-off value of 4.57 m/s. D: the needle tip (white arrowhead) is seen during the FNAB performed in the ROI with the highest LN stiffness by pSWE. The diagnosis was breast carcinoma.

LN: lymph node; US: ultrasound; pSWE: point-shear wave elastography; FNAB: fine needle aspiration biopsy; ROI: region of interest.

The positive predictive value was 68.0% (95% CI, 52.4-80.4) and the negative predictive value was 82.3% (95% CI, 69.6-90.4). The true-positive and true-negative results were 17 and 28, respectively, and the false-positive and false-negative results were 8 and 6, respectively.

Comparison of pSWE stiffness cut-off values and conventional US findings in peripheral lymphadenopathy

Twenty-eight (82.4%) of 34 LNs with a stiffness cutoff value < 3.4 were benign, while 6 (17.6%) were malignant (Table 3). In contrast, 17 (68%) of 25 LNs with a stiffness cut-off value \geq 3.4 m/s were malignant, while only 8 (32%) were benign (p < 0.001). The peripheral lymphadenopathy location, shape, echogenicity, cortical thickening, or echogenic hilum were comparable between malignant and benign LNs. The hilar vascularity of peripheral LNs was significantly associated with a stiffness cut-off value < 3.4 in 20 (71.4%) of 28 cases with benign LNs (p = 0.041).

DISCUSSION

In our study, the diagnostic performance of the stiffness cut-off value \geq 3.4 m/s of pSWE for predicting the

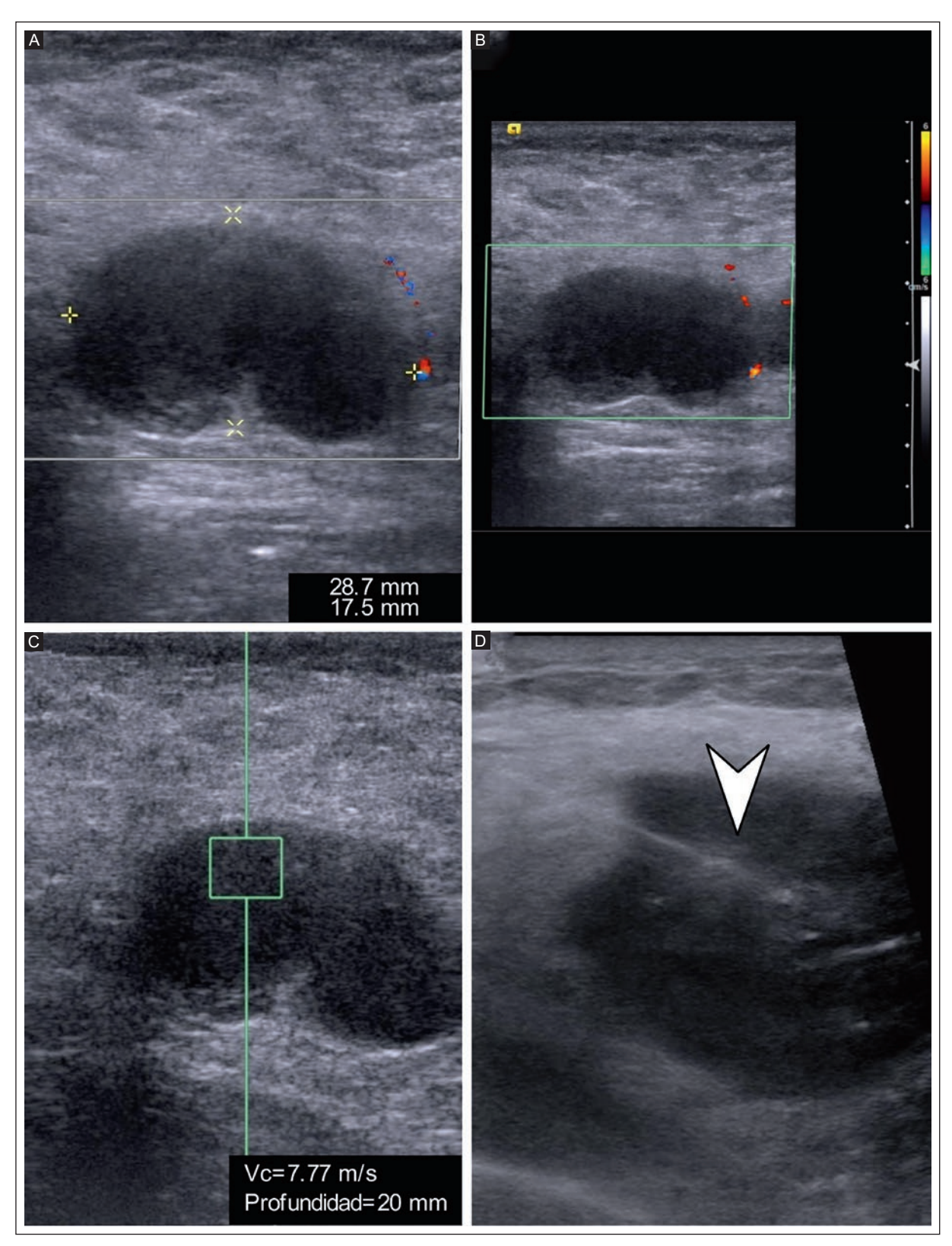


Figure 5. A 51-year-old woman with peripheral lymphadenopathy in the right axillary region. A: a conventional US, longitudinal plane, shows oval, homogeneous LN with a short axis of 28.7 mm, a thickened cortex, and the absence of an echogenic hilum. B: color Doppler US shows peripheral vascularity. C: pSWE shows the LN with a stiffness cut-off value of 7.77 m/s. D: the needle tip (white arrowhead) is seen during the FNAB performed in the ROI with the highest pSWE LN value. The diagnosis was breast carcinoma.

LN: lymph node; US: ultrasound; pSWE: point-shear wave elastography; FNAB: fine needle aspiration biopsy; ROI: region of interest.

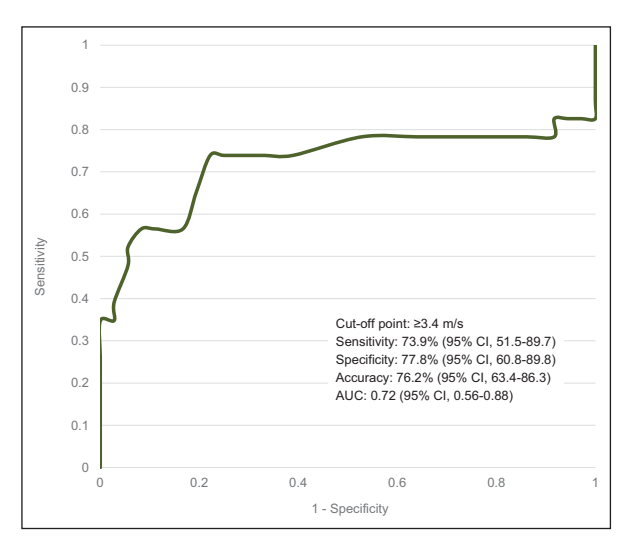


Figure 6. The ROC curve shows that the stiffness cut-off value ≥ 3.4 m/s of LNs on pSWE has the highest sensitivity (73.9%), specificity (77.8%) and accuracy (76.2%) for the prediction of malignant peripheral lymphadenopathy.

AUC: area under curve; LNs: lymph nodes; ROC: receiver operating characteristic; pSWE: point-shear wave elastography.

Table 2. Diagnostic performance of the stiffness cut-off value $(\ge 3.4 \text{ m/s})$ on pSWE for the prediction of malignant peripheral lymphadenopathy

Description	% (95% CI)
Sensitivity	73.9 (51.5-89.7)
Specificity	77.7 (60.8-89.8)
Positive LR (min-max)	3.3 (1.7-6.4)
Negative LR (min-max)	0.34 (0.16-0.68)
Positive predictive value	68.0 (52.4-80.4)
Negative predictive value	82.3 (69.6-90.4)
Accuracy	76.2 (63.4-86.3)

pSWE: point-shear wave elastography; LR: likelihood ratio.

malignancy of peripheral lymphadenopathy was good. This study is the first to evaluate peripheral lymphadenopathy using pSWE in the Mexican population and suggests a specific stiffness cut-off value for predicting malignancy in peripheral lymphadenopathy.

Stiffness quantified by elastography has been proposed to differentiate benign and malignant LNs^{1,7}. pSWE quantifies the stiffness of a focal area (ROI) with a minimum size of 1.5 mm in diameter⁷. Azizi et al.⁷ examined 270 LNs with conventional US, color Doppler US, and pSWE with cytopathologic confirmation in a

study of 231 US patients with neck lymphadenopathy. Benian LNs were diagnosed in 216 (80.0%) and malignant LNs in 54 (20.0%). The stiffness of the neck lymphadenopathy was determined by averaging two recordings of the stiffness area. In the ROC curve analysis, a cutoff value of > 2.93 m/s showed a sensitivity of 92.5% and a specificity of 75.4% for predicting malignancy. In addition, three categories were analyzed according to the stiffness of the LNs: 0-2.6 m/s, $> 2.6 - \le 3.2$ m/s, and > 3.2 m/s. The cut-off point of > 3.2 m/s had a sensitivity of 79.6% and a specificity of 81.9% for predicting malignancy. The authors concluded that the diagnostic performance of pSWE was good for differentiating benign and malignant cervical LNs. Kerim et al.1 in a study of 115 patients, differentiating malignant and benign peripheral lymphadenopathy, compared pSWE vs. strain elastography with a histopathologic diagnosis: 78 (67.8%) cases were malignant and 37 (32.2%) benign. The mean value of three pSWE measurements was obtained in an ROI of different LN areas. The ROC analysis defined a cut-off value > 2.7 m/s with a sensitivity of 88.5%, and a specificity of 89.2% for malignancy, with an AUC of 0.819. Our study showed a stiffness cut-off value ≥ 3.4 m/s on pSWE with a sensitivity of 73.9%, a specificity of 77.7%, an accuracy of 76.2% and an AUC of 0.72 for predicting malignancy in peripheral lymphadenopathy. Our results were comparable to those of Azizi et al.7 with a stiffness cut-off value > 3.2 m/s on pSWE, which showed a sensitivity of 79.6% and a specificity of 81.9% for predicting malignancy. Quantitative assessment of LN stiffness with pSWE may help clinicians to recommend biopsy in peripheral lymphadenopathy in patients with suspected malignancy.

Lymphomas are a heterogeneous group of lymphoproliferative neoplasms¹⁷. Conventional US examination can have difficulty distinguishing between metastases and lymphoma of LNs¹⁸. Internal hemorrhage or necrosis in these lesions may produce a lower stiffness value¹⁹. In our study, 6 peripheral LNs were diagnosed with pSWE stiffness values that ranged from 0.7 m/s to 5.7 m/s. Three (50.0%) of the lymphomas showed a stiffness cut-off value ≥ 3.4 m/s with stiffness variability in different LN regions. Kerim's study⁷ analyzed metastatic peripheral lymphadenopathy and primary lymphoproliferative neoplasms of LNs. In 22 lymphomas, pSWE stiffness values were recorded from different parts of the LN, avoiding the fatty hilum and necrotic areas. The mean stiffness value of LNs was 2.75 ± 0.58 m/s compared to the mean value of metastatic LNs with a stiffness value of 3.43 ± 0.58 m/s on pSWE.

Table 3. Comparison of stiffness cut-off values in pSWE and conventional US findings in peripheral lymphadenopathy

Description	Total	Stiffness cut-	Stiffness cut-off value, m/s		
	(n = 59)	< 3.4 (n = 34)	≥ 3.4 (n = 25)	_	
Malignant peripheral lymphadenopathy, n (%)				< 0.001	
Yes	23	6 (17.6)	17 (68.0)		
No	36	28 (82.4)	8 (32.0)		
Location of lymphadenopathy, n (%)				0.211	
Neck	13	8(23.5)	5 (20.0)		
Supraclavicular	2	0	2 (8.0)		
Axillary	38	21 (61.8)	17 (68.0)		
Inguinal	6	5 (14.7)	1 (4.0)		
US findings					
Shape, n (%)				0.792	
Oval	39	22 (64.7)	17 (68.0)		
Round	19	12 (35.3)	7 (28.0)		
Irregular	1	0	1 (4.0)		
Echogenicity, n (%)				0.466	
Heterogeneous	4	3 (8.8)	1 (4.0)		
Homogeneous	55	31 (91.2)	24 (96.0)		
Cortical thickness > 3mm, n (%)				0.217	
Yes	57	32 (94.1)	25 (100)		
No	2	2 (5.9)	-		
Echogenic hilum, n (%)				0.943	
Absent	31	18 (52.9)	13 (52.0)		
Present	28	16 (47.1)	12 (48.0)		
Vascularity, n (%)				0.041	
Hilar	28	20 (58.8)	8 (32.0)		
Peripheral/absent	31	14 (41.2)	17 (68.0)		

US: ultrasound; pSWE: point-shear wave elastography.

These differences may be due to substantial variability in the viscoelastic properties of lymphoid tissue with lower stiffness. For metastatic peripheral lymphadenopathy, the stiffness value reported by Kerim (3.43 \pm 0.58 m/s) is comparable to our stiffness cut-off value (\geq 3.4 m/s), but our analyzes do not differentiate lymphoproliferative neoplasms and metastatic LNs, although most diagnoses in our study were metastatic peripheral lymphadenopathy (n = 17, 73.9%). Lymphomas may exhibit different elastographic features compared to metastatic peripheral lymphadenopathy.

Most benign LNs have central hilar vessels that can be identified, even if the echogenic hilum is not observed²⁰. Benign LNs have one vascular pedicle that enters the hilum, in contrast to malignant LNs, which have multiple vascular pedicles that may invade the

cortex²¹. Sarda-Inman et al.²⁰ found 34 benign and 39 malignant LNs in 73 Mexican patients with neck lymphadenopathy evaluated with color Doppler, which showed 46.1% (n = 18) with hilar vascularity and 53.9% (n = 21) with non-hilar vascularity of malignant etiology. In contrast, 26.4% (n = 9) of benign lymphadenopathies had non-hilar vascularity, while 73.6% (n = 25) of 34 benign LNs had hilar vascularity. In our study, a significant association between the presence of hilar vascularity and lower tissue stiffness (< 3.4 m/s) was found in 20 (71.4%) of 28 benign LNs (p = 0.041). This result is comparable to the color Doppler US findings of the Sarda-Inman study²⁰. Hilar vascularity has been associated with benignity²¹, but there are currently no studies demonstrating a direct association between lower LN tissue stiffness values and hilar vascularity.

The strengths of this study include its prospective study design and diagnosis confirmation by both FNAB and CB in all cases of peripheral lymphadenopathy. Similarly, the use of pSWE identified ROIs with the highest LN stiffness in which the biopsy was performed. The limitations of the study were the fact that it was a single center and a small sample. On the other hand, ROI placement was operator dependent and intra-observer and inter-observer agreement was not examined to account for inter-operator variability.

CONCLUSION

In this study, ROC analysis showed that the optimal pSWE stiffness cutoff value was ≥ 3.4 m/s for the prediction of malignant peripheral lymphadenopathy with good diagnostic performance. Future research is needed to validate the clinical application of the proposed stiffness cutoff value based on our results, particularly multicenter studies with larger sample sizes.

Acknowledgments

The authors thank Professor Ana M. Contreras-Navarro for her guidance in preparing and writing this scientific paper. This original research in the Radiology Specialty field was an awarded thesis at the Tercera Convocatoria Nacional 2024-2025 "Las Mejores Tesis para Publicar en el JMeXFRI".

Funding

The authors declare that they have not received funding.

Conflicts of interest

The authors declare no conflicts of interest.

Ethical considerations

Protection of humans and animals. The authors declare that the procedures followed complied with the ethical standards of the responsible human experimentation committee and adhered to the World Medical Association and the Declaration of Helsinki (1964).

Confidentiality, informed consent, and ethical approval. The authors have obtained approval from the Ethics Committee for the analysis of routinely obtained and anonymized clinical data.

Declaration on the use of artificial intelligence.

The authors declare that no generative artificial intelligence was used in the writing of this manuscript.

REFERENCES

- Kerim AAA, Abd AME, Naguib NN, Guimei M, Emara DM. Shear wave elastography versus strain elastography to identify benign superficial lymph nodes: sonographic assessment with histopathological confirmation. Egypt J Radiol Nucl Med. 2023;54(1):32. doi: 10.1186/s43055-023-00983-5.
- Wang B, Guo Q, Wang JY, Yu Y, Yi AJ, Cui XW, et al. Ultrasound elastography for the evaluation of lymph nodes. Front Oncol. 2021;11:714660. doi: 10.3389/fonc.2021.714660.
- Lo WC, Cheng PW, Wang CT, Liao LJ. Real-time ultrasound elastography: an assessment of enlarged cervical lymph nodes. Eur Radiol. 2013; 23(9):2351-2357. doi: 10.1007/s00330-013-2861-7.
- Onol S, Ozkaya O. Diagnostic value of real-time elastography in diagnosing lymph node metastasis of skin cancer. Cureus. 2020;12(10):e10997. doi: 10.7759/cureus.10997.
- Acu L, Oktar SÖ, Acu R, Yücel C, Cebeci S. Value of ultrasound elastography in the differential diagnosis of cervical lymph nodes: a comparative study with B-mode and color doppler sonography. J Ultrasound Med. 2016;35(11):2491-2499. doi: 10.7863/ultra.15.09019.
- Benson J, Fan L. Understanding ARFI and new elastography quantification technologies. Mountain View, CA. USA: Siemens Medical Solutions USA Inc.; 2014. 10p.
- Azizi G, Keller JM, Mayo ML, Piper K, Puett D, Earp KM, et al. Shear wave elastography and cervical lymph nodes: predicting malignancy. Ultrasound Med Biol. 2016;42(6):1273-1281. doi: 10.1016/j.ultrasmedbio. 2016.01.012.
- Abdelgawad, EA, Abu-samra, MF, Abdelhay, NM. B-mode ultrasound, color Doppler, and sonoelastography in differentiation between benign and malignant cervical lymph nodes with special emphasis on sonoelastography. Egypt J Radiol Nucl Med. 2020;51:157. doi: 10.1186/s43055-020-00273-4.
- Barr RG. Multiparametric ultrasound for chronic liver disease. Radiol Clin North Am. 2025;63(1):13-28. doi: 10.1016/j.rcl.2024.07.003.
- Kennedy P, Wagner M, Castéra L, Hong CW, Johnson CL, Sirlin CB, et al. Quantitative elastography methods in liver disease: current evidence and future directions. Radiology. 2018;286(3):738-763. doi: 10.1148/radiol.2018170601.
- Ferraioli G, Tinelli C, Lissandrin R, Zicchetti M, Dal Bello B, Filice G, et al. Point shear wave elastography method for assessing liver stiffness. World J Gastroenterol. 2014;20(16):4787-4796. doi: 10.3748/wjg.v20.i16.4787.
- Ahuja AT, Ying M, Ho SY, Antonio G, Lee YP, King AD, et al. Ultrasound of malignant cervical lymph nodes. Cancer Imaging. 2008;8(1):48-56. doi: 10.1102/1470-7330.2008.0006
- Gonzalez GA, Fernández MJ, Aleman CM, Alcantara MDC. El A, B, C de la evaluación ganglionar con ultrasonido. 33 Congreso Nacional SE-RAM; 2016 May 19 – May 22; Palacio de Congresos y de la Musica de Euskalduna. Bilbao: SERAM; 2018 Nov. 306p.
- Fischerova D, Gatti E, Culcasi C, Ng Z, Szabó G, Zanchi L, et al. Ultrasound assessment of lymph nodes for staging of gynecological cancer: consensus opinion on terminology and examination technique. Ultrasound Obstet Gynecol. 2025;65(2):206-225. doi: 10.1002/uog.29127.
- Ljung BM, Geller DA. Fine-needle aspiration techniques for biopsy of deep-seated impalpable targets: a primer for radiologists. AJR Am J Roentgenol. 1998;171(2):325-328. doi: 10.2214/ajr.171.2.9694444.
- 16. Desai PB, Desai KN, Panchal NS. Utility of the United Kingdom National Health Services Breast Screening Program Diagnostic Protocol in fineneedle aspiration cytology with cell block preparation in cases of palpable breast lumps: a reliable, fast, and accurate diagnostic method for the assessment of breast lumps with histopathologic correlation. J Midlife Health. 2024;15(2):62-68. doi: 10.4103/jmh.jmh_187_23.
- Jiang M, Bennani NN, Feldman AL. Lymphoma classification update: T-cell lymphomas, Hodgkin lymphomas, and histiocytic/dendritic cell neoplasms. Expert Rev Hematol. 2017;10(3):239-249. doi: 10.1080/17474086. 2017.1281122.
- Chae SY, Jung HN, Ryoo I, Suh S. Differentiating cervical metastatic lymphadenopathy and lymphoma by shear wave elastography. Sci Rep. 2019;9(1):12396. doi: 10.1038/s41598-019-48705-0.
- Sigrist RMS, Liau J, Kaffas AE, Chammas MC, Willmann JK. Ultrasound elastography: review of techniques and clinical applications. Theranostics. 2017;7(5):1303-1329. doi: 10.7150/thno.18650.
- Sarda-Inman ED, Valdez-Rojas AM, Ultrasound Neck Node Reporting and Data System (UNN-RADS) for lymphadenopathy: a structured report. J Mex Fed Radiol Imaging. 2022;1(3):151-163. doi: 10.24875/JMEXFRI. M22000020.
- Dudea SM, Lenghel M, Botar-Jid C, Vasilescu D, Duma M. Ultrasonography of superficial lymph nodes: benign vs. malignant. Med Ultrason. 2012;14(4):294-306.





FULL RESEARCH ARTICLE

Vascular signs of Kaiser score* on contrast-enhanced breast MRI improve prediction of malignancy in mass and non-mass breast lesions

Leyla J. Alanis-Soto^{1a}, Nancy L. Garza-Garcia^{1a}, Mane M. Ayala-Duran¹, Yesika J. Davila-Zablah¹, I. Miranda Sanchez-Carenzo¹, Maria Guerra-Ayala¹, Gabriela S. Gomez- Macias², Yara G. Flores-Raymundo², Daniel F. Lopez-Altamirano² and Margarita L. Garza-Montemayor¹

¹Diagnostic Breast Imaging Department, Zambrano Hellion; ²Department of Pathology, San Jose Hospital, TecSalud. Monterrey, Nuevo Leon. Mexico

ABSTRACT

Introduction: The modified Kaiser score (KS*) evaluates vascular signs, such as a positive adjacent vessel sign (AVS) and increased ipsilateral breast vascularity, which have independent predictive value for malignancy in breast lesions. The aim of this study was to compare the original KS and the modified KS* for the prediction of malignancy based on the presence of vascular signs in mass and non-mass breast lesions on contrast-enhanced breast magnetic resonance imaging (MRI). Material and methods: This was a retrospective cross-sectional study of women with breast cancer. Mass and nonmass lesions seen on contrast-enhanced breast MRI were scored using the original KS based on the morphologic and kinetic features of the BI-RADS lexicon. KS* was classified based on positive AVS and increased ipsilateral breast vascularity. The molecular subtypes of breast cancer were also determined. Results: A total of 476 women with breast cancer were included: 421(88.4%) with mass breast lesions and 55 (11.6%) with non-mass breast lesions. The mean age ± SD was 49.3 ± 10.9 and 51.2 ± 10.9 years, respectively. A positive AVS and increased ipsilateral breast vascularity were found in 176 (41.8%) of 421 mass lesions. The score of these mass lesions was increased by three additional points, and they were reclassified as intermediate and high risk for malignancy on the KS*. In 23 (41.8%) of 55 non-mass lesions, both vascular signs were found. Non-mass lesions were also upgraded by 3 additional points and categorized as intermediate and high-risk on the KS*. Twenty-one (91.4%) of 23 non-mass lesions with both vascular signs were reclassified as high-risk (KS* 8 to 11). Conclusion: KS* improves malignancy prediction based on vascular signs in mass and non-mass breast lesions by contrast-enhanced breast MRI. This is the first study in Mexico that confirms that the presence of vascular signs improves the KS* diagnostic stratification algorithm in identifying lesions suspicious of malignancy and indicating the need for a breast biopsy.

Keywords: Contrast-enhanced breast magnetic resonance imaging. Breast Imaging Reporting and Data System. Kaiser score. Kaiser score*. Adjacent vessel sign. Increased ipsilateral breast vascularity.

INTRODUCTION

Contrast-enhanced breast magnetic resonance imaging (MRI) is performed as a complementary examination in breast lesion diagnosis, especially in suspected

breast cancer^{1,2}. Morphologic findings of breast lesions on MRI are described in the Breast Imaging Reporting and Data System (BI-RADS) lexicon³. The Kaiser score (KS) algorithm is used to categorize the risk of malignancy based on a specific BI-RADS lexicon with scores

*Corresponding author:

Nancy L. Garza-Garcia E-mail: nancygarza@tec.mx Received for publication: 25-03-2025 Accepted for publication: 23-05-2025 DOI: 10.24875/JMEXFRI.M25000111 Available online: 10-10-2025 J Mex Fed Radiol Imaging. 2025;4(3):184-197 www.JMeXFRI.com

2696-8444 / © 2025 Federación Mexicana de Radiología e Imagen, A.C. Published by Permanyer. This is an open access article under the CC BY-NC-ND (https://creativecommons.org/licenses/by-nc-nd/4.0/).

^aThese authors contributed equally.

ranging from 1 to 11. Higher scores are associated with a higher probability of malignancy⁴⁻⁶. The KS increases the specificity of contrast-enhanced breast MRI while reducing false-positive results and decreasing the number of unnecessary breast biopsies⁷. However, its diagnostic performance varies depending on the type of lesion, mass or non-mass,¹ and lesion size (< 1 cm)⁸.

Malignant angiogenesis, characterized by abnormal, irregular vascular growth and increased capillary permeability, has been described in breast cancer². Tumor blood supply has been shown to correlate with clinical prognosis¹. The KS* was developed by integrating the original KS with the assessment of breast vascularity, including a positive adjacent vessel sign (AVS) and increased ipsilateral breast vascularity¹.

Breast lesion classification with the KS* improves malignancy prediction of breast lesions initially classified as low risk with the original KS^{1,2,9}. Vascular signs are particularly useful for predicting malignancy in the evaluation of non-mass lesions¹. The aim of this study was to compare the original KS and KS* for the prediction of malignancy based on the presence of vascular signs in mass and non-mass breast lesions on contrast-enhanced breast MRI.

MATERIAL AND METHODS

This retrospective cross-sectional study was conducted from January 2014 to December 2023 in the Breast Imaging Department of San Jose Hospital and Zambrano Hellion Hospital of TecSalud in Monterrey, Nuevo Leon, Mexico. We included all contrast-enhanced breast MRI examinations performed in patients with a breast cancer diagnosis confirmed by percutaneous breast biopsy. Patients with a breast cancer diagnosis by excisional biopsy, a history of mastectomy, radiotherapy, or bilateral breast cancer were excluded. Informed consent was not required for this retrospective analysis of data collected as part of medical care. The Institutional Research and Ethics in Research Committees approved the study.

Study development and variables

Data were obtained from the clinical records of women with a confirmed diagnosis of breast cancer who had undergone contrast-enhanced breast MRI for diagnostic and/or staging purposes within one month or less after a percutaneous breast biopsy. The decision for breast biopsy was based on mammography.

ultrasound, and/or MRI findings with BI-RADS categories 4 or 5. KS and KS* classifications were performed retrospectively.

Image acquisition and analysis

A 1.5T Magnetom Aera and a 3.0T Espree MRI scanner (Siemens Medical Solutions, Erlangen, Germany) with a dedicated breast coil were used. The following sequences were acquired: T2-weighted with fat suppression, diffusion-weighted imaging (DWI) and apparent diffusion coefficient (ADC) maps, T1-weighted spin-echo without contrast agent, and Turbo Inversion Recovery Magnitude (TIRM). After contrast administration, T1-weighted gradient echo sequences with fat suppression were performed. A gadolinium-based contrast agent, 0.1 mL/kg, was administered at an injection rate of 2 mL/s. Five T1-weighted post-contrast series with image subtraction were acquired, followed by multiplanar reformatting and maximum intensity projection (MIP). A kinetic curve analysis was performed, and peak enhancement index (PEI) values were determined. The contrast-enhanced breast MRI images were stored in a Picture Archiving and Communication System (PACS) (Carestream, Phillips, Rochester, NY, USA). A radiologist (NGG) with 16 years of experience in breast imaging performed the image analysis.

Mass and non-mass lesions were scored using the KS based on the morphologic and kinetic features of the BI-RADS lexicon. These descriptors were the root sign (presence or absence of spiculations), enhancement curve (type 1, 2, or 3), lesion margin (irregular or circumscribed), internal enhancement pattern, and edema. The KS score was calculated using a virtual calculator available at https://school-of-radiology.com/kaiserscore/10. Based on the total score, lesions were classified to define malignancy risk and their relationship to BI-RADS: KS 1 to 4, low risk, BI-RADS 2 or 3; KS 5 to 7, intermediate risk, BI-RADS 4; and KS 8 to 11, high risk, BI-RADS 5.

For KS* breast vasculature assessment, AVS was defined as the presence of vessels either entering the lesion or in contact with the edge of the lesion, clearly delineated on the subtraction images^{1,11}. Vessels with a length \geq 3 cm and a diameter \geq 2 mm were counted for the breast with the lesion and the contralateral breast on the MIP images. If the number of vessels in the lesion-bearing breast was two or more than those in the contralateral breast, this was categorized as increased ipsilateral breast vascularity¹. In cases where

a breast lesion had a KS \leq 7 but simultaneously had positive AVS and increased ipsilateral breast vascularity, the KS was increased by 3 points, thereby modifying the final score. The KS* range remained from 1 to 11, aligning with the original KS framework¹.

Molecular breast cancer subtypes

Tumor biopsies were stained for estrogen receptor (ER), progesterone receptor (PR), and human epidermal growth factor receptor 2 (HER2) using a Ventana BenchMark GX Autostainer with validated internal protocols. An external positive control tissue was included in each run. ER and PR were classified as positive if nuclear staining was >1% according to ASCO/CAP guidelines¹². HER2 assessment was performed according to the 2023 ASCO/CAP HER2 test update¹².

Histopathologic workup

Breast lesions identified as BI-RADS 4 or 5 that underwent image-guided or surgical breast biopsy were evaluated by a breast pathologist (GGM) with 14 years of experience. The diagnostic criteria for histopathological diagnosis were based on the fifth edition of the WHO classification of breast tumors¹³.

Statistical analysis

Measures of central tendency and dispersion were used to summarize numerical variables, and absolute numbers and percentages for categorical variables. The association between unrelated categorical variables was assessed using the chi-square test. The p value < 0.05 was statistically significant. SPSS v.25 (IBM Corp., Armonk, NY, USA) was used for data analysis.

RESULTS

A total of 476 women with breast cancer were included: 421 (88.4%) had mass lesions and 55 (11.6%) had non-mass lesions. The mean age \pm SD was 49.3 \pm 10.9 and 51.2 \pm 10.9 years, respectively.

Contrast-enhanced breast MRI findings in mass lesions with or without vascular signs in women with breast cancer

The contrast-enhanced breast MRI findings in 418 of the 421 mass lesions in women with breast cancer with or without vascular signs are shown in Table 1. Three cases with only increased ipsilateral vascularity without AVS were not included. The shape, margin, type of enhancement, kinetic curve, and root sign of the mass breast lesions with or without vascular signs were not significantly different. Mass lesions with both vascular signs, AVS positive and increased ipsilateral breast vascularity (n = 176/418) had a higher frequency of masses (n = 120/176, 68.1%) with larger size (\geq 21 mm). In contrast, in 44 patients without vascular signs, 68.0% (n = 30/44) had small masses (\leq 20 mm) (p = 0.001). The presence of edema was observed in 23.4% (98/418) of the masses. Absence of edema was significantly more common in cases without vascular signs (n = 40/44, 90.9%) (p = 0.003).

Contrast-enhanced breast MRI findings in non-mass lesions with or without vascular signs in women with breast cancer

The contrast-enhanced breast MRI of 55 non-mass lesions in women with breast cancer with or without vascular signs is shown in table 2. Both vascular signs were found in 23 (42.0%), with a regional distribution pattern (n = 11/23, 47.8%) (p = 0.015) and a size > 51 mm (n = 16/23, 69.6%) (p = 0.001) being more significant. The absence of vascular signs, observed in 9.1% of cases (n = 5/55), was significantly associated with small, non-mass lesions (< 20 mm) (p < 0.001). There were no significant differences in the type of enhancement, kinetic curve, edema, or margin with the presence or absence of vascular signs. An increase in root sign was found in cases with a positive AVS and increased ipsilateral breast vascularity, although this difference was not significant.

Upgrading from KS to KS* based on the presence of vascular signs in women with breast cancer

Both vascular signs, positive AVS and increased ipsilateral breast vascularity, were found in 176 (41.8%) of 421 mass lesions on contrast-enhanced breast MRI (Table 3A). The score of these mass lesions was increased by 3 additional points, and they were reclassified as intermediate-risk and high-risk for malignancy on the KS*. There was no mass lesion in the low-risk category (KS* 1 to 4). Both vascular signs were found in 158 (89.8%) of 176 mass breast lesions with KS* 8 to 11, with a high risk of malignancy.

Table 1. Contrast-enhanced breast MRI findings in 418° mass lesions with or without vascular signs in women with breast cancer

Descriptor	Total (n = 418)	Positive AVS (n = 198)	Positive AVS and increased ipsilateral breast vascularity, (n = 176)	No vascular signs (n = 44)	р
Shape, n (%)					0.219
Oval	20 (4.8)	9 (4.5)	6 (3.4)	5 (11.4)	
Round	34 (8.1)	14 (7.1)	17 (9.7)	3 (6.8)	
Irregular	364 (87.1)	175 (88.4)	153 (86.9)	36 (81.8)	
Margin, n (%)					0.258
Circumscribed	13 (3.1)	5 (2.5)	5 (2.8)	3 (6.8)	
Spiculated	181 (43.3)	79 (39.9)	85 (48.3)	17 (38.6)	
Irregular	224 (53.6)	114 (57.6)	86 (48.9)	24 (54.5)	
Enhancement, n (%)					0.470
Homogeneous	54 (12.9)	30 (15.2)	16 (9.1)	8 (18.2)	
Heterogeneous	267 (63.9)	123 (62.1)	117 (66.5)	27 (61.4)	
Rim shape	96 (23.0)	45 (22.7)	42 (23.9)	9 (20.5)	
Dark internal septation	1 (0.2)	0	1 (0.6)	0	
Main lesion size, n (%)					0.001
2 to 20 mm	185 (44.3)	99 (50.0)	56 (31.8)	30 (68.2)	
> 21 to 50 mm	210 (50.2)	94 (47.5)	102 (58.0)	14 (31.8)	
> 51 mm	23 (5.5)	5 (2.5)	18 (10.2)	0	
Kinetic curve, n (%)					0.223
Type 1	48 (11.5)	26 (13.1)	18 (10.2)	4 (9.1)	
Type 2	210 (50.2)	94 (47.5)	87 (49.4)	29 (65.9)	
Type 3	160 (38.3)	78 (39.4)	71 (40.3)	11 (25.0)	
Root sign, n (%)					0.211
Yes	181 (43.3)	79 (39.9)	85 (48.3)	17 (38.6)	
No	237 (56.7)	119 (60.1)	91 (51.7)	27 (61.4)	
Edema, n (%)					0.003
Yes	98 (23.4)	40 (20.2)	54 (30.7)	4 (9.1)	
No	320 (76.6)	158 (79.8)	122 (69.3)	40 (90.9)	

aThree women with only increased ipsilateral breast vascularity were not included. AVS: adjacent vessel sign. KS: Kaiser score; KS*: modified Kaiser score.

Both vascular signs were found on contrast-enhanced breast MRI in 23 (41.8%) of 55 non-mass lesions (Table 3B). These lesions were upgraded by 3 additional points and were categorized as intermediate-and high-risk groups on KS*. Twenty-one (91.4%) of 23 non-mass lesions with both vascular signs were reclassified with high scores (KS* 8-11). Only one non-mass lesion remained in the low-risk category.

Molecular subtypes in mass and non-mass breast lesions in women with breast cancer

The distribution of molecular subtypes was comparable between mass and non-mass breast lesions (Table 4). The luminal A molecular subtype was more common, with 154 (36.6%) of 421 mass lesions and 26 (47.3%) of 55 non-mass lesions. The triple-negative

Table 2. Contrast-enhanced breast MRI findings in 55 non-mass lesions with or without vascular signs in women with breast cancer

Descriptor	Total (n = 55)	Positive AVS (n = 27)	Positive AVS and increased ipsilateral breast vascularity, (n = 23)	No vascular signs (n = 5)	р
Enhancement, n (%)					0.601
Homogeneous	3 (5.5)	3 (11.1)	0	0	
Heterogeneous	32 (58.2)	14 (51.9)	14 (60.9)	4 (80.0)	
Clumped	17 (30.9)	8 (29.6)	8 (34.8)	1 (20.0)	
Cluster ring	3 (5.5)	2 (7.4)	1 (4.3)	0	
Distribution, n (%)					0.015
Focal	21 (38.2)	13 (48.1)	4 (17.4)	4 (80.0)	
Lineal	8 (14.5)	5 (18.5)	2 (8.7)	1 (20.0)	
Segmental	12 (21.8)	6 (22.2)	6 (26.1)	0	
Regional	14 (25.5)	3 (11.1)	11 (47.8)	0	
Main lesion size, n (%)					0.001
2 to 20 mm	11 (20.0)	5 (18.5)	1 (4.3)	5 (100)	
> 21 to 50 mm	21 (38.2)	15 (55.6)	6 (26.1)	0	
> 51 mm	23 (41.8)	7 (25.9)	16 (69.6)	0	
Kinetic curve, n (%)					0.416
Type 1	15 (27.3)	8 (29.6)	7 (30.4)	0	
Type 2	24 (43.6)	12 (44.4)	8 (34.8)	4 (80.0)	
Type 3	16 (29.1)	7 (25.9)	8 (34.8)	1 (20.0)	
Root sign, n (%)					0.234
Yes	36 (65.5)	15 (55.6)	18 (78.3)	3 (60.0)	
No	19 (34.5)	12 (44.4)	5 (21.7)	2 (40.0)	
Edema, n (%)					0.317
Yes	17 (30.9)	7 (25.9)	7 (30.4)	3 (60.0)	
No	38 (69.1)	20 (74.1)	16 (69.6)	2 (40.0)	
Margin, n (%)					0.646
Circumscribed	6 (10.9)	2 (7.4)	3 (13.0)	1 (20.0)	
Non-circumscribed	49 (89.1)	25 (92.6)	20 (87.0)	4 (80.0)	

AVS: adjacent vessel sign; KS: Kaiser score; KS*: modified Kaiser score.

molecular subtype was significantly more common in mass lesions (n = 70/421, 16.6%) than in non-mass lesions (n = 1/55, 1.8%) (p = 0.004).

Association of KS and KS* with molecular subtypes of mass lesions in women with breast cancer

Of the 421 mass lesions, 48 (11.4%) were categorized as low risk, 195 (46.3%) as intermediate risk, and

178 (42.3%) as high risk for malignancy by KS (Table 5A). No significant association was found between molecular subtype and malignancy risk in KS. However, the majority of mass lesions of all molecular subtypes were categorized as intermediate (n = 195/421, 46.3%) or high malignancy risk (n = 178/421, 42.3%).

Among the 421 mass breast lesions, a subgroup of 176 showed both vascular signs on contrast-enhanced breast MRI and were classified with KS* (Table 5B).

Table 3A. Upgrade from KS to KS* based on the presence of vascular signs in mass lesions on contrast-enhanced breast MRI in women with breast cancer

KS			KS*				
1 to 4	5 to 7	8 to 11	Total	1 to 4	5 to 7	8 to 11	Total
48 (11.5%)	195 (46.3%)	178 (42.3%)	421	0	18 (10.2%)	158 (89.8)	176ª

^aA subgroup of 176 (41.8%) of the 421 mass lesions had both vascular signs; these were upgraded by 3 additional points. As a result, none of the lesions remained in the low-risk category (KS* 1–4). MRI: magnetic resonance imaging; KS: Kaiser score; KS*: modified Kaiser score.

Table 3B. Upgrade from KS to KS* based on the presence of vascular signs in non-mass lesions on contrast-enhanced breast MRI in women with breast cancer

KS			KS*				
1 to 4 5 to 7 8 to 11 Total				1 to 4	5 to 7	8 to 11	Total
9 (16.3%)	26 (47.3)	20 (36.4%)	55	1 (4.3%)	1 (4.3%)	21 (91.4%)	23ª

^aA subgroup of 23 (41.8%) of the 55 non-mass lesions had both vascular signs; these were upgraded by 3 additional points on the KS*. As a result, only one non-mass lesion remained in the low-risk category (KS* 1–4). MRI: magnetic resonance imaging; KS: Kaiser score; KS*: modified Kaiser score.

Table 4. Molecular subtypes in mass and non-mass lesions in women with breast cancer

Description	Mass breast lesions, (n = 421)	Non-mass breast lesions, (n = 55)
Luminal A, n (%)	154 (36.6)	26 (47.3)
Luminal B, n (%)	119 (28.3)	13 (23.6)
Luminal B HER2+, n (%)	33 (7.8)	7 (12.7)
HER2+, n (%)	29 (6.9)	5 (9.1)
Triple-negative, n (%)	70 (16.6)	1 (1.8)
HER2-low, n (%)	16 (3.8)	3 (5.5)

HER2+: human epidermal growth factor receptor 2.

These lesions received an upgrade of 3 additional points. As a result, none of the lesions remained in the low-risk (KS* 1 to 4). The high-risk category was elevated in all molecular subtypes (range 75.8% to 94.4%).

Figure 1 shows a contrast-enhanced breast MRI in a 41-year-old woman with a mass lesion with positive AVS and increased ipsilateral breast vascularity. This mass was classified as a BI-RADS category 2 and a KS of 2, corresponding to a low risk of malignancy. In addition, 3 points were assigned based on the presence

of vascular signs, resulting in a KS* of 5 corresponding to an intermediate risk of malignancy, BI-RADS category 4. The histopathologic diagnosis was invasive non-special type (NST) carcinoma, molecular subtype luminal A.

Figure 2 shows a contrast-enhanced breast MRI of a 41-year-old woman with a non-mass lesion, BI-RADS category 2, and a KS of 1, corresponding to a low risk of malignancy. Three points were assigned based on the positive AVS and increased ipsilateral breast vascularity, resulting in a KS* of 4, corresponding to a low risk of malignancy, BI-RADS category 2. A breast biopsy was ordered due to calcifications in the right breast detected by mammography (not shown). The histopathologic diagnosis of the non-mass lesion in the right breast was invasive NST carcinoma, molecular subtype luminal B, with an associated *in situ* carcinoma.

Figure 3 shows a contrast-enhanced breast MRI in a 52-year-old woman with a mass lesion with positive AVS and increased ipsilateral breast vascularity. This mass was classified as BI-RADS category 2, with a KS of 2, corresponding to a low risk of malignancy. Three points were assigned based on the presence of vascular signs, resulting in a KS* of 5, corresponding to an intermediate risk of malignancy, BI-RADS category 4. The histopathologic diagnosis was invasive NST carcinoma with basaloid features, molecular subtype triple-negative.

Table 5A. Association of KS with molecular subtypes of mass lesions in women with breast cancer

Description	Total, n	KS		р	
	_	1 to 4	5 to 7	8 to 11	_
Luminal A, n (%)	154	16 (10.4)	80 (51.9)	58 (37.7)	0.374
Luminal B, n (%)	119	10 (8.4)	58 (48.7)	51 (42.9)	0.577
Luminal B HER2+, n (%)	33	4 (12.1)	13 (39.4)	16 (48.5)	0.720
HER2+, n (%)	29	2 (6.9)	11 (37.9)	16 (55.2)	0.351
Triple-negative, n (%)	70	13 (18.6)	25 (35.7)	32 (45.7)	0.080
HER2-low, n (%)	16	3 (18.8)	8 (50.0)	5 (31.3)	0.531

HER2+: human epidermal growth factor receptor 2; KS: Kaiser score.

Table 5B. Association of KS* with molecular subtypes of mass lesions^a in women with breast cancer

Description	Total, n	KS*			р
	_	1 to 4	5 to 7	8 to 11	-
Luminal A, n (%)	54	0	3 (5.6)	51 (94.4)	0.257
Luminal B, n (%)	54	0	3 (5.6)	51 (94.4)	0.257
Luminal B HER2+, n (%)	18	0	2 (11.1)	16 (88.9)	0.902
HER2+, n (%)	13	0	2 (15.4)	11 (84.6)	0.539
Triple-negative, n (%)	33	0	8 (24.2)	25 (75.8)	0.008
HER2-low, n (%)	4	0	0	4 (100)	0.500

^aA subgroup of 176 (41.8%) of the 421 mass lesions had both vascular signs; these were upgraded by 3 additional points. As a result, none of the lesions remained in the low-risk category (KS* 1 to 4). HER2+: human epidermal growth factor receptor 2; KS*: modified Kaiser score.

Association of KS and KS* with molecular subtypes of non-mass lesions in women with breast cancer

Nine (16.4%) of 55 non-mass lesions were categorized as low risk, 26 (47.3%) as intermediate risk, and 20 (36.3%) as high risk in KS (Table 6A). Only luminal A, luminal B, and HER2+ molecular subtypes had low-risk KS lesions. No significant association was found between the molecular subtype and risk of malignancy categorized by KS.

Of 55 non-mass breast lesions, 23 (41.8%) had both vascular signs on contrast-enhanced breast MRI (Table 6B). Twenty-one (91.3%) of the 23 were categorized in the high-risk category (KS* 8 to 11), similar to the mass lesions. Figure 4 shows a contrast-enhanced

breast MRI of a 67-year-old woman with a non-mass lesion enhancement classified as BI-RADS category 3 and a KS of 4 with a low risk of malignancy. Three points were assigned based on the presence of vascular signs, resulting in a KS* of 7, corresponding to an intermediate risk of malignancy, BI-RADS category 4. The diagnosis was high-grade DCIS of the solid, comedo, and cribriform type, with a HER2-positive molecular subtype.

DISCUSSION

Our study showed that KS* improved malignancy prediction by contrast-enhanced breast MRI based on the presence of vascular signs in both mass and non-mass breast lesions. This is the first study in Mexico to confirm that the presence of vascular signs optimizes the

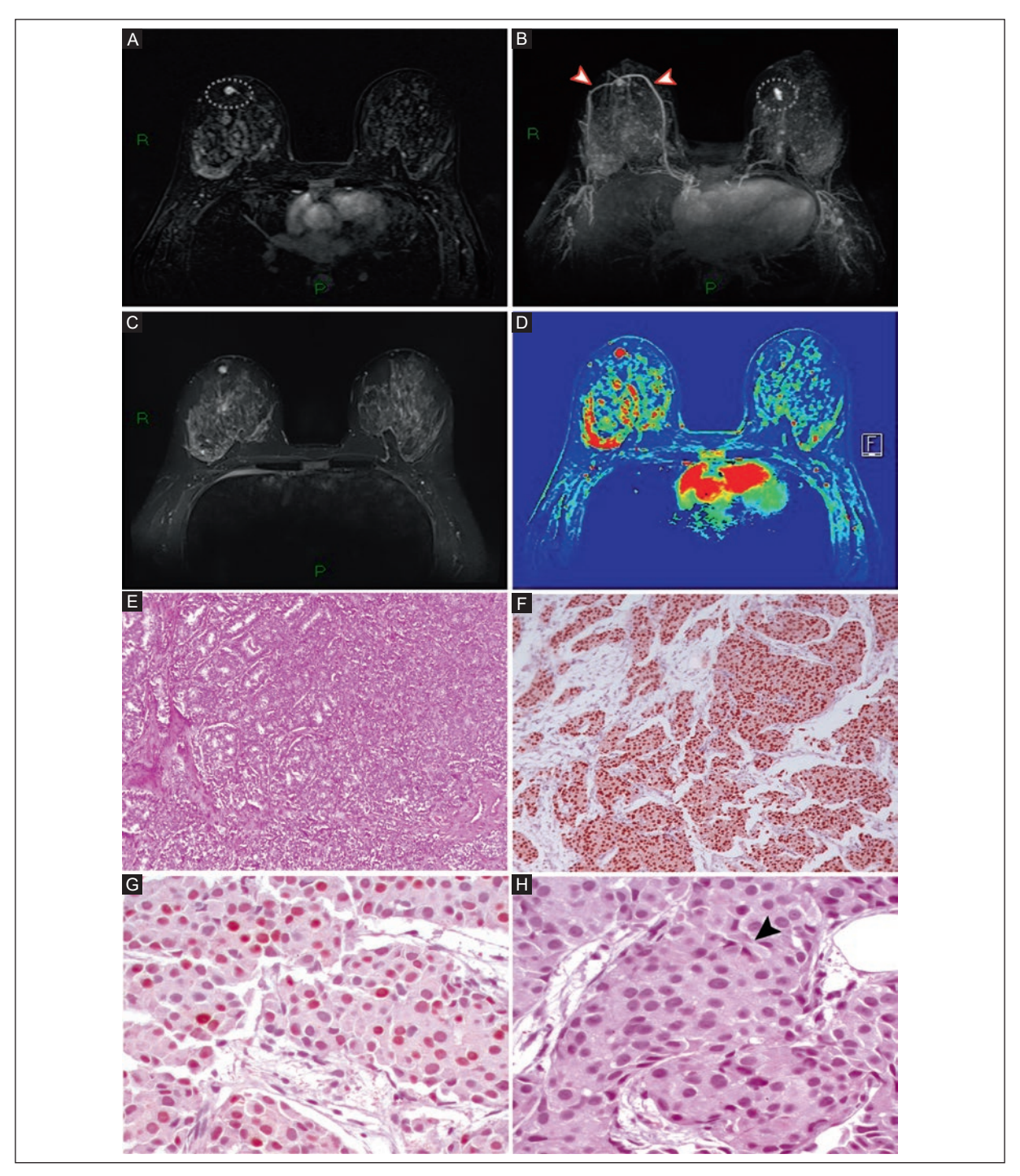


Figure 1. Contrast-enhanced breast MRI of a 41-year-old woman. **A**: T1 DCE sequence with gadolinium demonstrates a round mass with circumscribed margins and ring enhancement in the upper outer quadrant of the right breast (dotted circle). **B**: MIP image demonstrates a right breast mass with a positive AVS and increased ipsilateral breast vascularity (red arrowheads). In the left breast, a hyperenhanced solid mass without vascular signs is also observed, corresponding to a previously diagnosed fibroadenoma confirmed by histopathology (dashed circle). **C**: there is no perilesional edema on the TIRM sequence. **D**: PEI and the correlation of time—signal intensity curves of the main lesion in the right breast shows a type 2 plateau curve (not shown). This mass breast lesion was classified as BI-RADS category 2, and KS 2, with a low risk of malignancy. Three points were assigned based on the presence of vascular signs, resulting in a KS* of 5, with an intermediate risk of malignancy, BI-RADS category 4. **E**: H&E 10X, nests of neoplastic cells with sparse lumen formation. The cells have nuclear pleomorphism and frequent mitoses. **F**: ER (5X) 100% nuclear expression, with strong intensity. **G**: PR (10X) 100% nuclear expression, with strong intensity. **H**: HER-2 (10X) negative membrane staining (0+) (black arrowhead). The histopathologic diagnosis was invasive NST carcinoma, luminal A molecular subtype.

AVS: adjacent vessel sign; KS: Kaiser score; KS*: modified Kaiser score; BI-RADS: Breast Imaging Reporting and Data System; DCE: dynamic contrast-enhanced; Gd: gadolinium; MIP: maximum intensity projection; MRI: magnetic resonance imaging; PEI: positive enhancement integral; TIRM: turbo inversion recovery magnitude; NST: non-special type; H&E: hematoxylin and eosin; ER: estrogen receptor; PR: progesterone receptor; HER-2: human epidermal growth factor receptor 2.

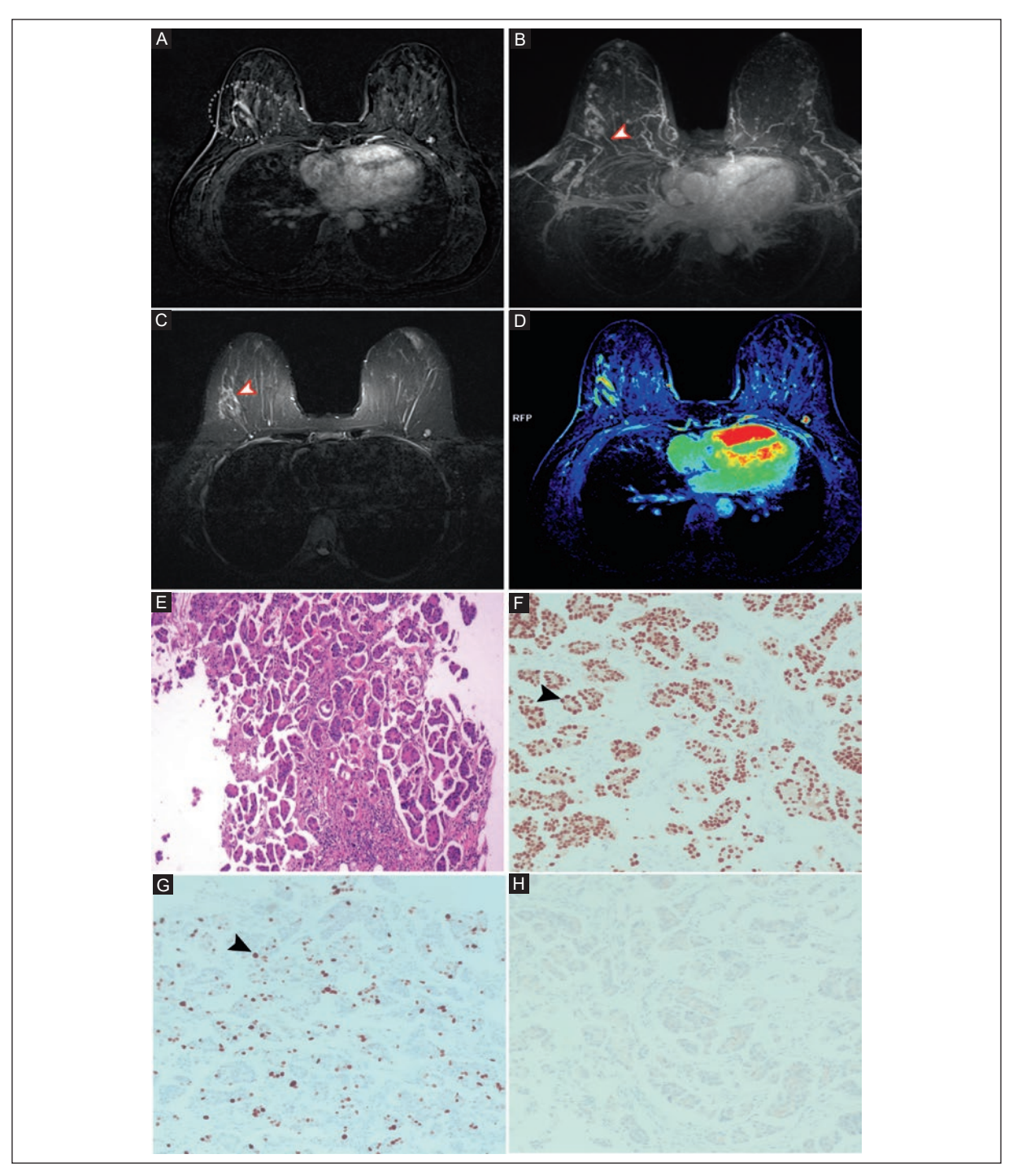


Figure 2. Contrast-enhanced breast MRI of a 41-year-old woman. **A:** T1 DCE sequence with Gd shows a non-mass lesion with a circumscribed margin and cobblestone enhancement in the upper outer quadrant of the right breast (dotted circle). **B:** MIP shows a non-mass lesion in the right breast with positive AVS and increased ipsilateral breast vascularity (red arrowhead). **C:** perilesional edema is seen on the TIRM sequence (red arrowhead). **D:** PEI and the correlation of time—signal intensity curves of the main lesion with a persistent type 1 curve (not shown). This non-mass lesion was classified as BI-RADS category 2, KS 1, with a low risk of malignancy. Three points were assigned based on the positive AVS and increased ipsilateral breast vascularity, resulting in a KS* of 4 with a low risk of malignancy, BI-RADS category 2. Breast biopsy was indicated due to calcifications in the right breast detected by mammography (not shown). **E:** H&E 5X, nests of neoplastic cells with reversed polarity and stromal retraction. **F:** ER 5X, 100% nuclear expression with strong intensity (black arrowhead). **G:** PR 5X, 100% nuclear expression with strong intensity (black arrowhead). **H:** HER-2 5X, partial and weak membrane staining (1+). The histopathologic diagnosis of the non-mass lesion in the right breast was invasive NST carcinoma, luminal B molecular subtype, with associated in situ carcinoma.

AVS: adjacent vessel sign; KS: Kaiser score; KS*: modified Kaiser score; BI-RADS: Breast Imaging Reporting and Data System; DCE: dynamic contrast-enhanced; Gd: gadolinium; MIP: maximum intensity projection; MRI: magnetic resonance imaging; PEI: positive enhancement integral; TIRM: turbo inversion recovery magnitude; NST: not-special type; H&E: hematoxylin and eosin; ER: estrogen receptor; PR: progesterone receptor; HER-2: human epidermal growth factor receptor 2.

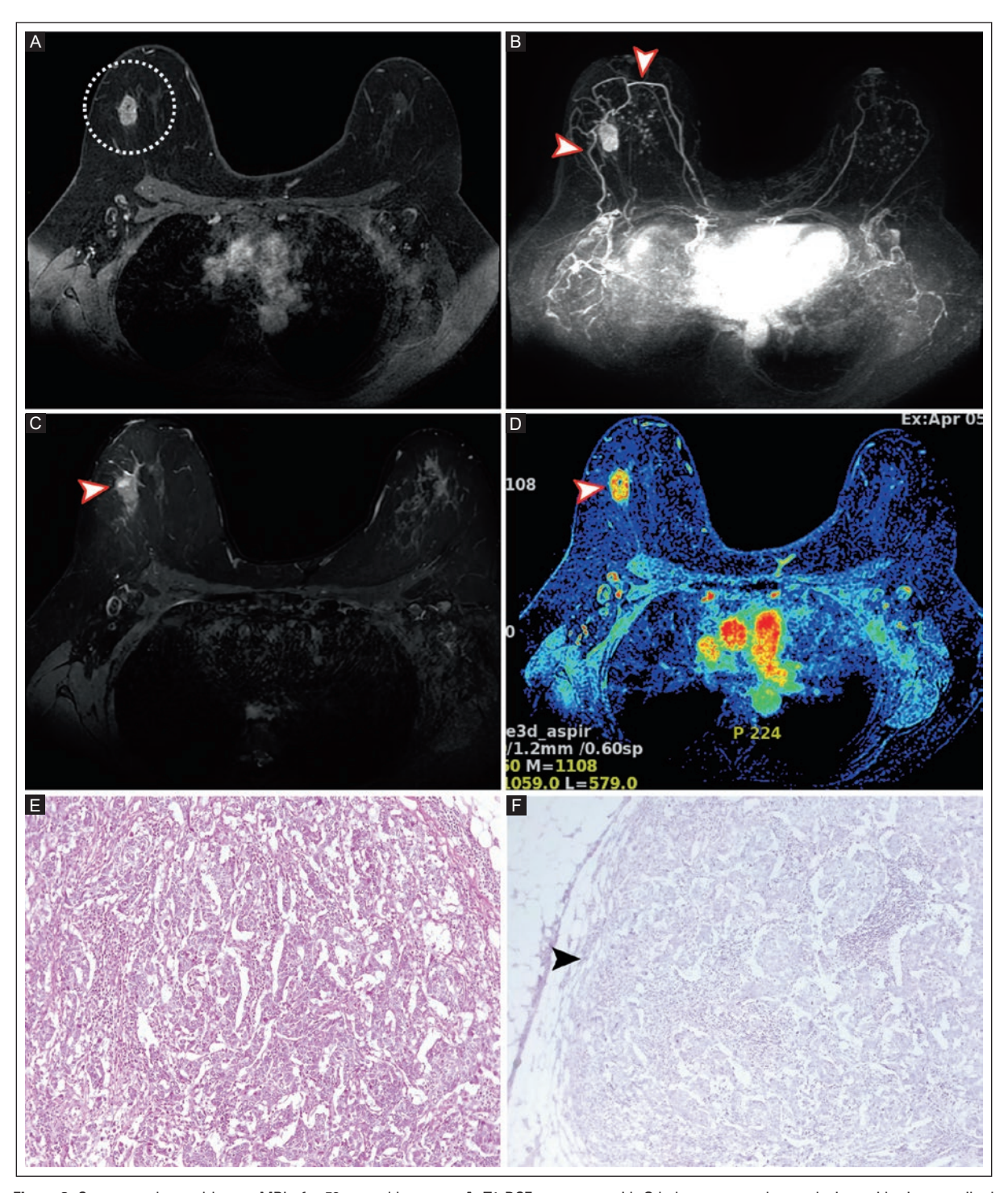


Figure 3. Contrast-enhanced breast MRI of a 52-year-old woman. A: T1 DCE sequence with Gd shows a round mass lesion, with circumscribed margins and homogeneous enhancement in the upper outer quadrant of the right breast (dotted circle). B: MIP shows a mass lesion of the right breast with positive AVS and increased ipsilateral breast vascularity (red arrowheads). C: there is no perilesional edema in the TIRM sequence (red arrowhead). D: PEI and the correlation of time—signal intensity curves of the breast lesion with a type 2 plateau curve (not shown). This mass was classified as BI-RADS category 2, KS 2, with a low risk of malignancy. Three points were assigned based on the presence of vascular signs, resulting in a KS* of 5, with an intermediate risk of malignancy, BI-RADS category 4. E: H&E 10X, nests of neoplastic cells with sparse lumen formation, nuclear pleomorphism, and frequent mitoses. F: ER 5X, negative expression. PR 5X, negative expression. HER2 5X, negative expression (black arrowhead). The histopathologic diagnosis was invasive NST carcinoma with basaloid features, triple-negative molecular subtype.

AVS: adjacent vessel sign; KS: Kaiser score; KS*: modified Kaiser score; BI-RADS: Breast Imaging Reporting and Data System; DCE: dynamic contrast-enhanced; Gd: gadolinium; MIP: maximum intensity projection; MRI: magnetic resonance imaging; PEI: positive enhancement integral; TIRM: turbo inversion recovery magnitude; NST: non-special type; H&E: hematoxylin and eosin; ER: estrogen receptor; PR: progesterone receptor; HER-2: human epidermal growth factor receptor 2.

Table 6A. Association of KS with molecular subtypes of non-mass lesions in women with breast cancer

Description	Total, n	KS			р
		1 to 4	5 to 7	8 to 11	
Luminal A, n (%)	26	6 (23.1)	11 (42.3)	9 (34.6)	0.437
Luminal B, n (%)	13	2 (15.4)	7 (53.8)	4 (30.8)	0.856
Luminal B HER2+, n (%)	7	0	4 (57.1)	3 (42.9)	0.456
HER2+, n (%)	5	1 (20.0)	2 (40.0)	2 (40.0)	0.939
Triple-negative, n (%)	1	0	0	1 (100)	0.410
HER2-low, n (%)	3	0	2 (66.7)	1 (33.3)	0.677

HER2+: human epidermal growth factor receptor 2. KS: Kaiser score.

Table 6B. Association of KS* with molecular subtypes of non-mass lesions in women with breast cancer

Description	Total, n	KS*			р
	_	1 to 4	5 to 7	8 to 11	_
Luminal A, n (%)	9	0	0	9 (100)	0.495
Luminal B, n (%)	5	1 (20.0)	0	4 (80.0)	0.138
Luminal B HER2+, n (%)	4	0	0	4 (100)	0.794
HER2+, n (%)	3	0	1 (33.3)	2 (66.7)	0.030
Triple-negative, n (%)	1	0	0	1 (100)	0.951
HER2-low, n (%)	1	0	0	1 (100)	0.950

⁸A subgroup of 23 (41.8%) of the 55 non-mass lesions had both vascular signs; there were upgraded by 3 additional points in the KS*. As a result, only one non-mass lesion remained in the low score category (KS* 1 to 4). HER2+: human epidermal growth factor receptor 2; KS*: modified Kaiser score.

KS* diagnostic stratification algorithm that identifies lesions with suspected malignancy and indicates the need for breast biopsy. The breast lesion scores were initially categorized as low risk, with the KS* increased due to positive AVS and increased ipsilateral breast vascularity. They were subsequently reclassified as intermediate and high risk for malignancy with KS*.

Positive AVS and increased ipsilateral breast vascularity improve the diagnostic performance of KS* in predicting breast lesion malignancy^{1,10,14}. In our study, the presence of both vascular signs was associated with significantly higher KS* scores in both mass and nonmass lesions. Dietzel et al.¹⁴, in a retrospective study in German women, analyzed 1,084 breast lesions. A positive AVS was significantly associated with malignancy (p < 0.001). Lesions larger than 20 mm were more likely to have a positive AVS than those smaller than 20 mm

(p < 0.0001). Zhou et al. examined 223 breast lesions with suspected malignancy by contrast-enhanced breast MRI with a histopathologic diagnosis. There were 119 (53.4%) benign and 104 (46.6%) malignant lesions. Eighty-five (51.8%) of 164 mass lesions and 19 (32.2%) of 59 non-mass lesions were malignant. In the ROC curve, the AUC of KS* was 0.877 and of KS, 0.858 (p = 0.016). In non-mass lesions, the AUC was 0.793, and KS was 0.725 (p = 0.029). The combination of KS with vascular signs (KS*) significantly improves the diagnostic performance in differentiating benign and malignant breast lesions, especially in non-mass lesions. Positive AVS and increased ipsilateral breast vascularity were significantly associated with malignancy. Our study of 476 women with breast cancer evaluated with contrast-enhanced breast MRI with histopathologic confirmation and reclassification of breast lesions into

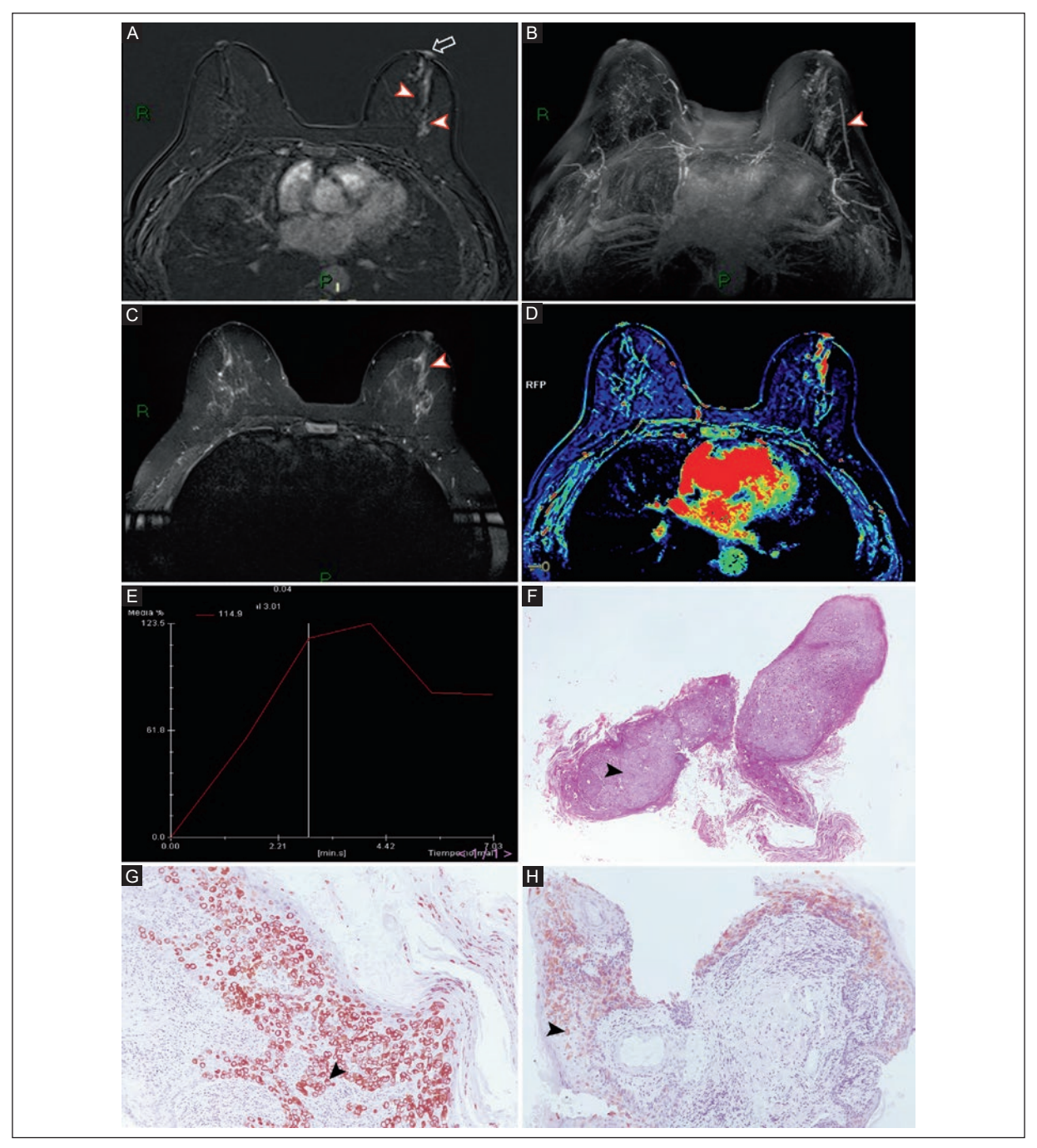


Figure 4. Contrast-enhanced breast MRI of a 67-year-old woman. A: T1 DCE sequence with Gd shows non-mass enhancement with a circumscribed margin and cobblestone-like enhancement with linear distribution in the retroareolar region of the left breast (red arrowheads). Note the nipple enhancement (white arrow). B: MIP image shows a non-mass lesion in the left breast with positive AVS and increased ipsilateral breast vascularity (red arrowhead). C: there is no perilesional edema in the TIRM sequence (red arrowhead). D-E: dynamic post-contrast image with time—signal intensity curve analysis of the primary lesion shows a type 3 washout curve. This non-mass lesion was classified as KS 4 with a low risk of malignancy. Three points were assigned based on the presence of vascular signs, resulting in a KS* of 7, with an intermediate risk of malignancy, BI-RADS category 4. A left breast mastectomy revealed a high-grade DCIS with solid, comedo-like, cribriform architecture, classified as a HER2-positive molecular subtype. There is no dermal infiltration. Paget's disease was present on the nipple. F: H&E 5X, proliferation of malignant intraepidermal glandular epithelial cells. Cells with abundant eosinophilic cytoplasm and pleomorphic nuclei (black arrowhead). G: ER: CK7 (5X), positive membranous expression (black arrowhead).

AVS: adjacent vessel sign; KS: Kaiser score; KS*: Kaiser score*; BI-RADS: Breast Imaging Reporting and Data System; DCE: dynamic contrast-enhanced; Gd: gadolinium; MIP: maximum intensity projection; MRI: magnetic resonance imaging; PEI: positive enhancement integral; TIRM: turbo inversion recovery magnitude; NST: non-special type; DCIS: ductal carcinoma in situ; H&E: hematoxylin and eosin; ER: estrogen receptor; PR: progesterone receptor; CK7: cytokeratin 7; HER-2: human epidermal growth factor receptor 2.

intermediate- and high-risk KS* based on positive AVS and increased ipsilateral breast vascularity increased the prediction of malignancy in lesions originally classified as low-risk. These results highlight the importance of evaluating not only the morphological and dynamic features of breast lesions on contrast-enhanced breast MRI, but also vascular signs, since these provide additional information about their malignant behavior.

Benign and malignant breast lesions may show nonmass enhancement on MRI. KS is less accurate in predicting malignancy in non-mass lesions. Therefore. the addition of vascular signs indicative of abnormal vascularity guides the diagnosis of malignancy¹. In our study, the presence of vascular signs in the KS* algorithm significantly increased the risk classification of malignancy. In mass lesions with both vascular signs, 158 (89.8%) of 176 mass breast lesions with KS* of 8 to 11 were at high risk of malignancy. None of these KS* lesions were classified as low risk. Twenty-one (91.4%) of 23 non-mass lesions with both vascular signs were reclassified as high risk (KS* 8 to 11), and only one non-mass lesion remained in the low-risk category. KS* with assessment of vascular signs increases the accuracy in predicting the malignancy of mass and non-mass breast lesions, especially lesions that could initially be underestimated with BI-RADS category 2 or 3 morphologic criteria. KS* can reduce false-negative results and support the indication for a breast biopsy in lesions with vascular signs.

Angiogenesis is critical in the development and spread of breast cancer and can vary depending on the molecular subtype¹⁵. Çetinkaya et al.¹⁶, in a retrospective study of 124 Turkish women examined with contrastenhanced breast MRI 1.5T with positive AVS, found 105 (78.9%) of 133 breast lesions suspicious for malignancy. No significant association was found between positive AVS and molecular subtypes. Bujor et al. 17 showed that the more aggressive molecular subtypes, HER2-positive and triple negative, had more blood vessels in the tumor compared to the luminal A and B molecular subtypes. In contrast, the luminal A molecular subtype, which has a better prognosis, has less angiogenic activity¹⁷. In our study of mass and non-mass breast lesions, the absence of vascular signs was predominant in the luminal A molecular subtype. This observation is consistent with a previous report indicating less angiogenesis and less prominent vascular patterns in luminal A tumors¹⁷. This finding contrasts with more aggressive molecular subtypes that exhibit greater vascularity. Our results reinforce the hypothesis that vascular signs may act as different functional biomarkers depending on the molecular tumor profile, especially in aggressive molecular subtypes that tend to show distinct vascular patterns.

One of the major strengths of this study is the sample size, which included 473 lesions in women with breast cancer and allowed for a robust and stratified analysis. This study also addressed the association between KS* and molecular subtypes, an aspect that has been scarcely explored. The weaknesses of this study are related to its single-center retrospective design. The sample size of non-mass lesions (n = 55) was small. In addition, only malignant cases were included, so it was not possible to determine the diagnostic performance of the KS* and its accuracy in distinguishing between benign and malignant lesions. Intraobserver and interobserver agreement were not assessed.

CONCLUSION

In our study, KS* increased the prediction of malignancy compared to KS, based on the presence of vascular signs in mass and non-mass breast lesions by contrast-enhanced breast MRI. Systematic evaluation of breast lesions with the KS* is recommended to optimize clinical decision making, especially the indication for a breast biopsy. The KS* is based on visual signs for assessing contrast-enhanced breast MRI. These signs are easily applicable in daily clinical practice without specialized software.

Acknowledgments

The authors thank Professor Ana M. Contreras-Navarro for her guidance in preparing and writing this scientific paper.

Funding

The authors declare that they have not received funding.

Conflicts of interest

The authors declare no conflicts of interest.

Ethical considerations

Protection of humans and animals. The authors declare that the procedures followed complied with the ethical standards of the responsible human experimentation committee and adhered to the World Medical

Association and the Declaration of Helsinki (1964). The procedures were approved by the institutional Ethics Committee.

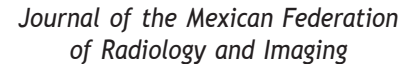
Confidentiality, informed consent, and ethical approval. The authors have obtained approval from the Ethics Committee for the analysis of routinely obtained and anonymized clinical data, so informed consent was not necessary.

Declaration on the use of artificial intelligence. The authors declare that no generative artificial intelligence was used in the writing of this manuscript.

REFERENCES

- Zhou XZ, Liu LH, He S, Chen LP, Deng C, Li SL, et al. Diagnostic value of Kaiser score combined with breast vascular assessment from breast MRI for the characterization of breast lesions. Front Oncol. 2023;13: 1165405. doi:10.3389/fonc.2023.1165405.
- Schmitz AC, Peters NHGM, Veldhuis WB, Gallardo AM, van Diest PJ, Stapper G, et al. Contrast-enhanced 3.0-T breast MRI for characterization of breast lesions: increased specificity by using vascular maps. Eur Radiol. 2008;18(3):355-364. doi: 10.1007/s00330-007-0766-z.
- D'Orsi CJ, Sickles EA, Mendelson EB, Morris EA. ACR BI-RADS® atlas: Breast Imaging Reporting and Data System. 5th ed. Reston, VA: American College of Radiology; 2013.
- Baltzer PÄT, Dietzel M, Kaiser WA. A simple and robust classification tree for differentiation between benign and malignant lesions in MRmammography. Eur Radiol. 2013;23(8):2051-2060. doi: 10.1007/s00330-013-2804-3.
- Baltzer PAT, Krug KB, Dietzel M. Evidence-based and structured diagnosis in breast MRI using the Kaiser Score. Rofo. 2022;194(11):1216-1228. English, German. doi:10.1055/a-1829-5985.

- Dietzel M, Baltzer PAT. How to use the Kaiser score as a clinical decision rule for diagnosis in multiparametric breast MRI: a pictorial essay. Insights Imaging. 2018;9(3):325-335. doi:10.1007/s13244-018-0611-8.
- Mohammadzadeh S, Mohebbi A, Moradi Z, Abdi A, Mohammadi A, Hakim PK, et al. Diagnostic performance of Kaiser score in the evaluation of breast cancer using MRI: a systematic review and meta-analysis. Eur J Radiol. 2025;186:112055. doi:10.1016/j.ejrad.2025.112055.
- Avdan-Aslan A, Gültekin S. Diagnostic performance of Kaiser score in patients with newly diagnosed breast cancer: factors associated with false-negative results. Eur J Radiol. 2023;164:110864. doi: 10.1016/j. eirad.2023.110864.
- Sachani P, Dhande R, Parihar P, Kasat PR, Bedi GN, Pradeep U, et al. Enhancing the understanding of breast vascularity through insights from dynamic contrast-enhanced magnetic resonance imaging: a comprehensive review. Cureus. 2024;16(9):e70226. doi:10.7759/cureus.70226.
- Baltzer PA, Dietzel M. Kaiser Score. University Hospital Freiburg of Germany, School of Radiology; 2023 (updated: 2021 Dec 6; cited 2025 February 5). Available from: https://school-of-radiology.com/kaiser-score/.
- Fischer DR, Malich A, Wurdinger S, Boettcher J, Dietzel M, Kaiser WA. The adjacent vessel on dynamic contrast-enhanced breast MRI. AJR Am J Roentgenol. 2006;187(2):W147-W151. doi: 10.2214/AJR.05.0377.
- Wolff AÖ, Hammond MEH, Allison KH, Harvey BE, Mangu PB, Bartlett JMS, et al. Human epidermal growth factor receptor 2 testing in breast cancer: ASCO-College of American Pathologists Guideline Update. J Clin Oncol. 2023;41(19):3867-3872. doi:10.1200/JCO.22.02864.
- World Health Organization, International Agency for Research on Cancer. WHO Classification of Breast Tumours: WHO Classification of Tumours, 5th Ed. Volume 2 [Internet]. Geneva: World Health Organization; 2019. Available from: https://publications.iarc.fr/581.
- Dietzel M, Baltzer PAT, Vag T, Herzog A, Gajda M, Camara O, et al. The adjacent vessel sign on breast MRI: new data and a subgroup analysis for 1,084 histologically verified cases. Korean J Radiol. 2010;11(2): 178-186. doi:10.3348/kjr.2010.11.2.178.
- Weidner N. Tumor angiogenesis: review of current applications in tumor prognostication. Semin Diagn Pathol. 1993;10(4):302-313.
- Çetinkaya E, Yıldız Ş, Otçu H, Sharifov R, Çelik Yabul F, Alkan A. The value of adjacent vessel sign in malignant breast tumors. Diagn Interv Radiol. 2022;28(5):463-469. doi:10.5152/dir.2022.211228.
- Bujor IS, Cioca A, Ceauşu RA, Veaceslav F, Nica C, Cîmpean AM, et al. Evaluation of vascular proliferation in molecular subtypes of breast cancer. In Vivo. 2018;32(1):79-83. doi:10.21873/invivo.11207.







BRIEF RESEARCH ARTICLE

Comparison of the diagnostic performance of Quantra artificial intelligence software with an experienced radiologist in the mammographic breast density assessment in women with and without breast implants

Beatriz E. Gonzalez-Ulloa*, Claudia B. Corona-Gonzalez, and Rosa L. Molina-Gutierrez

Breast Imaging Department, Centro de Diagnostico Especializado por Imagen, Zapopan, Jalisco, Mexico

ABSTRACT

Mammographic sensitivity decreases when mammographic breast density (MBD) is assessed in women with dense breasts and/or breast implants. This study compared the diagnostic performance of Quantra artificial intelligence (AI) software with an experienced radiologist with 32 years of experience interpreting breast images as the gold standard in MBD assessment of dense categories (c+d) in women with and without breast implants. In this prospective cohort study, an experienced radiologist and AI Quantra (v 2.2.2) assessed 2D mammograms and tomosyntheses of women over 35 years of age with and without breast implants in dense categories (c+d) based on the Breast Imaging Reporting and Data System (BI-RADS) 5th Edition. Sensitivity, specificity, positive predictive value, negative predictive value, and accuracy were recorded. AI Quantra sensitivity was low (30.6%, 95% CI 18.2-45.4) in dense categories (c+d) in women with breast implants (n = 130). In contrast, sensitivity was high (95.2%, 95% CI 92.1-97.3) in women without breast implants (n = 548). Accuracy was 73.1% (95% CI 64.6-80.5%) and 81.0% (95% CI 77.5-84.2), respectively. The diagnostic performance of the current version of Quantra AI in assessing MBD in dense categories (c+d) was unacceptably low in women with breast implants.

Keywords: Mammographic breast density. Artificial intelligence. Experienced radiologist. BI-RADS. Quantra.

INTRODUCTION

The diagnostic performance of artificial intelligence (AI) assessing mammographic breast density (MBD) is comparable to that of radiologists, and synergies may exist between the two¹⁻³. The Food and Drug Administration (FDA) approved AI Quantra v.2.2.2 for MBD assessment. It quantifies the densest area based on the Breast Imaging Reporting and Data System (BI-RADS) 5th Edition⁴. AI software for MBD assessment has potential benefits and risks, as radiologists may be distracted, leading to more errors in image diagnosis⁵⁻⁷. Therefore, an automated AI method such as Quantra software could

have greater reproducibility and accuracy in classifying MBD. However, Quantra AI was not developed for MBD assessment of women with breast implants⁸.

Intra- and interobserver agreement between radiologists and Quantra AI has been reported in women without implants^{3,5}, and when women with and without implants are compared⁹. In a previous report, we compared the diagnostic performance of AI Quantra and an experienced radiologist in MBD assessment without differentiating women with and without implants⁵.

Previous studies have shown better diagnostic performance of Quantra AI in two categories (non-dense and dense)^{10,11}. Mammographic sensitivity decreases in

*Corresponding author:

Beatriz E. Gonzalez-Ulloa E-mail: betyglez@yahoo.com Received for publication: 04-05-2025 Accepted for publication: 09-06-2025 DOI: 10.24875/JMEXFRI.M25000108 Available online: 10-10-2025 J Mex Fed Radiol Imaging. 2025;4(3):198-204 www.JMeXFRI.com

2696-8444 / © 2025 Federación Mexicana de Radiología e Imagen, A.C. Published by Permanyer. This is an open access article under the CC BY-NC-ND (https://creativecommons.org/licenses/by-nc-nd/4.0/).

women with dense breasts and implants^{12,13}. The dense (c+d) category has a higher risk of cancer, and additional examinations must be performed. This study compared the diagnostic performance of Quantra AI software with that of an experienced radiologist as the gold standard in MBD assessment of dense categories (c+d) in women with and without breast implants.

MATERIAL AND METHODS

This prospective cohort study was conducted from May 2 to June 30, 2022, in the Breast Imaging Department of the Centro de Diagnóstico Especializado por Imagen in Zapopan, Jalisco, Mexico. An experienced radiologist with training in breast imaging and current certification by the Mexican Council of Radiology and Imaging participated in the study. Consent was obtained from the radiologist who participated in the study.

Study development and variables

Screening or diagnostic mammograms of women aged 35 years and older with and without breast implants were analyzed from a previously published study⁹ corresponding to phase 1. The dense MBD category (c+d) was based on the American College of Radiology BI-RADS 5th Edition⁴. Sex and years of experience as a radiologist performing breast imaging examinations were recorded.

Digital mammography and digital breast tomosynthesis

Images were acquired using Selenia Dimensions equipment (Hologic, Bedford, MA, USA) with automatic acquisition parameters. Images were stored and reviewed in PACS (SecureView, Diagnostic Workstation, Bedford, MA, USA). Conventional projections, two craniocaudal (CC) and two mediolateral oblique (MLO) images of both breasts, were obtained. Images with implant displacements were evaluated in women with breast implants. MBD was classified according to the 5th Edition of BI-RADS based on the densest area of fibroglandular tissue in the dense breast (c+d), category c, heterogeneously dense, and category d, extremely dense.

Quantra Al software

The mammography images were analyzed with Quantra AI version 2.2.2 (Hologic Inc., Bedford, MA, USA). AI Quantra analyzes MBD in images with implant displacements. The assessment is based on the

Table 1. Diagnostic performance of Al Quantra compared to an experienced radiologist as the gold standard in MBD assessment of dense categories^a in women with breast implants

Parameter	%	95% CI
Sensitivity	30.6	18.2-45.4
Specificity	98.8	93.3-99.9
Positive predictive value	93.7	67.1-99.1
Negative predictive value	70.2	66.1-73.9
Accuracy	73.1	64.6-80.5

ac+d categories; Al: artificial intelligence; BI-RADS: Breast Imaging Reporting and Data System; MBD: mammographic breast density; CI: confidence interval.

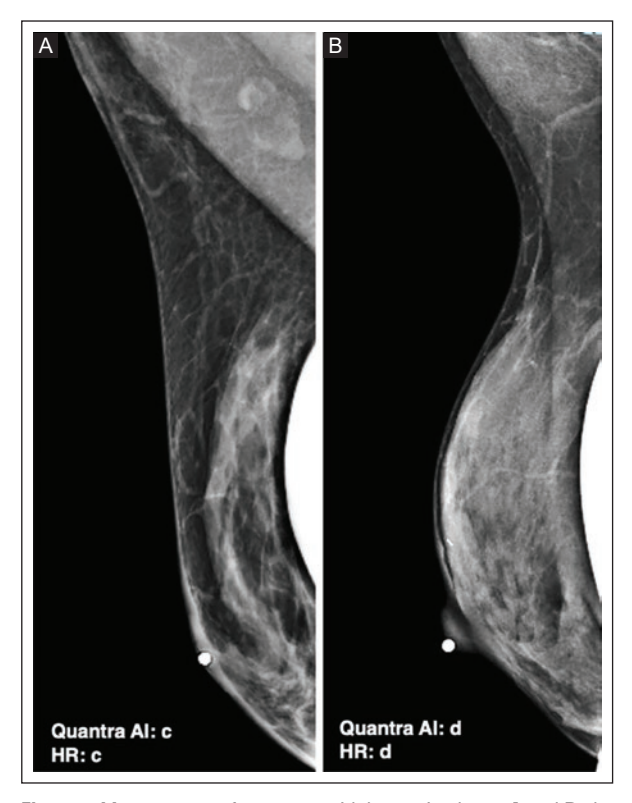


Figure 1. Mammogram of a woman with breast implants. A and B: the MLOID views of the right breast show concordance between Quantra AI and an experienced radiologist (HR) in the classification of dense (c+d) MBD categories using BI-RADS 5th Edition: category c, heterogeneously dense; and category d, extremely dense.

Al: artificial intelligence; BI-RADS: Breast Imaging Reporting and Data System; MBD: mammography breast density; HR: human reader; MLOID: mediolateral oblique implant displacement.

distribution and texture of the fibroglandular tissue pattern, with an estimate of breast composition by selecting the densest category according to BI-RADS 5th Edition.

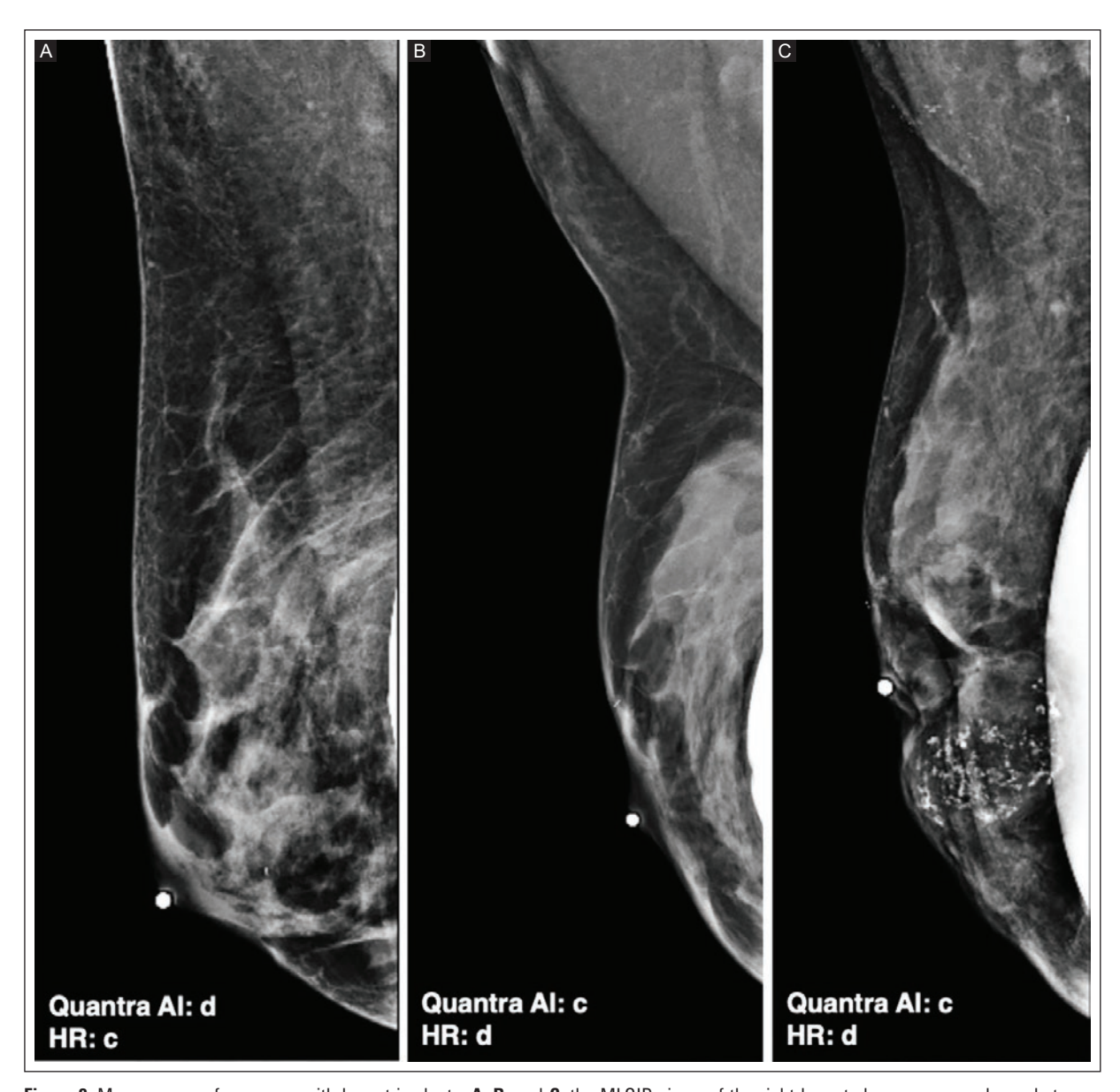


Figure 2. Mammogram of a woman with breast implants. A, B, and C: the MLOID views of the right breast show no concordance between Quantra AI and an experienced radiologist (HR) in the classification of dense (c+d) MBD categories using BI-RADS 5th Edition: category c, heterogeneously dense; and category d, extremely dense.

Al: artificial intelligence; BI-RADS: Breast Imaging Reporting and Data System; HR: human reader; MBD: mammography breast density; MLOID: mediolateral oblique implant displacement.

Statistical analysis

Sensitivity, specificity, positive predictive values, negative predictive values, and accuracy were calculated to evaluate the diagnostic performance of Quantra Al compared to an experienced radiologist as the gold standard. The statistical analysis was performed with SPSS v.25 (IBM Corp., Armonk, NY, USA).

RESULTS

The radiologist with 32 years of experience reads approximately 90 mammograms per week and spends 50 hours performing various breast examinations and procedures (including mammography, ultrasound, MRI, biopsies, and breast marking). A total of 678 mammograms were analyzed, 130 mammograms with breast

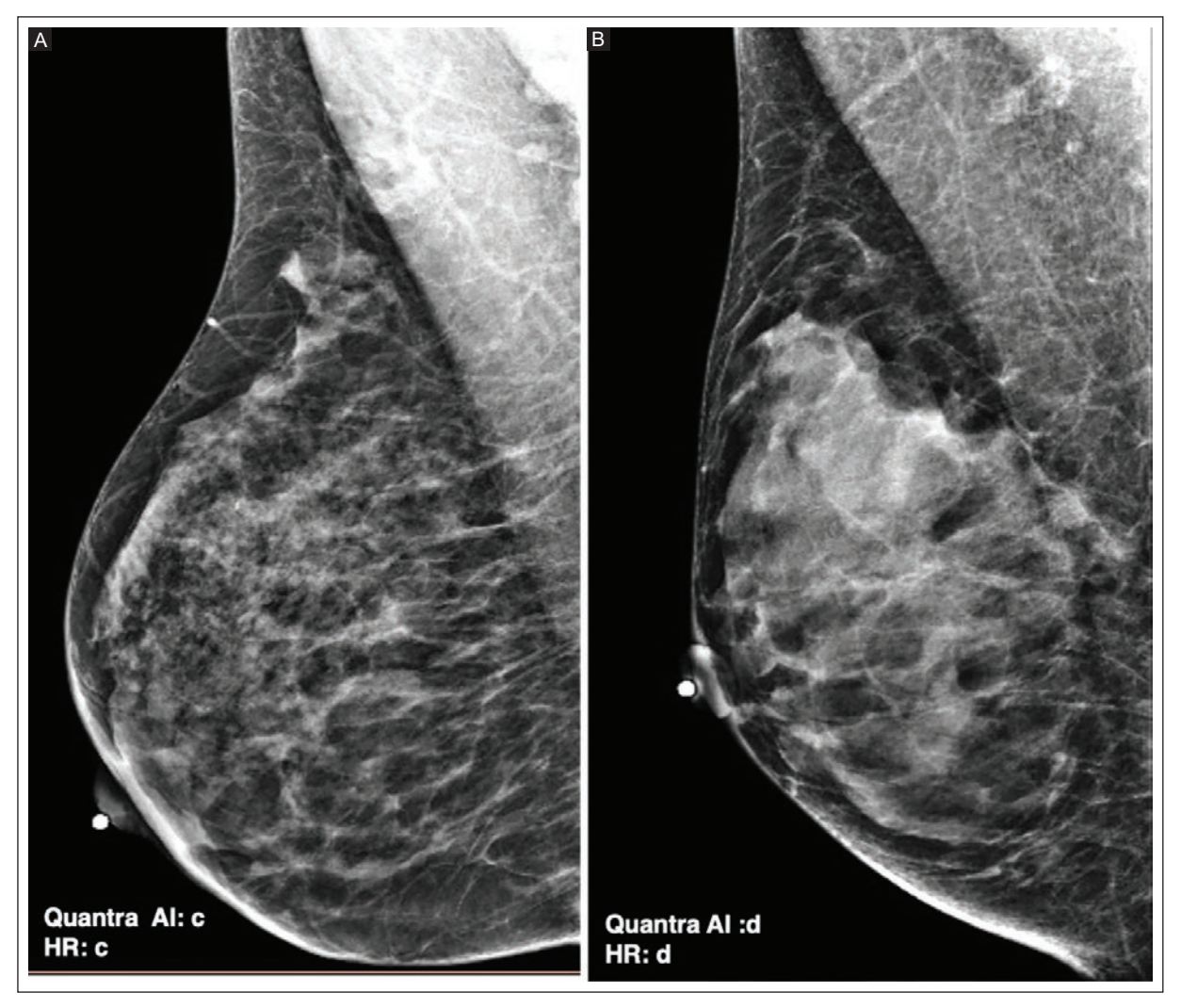


Figure 3. Mammogram of a woman without breast implants. A and B: the MLO views of the right breast show concordance between Quantra AI and an experienced radiologist (HR) in the classification of dense (c+d) MBD categories using BI-RADS 5th Edition: category c, heterogeneously dense; and category d, extremely dense.

Al: artificial intelligence; BI-RADS: Breast Imaging Reporting and Data System; MBD: mammography breast density; HR: human reader; MLO: mediolateral oblique.

Table 2. Diagnostic performance of Al Quantra compared to an experienced radiologist as the gold standard in MBD assessment of dense categories^a in women without breast implants

Parameter	%	95% CI
Sensitivity	95.2	92.1-97.3
Specificity	62.6	56.1-68.8
Positive predictive value	76.8	73.7-79.6
Negative predictive value	90.8	85.7-94.3
Accuracy	81.0	77.5-84.2

[°]c+d categories; Al: artificial intelligence; BI-RADS: Breast Imaging Reporting and Data System; MBD: mammographic breast density; CI: confidence interval.

implants and 548 mammograms without breast implants.

Table 1 shows the diagnostic performance of Al Quantra compared to an experienced radiologist in assessing MBD in women with dense breasts (c+d) and breast implants. The sensitivity of Al Quantra in assessing dense categories (c+d) in women with breast implants (n = 130) was low (30.6%, 95% CI 18.2-45.4). Specificity was high (98.8%, 95% CI, 93.3-99.9) while accuracy was 73.1% (95% CI, 64.6-80.5).

Figure 1 shows a mammogram with concordance between Quantra AI and the radiologist in classifying dense (c+d) MBD categories in a woman with breast

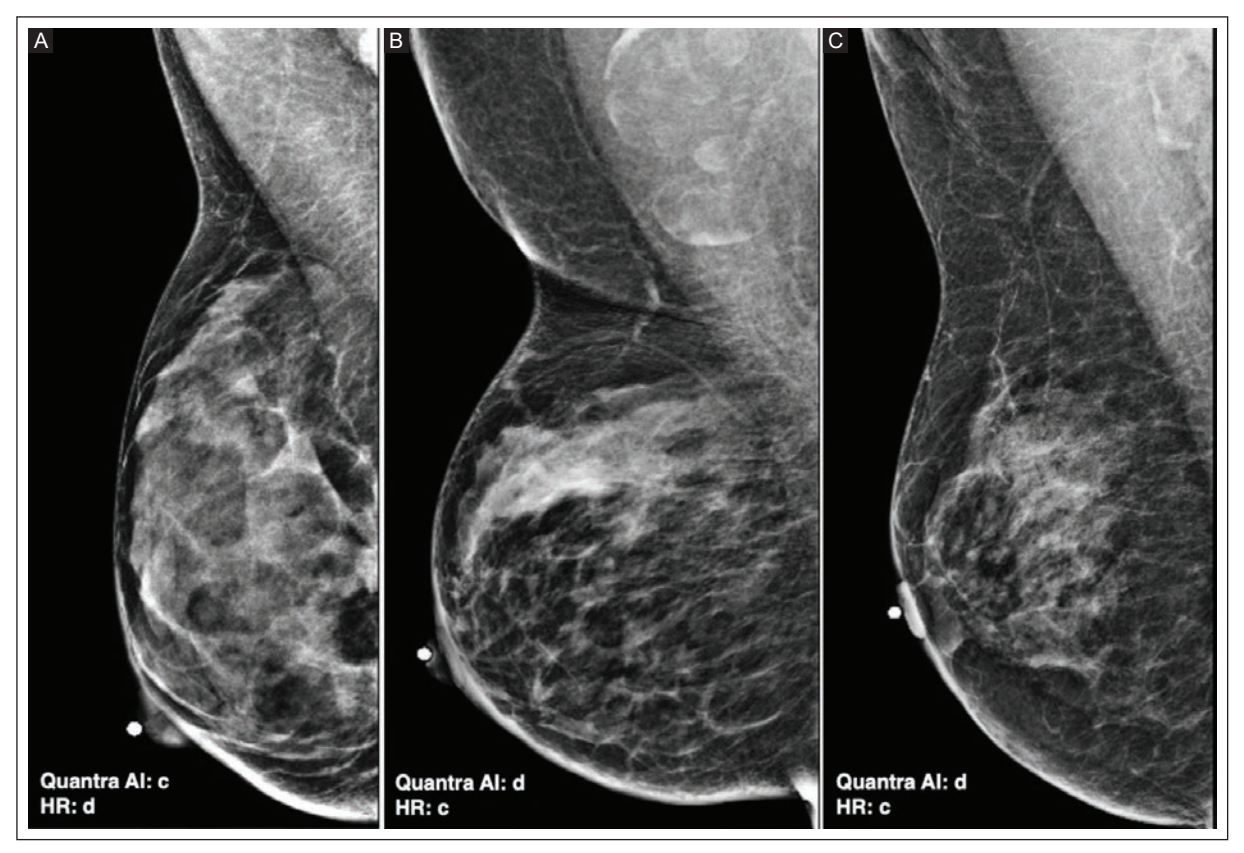


Figure 4. Mammogram of a woman without breast implants. A, B, and C: the MLO views of the right breast show no concordance between Quantra AI and an experienced radiologist (HR) in the classification of dense (c+d) MBD categories using BI-RADS 5th Edition: category c, heterogeneously dense; and category d, extremely dense.

Al: artificial intelligence; BI-RADS: Breast Imaging Reporting and Data System; HR: human reader; MBD: mammography breast density; MLO: mediolateral oblique.

implants. In contrast, figure 2 shows that Quantra Al underestimates or overestimates dense MBD categories compared to the radiologist in a patient with breast implants.

Table 2 shows the diagnostic performance of Quantra Al compared to an experienced radiologist as the gold standard in MBD assessment of dense categories (c+d) in women with dense breasts without breast implants. Sensitivity was high (95.2%, 95% CI 92.1-97.3), while specificity was low (62.6%, 95% CI 56.1-68.8). Accuracy was 81.0% (95% CI, 77.5-84.2).

Figure 3 shows the mammogram of a woman without breast implants, with concordance between Quantra AI and the radiologist in classifying the dense (c+d) MBD categories. In contrast, Figure 4 shows that the Quantra AI underestimates or overestimates the dense MBD categories compared to the radiologist in a patient without breast implants.

DISCUSSION

Our study showed unacceptably low sensitivity in the diagnostic performance of the current version of Quantra AI in MBD assessment in dense categories (c+d) in women with breast implants. In contrast, its sensitivity in assessing dense MBD categories (c+d) in women without breast implants was high. This report is the first comparing Quantra AI and an experienced radiologist in MBD assessment of women with dense breasts with and without breast implants.

Quantra AI has not been sufficiently tested for the evaluation of MBD in women with implants, and there are no reports evaluating its diagnostic performance. In our previously published study⁹, we examined 678 women, 130 with breast implants and 548 without breast implants. Quantra AI classified dense categories in 114 (87.7%) of 130 women with breast implants and four

radiologists in 81 (62.3%), whereas in women without breast implants. Quantra Al classified dense categories in 384 (70.1%) of 548 and radiologists in 310 (56.6%) of 548 mammograms; the concordance between Quantra Al and four radiologists was better in women without breast implants. On the other hand, the interobserver agreement between four radiologists and Quantra AI in dense categories was slight to fair in women with breast implants. In contrast, it was moderate in women without breast implants. These results suggest that the interobserver agreement between the radiologists and Quantra Al was unacceptable in dense MBD categories in women with breast implants. This study showed comparable results in the diagnostic performance of Quantra Al with that of an experienced radiologist as the gold standard in MBD assessment of dense categories (c+d) in women with breast implants. The sensitivity of Quantra Al was unacceptably low (30.6%). This result means that Quantra AI does not detect dense breasts in 7 out of 10 women with breast implants. We therefore confirmed the manufacturer's recommendation that Quantra Al can process images with breast implants, although it was not designed for this purpose and may inaccurately report MBD in women with breast implants.

There are few reports on the diagnostic performance of Al Quantra in MBD assessment^{1,10,11}. Epko et al.¹¹ compared the previous version of Al Quantra (v2.0) with a majority radiologist-generated report as the gold standard for MBD assessment. Sensitivity was 91.3% and specificity was 83.6% for the two MBD categories (a+b) vs. c+d). Although the authors did not specify whether the women had implants or not, the diagnostic performance of Al Quantra was high, especially in the two MBD categories. They concluded that the diagnostic performance of Al Quantra reproduced the BI-RADS classification for two MBD categories very well. In our study, using the current Al Quantra version (v2.2.2) as a comparison to an experienced radiologist, we found high sensitivity (95.2%) for dense breasts in women without breast implants, with a specificity of 62.6%. As Quantra Al version was a different version, it showed a higher sensitivity with the new version of the software. There is no doubt about the added value that AI can bring to diagnostic imaging, especially in the assessment of MBD.

The strengths of this study are its prospective design and sample size. However, the limitations of the study were that it was a single-center study, only one experienced radiologist participated, and a single mammography unit recorded all mammograms. On the other hand, Quantra AI was the only software evaluated at our center.

CONCLUSION

The diagnostic performance of the current version of Quantra AI in MBD assessment in dense categories (c+d) had unacceptably low sensitivity in our study of women with breast implants. In contrast, the sensitivity of Quantra AI in assessing dense MBD categories (c+d) in women without breast implants was high. Therefore, it is important to have an AI tool with better diagnostic performance in women with breast implants. We hope a new version of Quantra AI software will be available for use in women with implants, as the number of women with implants is increasing.

Acknowledgments

The authors thank Professor Ana M. Contreras-Navarro for her guidance in preparing and writing this scientific paper.

Funding

This research received no external funding.

Conflicts of interest

The authors declare no conflicts of interest.

Ethical considerations

Protection of humans and animals. The authors declare that the procedures followed complied with the ethical standards of the responsible human experimentation committee and adhered to the World Medical Association and the Declaration of Helsinki. The procedures were approved by the institutional Ethics Committee.

Confidentiality, informed consent, and ethical approval. Consent was obtained from the radiologist who participated in the study.

Declaration on the use of artificial intelligence. The authors declare that no generative artificial intelligence was used in the writing of this manuscript.

REFERENCES

- Richard-Davis G, Whittemore B, Disher A, Rice VM, Lenin RB, Dollins C, et al. Evaluation of quantra hologic volumetric computerized breast density software in comparison with manual interpretation in a diverse population. Breast Cancer (Auckl). 2018;12:1178223418759296.
- Taylor CR, Monga N, Johnson C, Hawley JR, Patel M. artificial intelligence applications in breast imaging: current status and future directions. Diagnostics (Basel). 2023;13(12):2041. doi:10.3390/diagnostics13122041.

- Ciatto S, Bernardi D, Calabrese M, Durando M, Gentilini MA, Mariscotti G, et al. A first evaluation of breast radiological density assessment by QUANTRA software as compared to visual classification. Breast. 2012;21(4):503-506. doi:10.1016/j.breast.2012.01.005.
- American College of Radiology. ACR BI-RADS Atlas: Breast Imaging Reporting and Data System. 5th ed. Reston, VA: American College of Radiology; 2013.
- Gonzalez-Ulloa B, Corona-Gonzalez C, Molina-Gutierrez R. Diagnostic performance of an experienced radiologist and Quantra artificial intelligence software in the assessment of mammographic breast density. J Mex Fed Radiol Imaging. 2025;4(1):37-43. doi:10.24875/JMEXFRI.M25000094.
- Ornelas-Cortinas G, Luna-Marroquin AK. Diagnostic errors in radiology: where are we? J Mex Fed Radiol Imaging. 2024;3(4):205-207. doi: 10.24875/JMEXFRI.M24000085.
- Dratsch T, Chen X, Rezazade Mehrizi M, Kloeckner R, M\u00e4hringer-Kunz A, P\u00fcsken M, et al. Automation bias in mammography: the impact of artificial intelligence BI-RADS suggestions on reader performance. Radiology. 2023;307(4):e222176. doi:10.1148/radiol.222176.
- Hologic Inc. Understanding Quantra 2.2 user guide for Cenova 3.0.1.
 English Man 05503-302 rev 002. Bedford, MA: Hologic Inc.; 2019 [Internet]. Available from: https://www.hologic.com.

- Gonzalez-Ulloa B, Corona-Gonzalez C, Molina-Gutierrez R. Comparison of mammography breast density assessment by radiologists and Quantra artificial intelligence in women with and without breast implants: intra and interobserver agreement. J Mex Fed Radiol Imaging. 2025;4(2):102-111. doi:10.24875/JMEXFRI.M25000103.
- Gonzalez-Ulloa B, Corona-Gonzalez C, Molina-Gutierrez R. Mammography breast density assessment with Quantra artificial intelligence software: intra and interobserver agreement with radiologists. J Mex Fed Radiol Imaging. 2024;3(4):221-230. doi:10.24875/JMEXFRI.M24000088.
- Ekpo EU, McEntee MF, Rickard M, Brennan PC, Kunduri J, Demchig D, et al. Quantra[™] should be considered a tool for two-grade scale mammographic breast density classification. Br J Radiol. 2016;89(1060): 20151057. doi:10.1259/bjr.20151057.
- Miglioretti DL, Rutter CM, Geller BM, Cutter G, Barlow WE, Rosenberg R, et al. Effect of breast augmentation on the accuracy of mammography and cancer characteristics. JAMA. 2004;291(4):442-450. doi:10.1001/ jama.291.4.442.
- Handel N. The effect of silicone implants on the diagnosis, prognosis, and treatment of breast cancer. Plast Reconstr Surg. 2007;120(7 Suppl 1): 81S-93S. doi:10.1097/01.prs.0000286578.94102.2b.





CASE REPORT

Quantification of an intrathoracic organoaxial gastric volvulus secondary to a hiatal hernia diagnosed by multidetector computed tomography: a case report

Felipe de J. Avila-Zamarripa¹*, Roberto Hernandez-Juarez², Maribel Rios-Vazquez¹, Jesus M. de la Fuente-Salazar¹ and Edgar I. Perez-Rodriguez¹

¹Department of Radiology and Imaging, Hospital Regional de Alta Especialidad de Ciudad Victoria, Ciudad Victoria, Tamaulipas; ²Department of Radiology and Imaging, Hospital Angeles Pedregal, Mexico City. Mexico

ABSTRACT

Contrast-enhanced multidetector computed tomography (MDCT) with multiplanar reformations is useful for diagnosing an intrathoracic organoaxial gastric volvulus secondary to a hiatal hernia. We describe the case of a 60-year-old man with morbid obesity admitted to the emergency room with severe epigastric pain, nausea, vomiting, and dyspnea. Contrast-enhanced thoracoabdominal MDCT showed a large type IV hiatal hernia with complete intrathoracic migration of the stomach and the adjacent mesentery. The gastroesophageal junction was posterior and inferior to the gastric fundus, corresponding to organoaxial gastric torsion with no tomographic findings of ischemia or perforation. The intrathoracic hernia sac volume was measured by manually outlining the hernia sac. The hiatal defect area measured 46 cm². The intrathoracic hernia sac volume was 2075 cc. Immediate insertion of a nasogastric tube facilitated decompression, and the gastric volvulus resolved completely. A surgical procedure was subsequently performed to repair the hiatal hernia. This case report is for educational purposes to demonstrate the usefulness of contrast-enhanced MDTC with multiplanar reformations to quantify a hiatal defect area and intrathoracic hernia sac volume in an intrathoracic organoaxial gastric volvulus secondary to a type IV hiatal hernia. This quantitative approach provides diagnostic value beyond traditional subjective assessment.

Keywords: Hiatal hernia. Gastric volvulus. Multidetector computed tomography. Thoracic hernia. Case Report.

INTRODUCTION

An intrathoracic gastric volvulus is a rare entity associated with a type IV paraesophageal hiatal hernia. The organoaxial form is the most common and occurs in 60% of cases of gastric volvulus. It is characterized by rotation of the stomach along its longitudinal axis, connecting the cardia to the pylorus. The stomach and other abdominal

viscera migrate into the mediastinum, favoring gastric torsion¹⁻⁴. Approximately 4% of hiatal hernias are complicated by a gastric volvulus^{1,5,6}. It is more common in adults in their fifth decade of life and is associated with large hiatal hernia. An association with gender or ethnicity has not been proven^{1,7}. Serious complications include ischemia, gastric necrosis, perforation, and sepsis, especially if not diagnosed and treated promptly^{1,4,7}.

Contrast-enhanced multidetector computed tomography (MDCT) with multiplanar reformations is useful for diagnosing intrathoracic organoaxial gastric volvulus secondary to hiatal hernia, allowing the identification of the axis of rotation, the extent of intrathoracic displacement, and indirect findings of complications such as ischemia or perforation^{6,8}. In contrast to conventional methods, such as X-ray or fluoroscopy, computerized volumetric analysis and multidimensional visualization allow quantification of the hiatal defect area and intrathoracic hernia sac volume, which have been advocated for measurement with tailored repairs based on defect size9-11. This case report demonstrates the guantification of a hiatal defect area and intrathoracic hernia sac volume on contrast-enhanced MDCT in a 60-yearold man with an intrathoracic organoaxial gastric volvulus secondary to a hiatal hernia.

CLINICAL CASE DESCRIPTION

A 60-year-old man with morbid obesity, systemic arterial hypertension, and T2 diabetes came to the emergency room because of severe epigastric pain that had been developing over 36 hours, with nausea, persistent belching, non-bilious vomiting, bloating, dyspnea, and retrosternal pain with no history of abdominal surgery. Physical examination revealed a blood pressure of 150/95 mmHg, a heart rate of 98 beats per minute, a respiratory rate of 20 breaths per minute, a body temperature of 36.8°C, and an oxygen saturation of 96% on room air. Body weight was 130 kg, with a height of 1.72 m, and a body mass index (BMI) of 44 kg/m². No pathological findings were found on lung auscultation. Abdominal examination revealed severe tenderness in the epigastric region, with no involuntary muscle guarding.

Image findings

A 1.5-mm contrast-enhanced thoracoabdominal MDCT was performed using a Somatom Sensation AS 40[™] (Siemens Healthineers, Erlangen, Germany) with oral positive and neutral contrast medium. Figure 1 shows illustrations of the normal position of the stomach and two anatomical types of gastric volvulus.

Figure 2 shows a contrast-enhanced thoracoabdominal MDCT examination of the patient with a large type IV hiatal hernia with complete intrathoracic migration of the stomach and the adjacent mesentery. The stomach is distended, and contents are mixed with air (blue

arrowhead) and fluid. The gastroesophageal junction is posterior and inferior to the gastric fundus, which corresponds to organoaxial gastric torsion without tomographic findings of ischemia or perforation.

The intrathoracic hernia sac volume was measured by manually outlining the hernia sac on all axial images containing the hernia, which measured 18.7 cm in length, 15.6 cm in width, and 13.6 cm in height (Figure 3). The hiatal defect area measured 46 cm². The volume was calculated with the classical ellipsoidal formula (V = $\pi/6$ × L × W × H) based on orthogonal measurements. The intrathoracic hernia sac volume was 2075 cc.

Clinical outcome

Immediate insertion of a nasogastric tube allowed decompression and resulted in complete resolution of the gastric volvulus. At follow-up, a surgery was performed to repair the hiatal hernia.

DISCUSSION

This case report demonstrates the usefulness of contrast-enhanced MDTC with multiplanar reformations to quantify a hiatal defect area and intrathoracic hernia sac volume in a case of intrathoracic organoaxial gastric volvulus secondary to type IV hiatal hernia. MDCT with multiplanar reformation accurately identifies the point of torsion for early diagnosis and assesses gastric viability.

Contrast-enhanced MDCT examination is uniquely suited for visualizing the diaphragm and provides important information about the three-dimensional contents of the hiatal hernia. These include crural dimensions, the size of the hernia sac, the intrathoracic hernia sac volume, and the relationship with neighboring structures, as well as the presence of complications such as gastric volvulus9. Rengo et al.12 reported excellent overall reproducibility of hernia sac size measurement (ICC 0.95; 95% CI 0.90 to 0.98) by MDCT, independently of the reader's experience, with good-to-excellent intraand interreader agreement. In our case, contrastenhanced MDCT showed rotation of the stomach on its longitudinal axis and complete migration into the mediastinum, with no evidence of ischemia or perforation. Kao et al.9 evaluated 213 patients with a diagnosis of paraesophageal hernia who underwent preoperative contrast-enhanced MDCT with volumetric analysis software (Aguarius iNtuition, TeraRecon, San Mateo, CA, USA) to quantify the hiatal defect area and intrathoracic

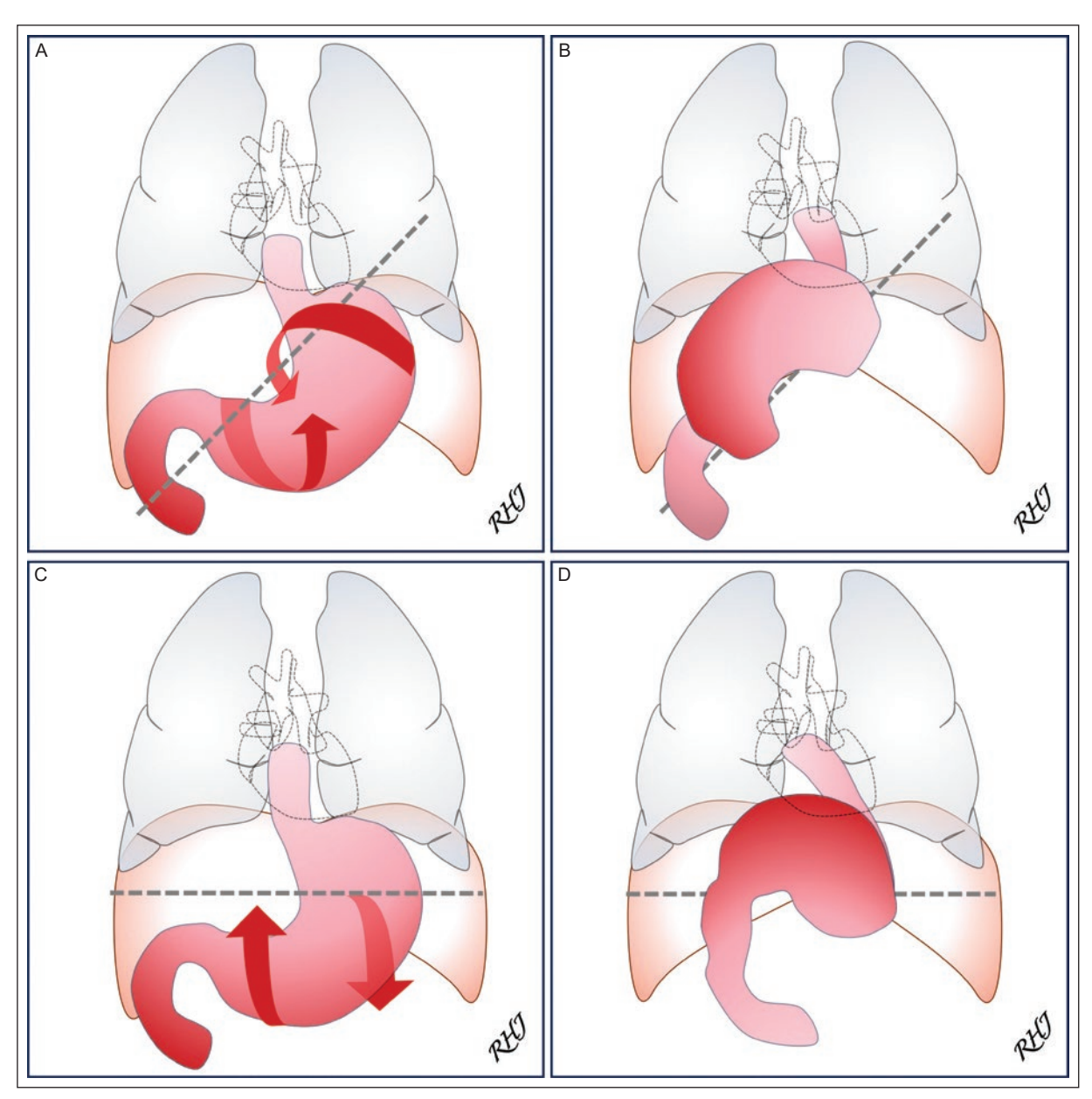


Figure 1. Illustrations of the normal position of the stomach and the two anatomical types of gastric volvulus. A: the normal anatomical position of the stomach in relation to the diaphragm shows the longitudinal axis extending from the gastroesophageal junction to the pylorus (dashed line) and the course of the gastric fundus forming the characteristic inversion of the greater and lesser curvatures (red curved arrows).

B: in an organoaxial gastric volvulus, the stomach shows an abnormal rotation greater than 180° around its longitudinal axis (dashed line), resulting in complete inversion of the gastric anatomy. The fundus is inverted and displaced downwards, while the antrum is displaced upwards, causing inversion of the major and minor curvatures. C: the normal anatomical arrangement of the stomach in relation to the diaphragm, showing the transverse mesenteric axis connecting the lesser curvature to the greater curvature (dashed line), and the usual direction of the pylorus and gastric antrum when they are displaced anteriorly and upward. D: in a mesenteroaxial gastric volvulus, the stomach rotates around a transverse axis connecting the greater and lesser curvatures (dashed line). The antrum of the stomach shifts anteriorly and superiorly, and positions itself over the fundus, which remains in a posterior and inferior position.

hernia sac volume. The mean hiatal defect area was 25.7 cm², and the mean hernia sac volume was 365 cc. Elhage et al.¹³ reported higher values in a study of 201 patients undergoing emergency surgery, with a mean

hiatal defect area of 41.7 ± 19 . cm² and a mean intrathoracic hernia sac volume of 805 ± 483.5 cc. The hiatal defect area of 46 cm² in our case was comparable to the values reported by Elhage et al.¹³; however,

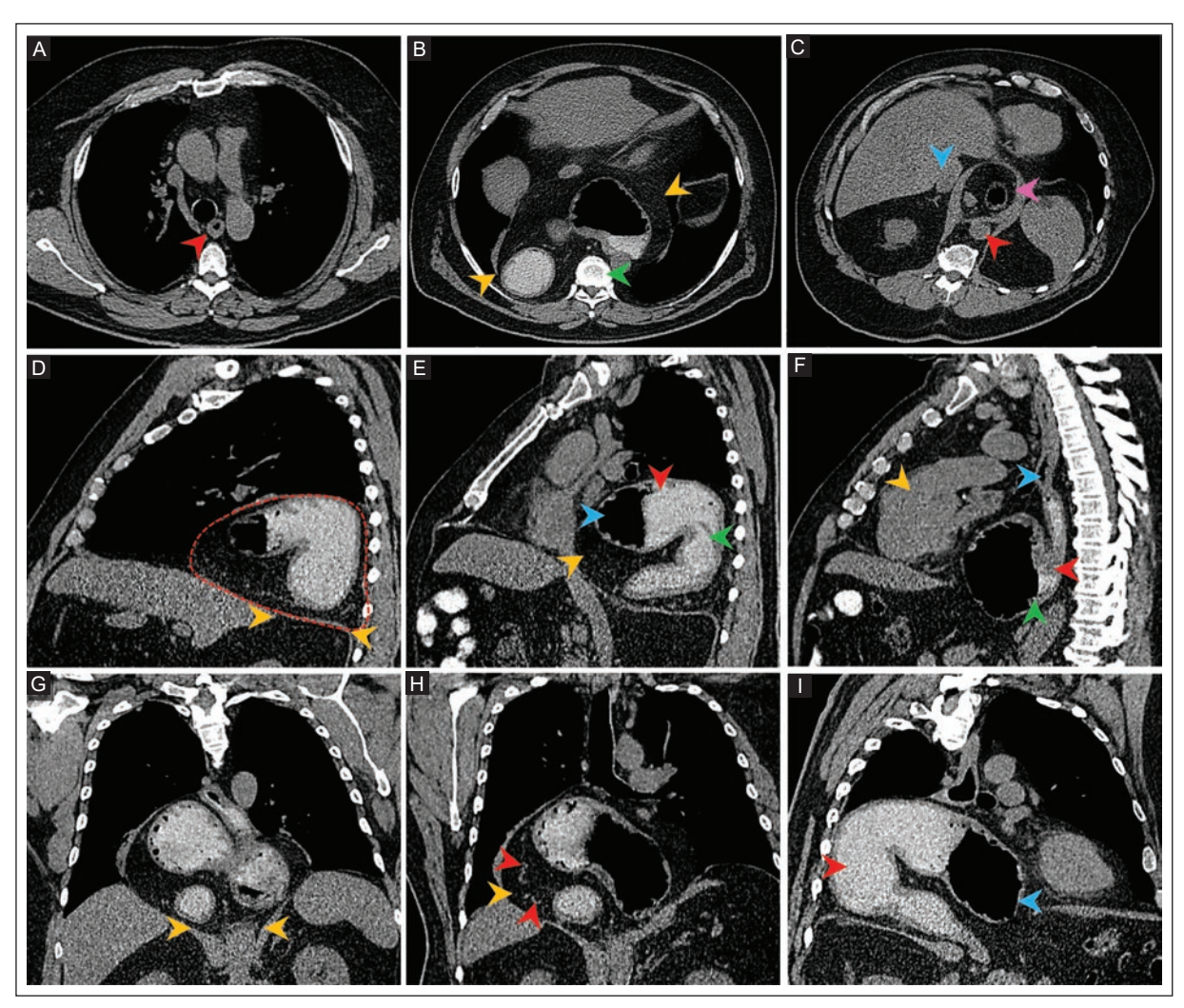


Figure 2. Contrast-enhanced thoracoabdominal MDCT examination in a 60-year-old man with severe epigastric pain. Axial oblique views in the upper panel, **A**: thickening of the posterior wall of the mid-thoracic esophagus, up to 9 mm (red arrowhead). **B**: at the level of the ninth thoracic vertebra (green arrowhead), a hernia sac containing stomach and mesentery is shown (yellow arrowheads). **C**: depiction of the three diaphragmatic hiatuses: aortic hiatus (red arrowhead), inferior vena cava hiatus (blue arrowhead), and a clearly dilated esophageal hiatus (pink arrowhead). Oblique sagittal views in the middle panel, **D**: large hiatal hernia (dashed line) with marked enlargement of the esophageal hiatus (yellow arrowheads). **E**: complete intrathoracic herniation of the stomach (red arrowhead) and the adjacent mesentery (yellow arrowhead). The stomach is distended, and the contents are mixed with air (blue arrowhead) and fluid (green arrowhead). **F**: the gastroesophageal junction (red arrowhead) is posterior and inferior to the gastric fundus, which corresponds to gastric torsion (green arrowhead). A shortening of the esophagus (blue arrowhead) and a slight upward displacement of the heart and anterior mediastinal structures is seen (yellow arrowhead). Oblique coronal views in the lower panel, **G**: loss of the normal diaphragmatic contour in the posterosuperior region (yellow arrowheads). **H**: herniated mesenteric structures with fat (yellow arrowhead) and mesenteric vessels in the mediastinum (red arrowheads). **I**: inversion of normal gastric anatomy: the antrum is superior (red arrowhead) and the fundus inferior (blue arrowhead), indicating organoaxial gastric torsion.

MDCT: multidetector computed tomography.

the intrathoracic hernia sac volume of 2075 cc was very high. This finding may have been related to the patient's high BMI and morbid obesity. On the other hand, we performed the measurements manually, which may result in lower precision compared to automated software. In our case, MDCT examination with multiplanar reformations allowed non-invasive quantification of the hiatal defect area and intrathoracic hernia sac volume.

Patients with a larger hernia sac volume are more likely to require urgent surgery¹³. However, some patients with intrathoracic organoaxial gastric volvulus secondary to hiatal hernia do well with watchful waiting because those who undergo immediate repair have a higher risk of an adverse outcome¹³. Elhage et al.¹³ found that emergency hiatal hernia repair is associated with increased morbidity and mortality. The author reported that patients

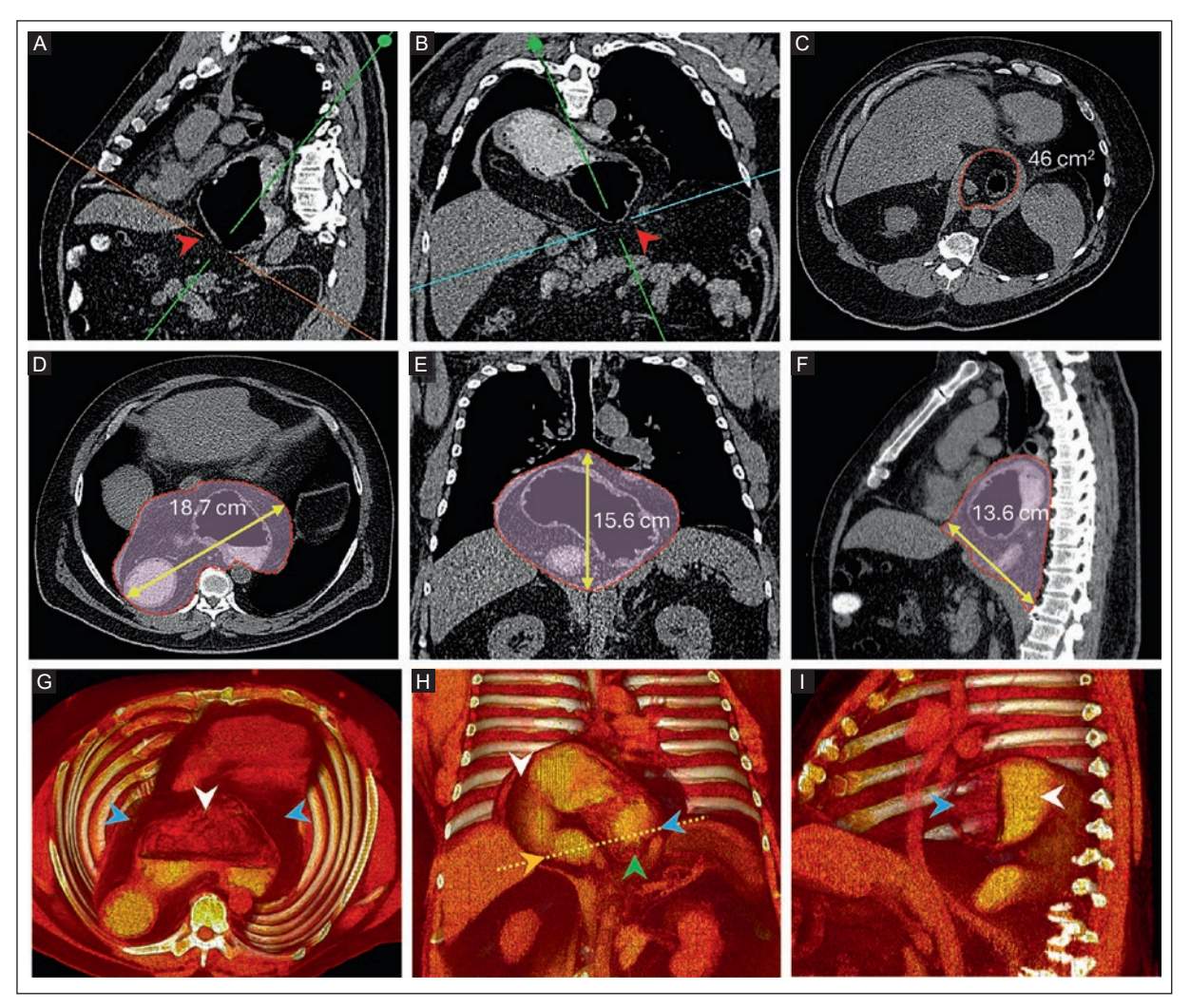


Figure 3. Contrast-enhanced thoracoabdominal MDCT examination in a 60-year-old man with severe epigastric pain. Upper panel, A: oblique sagittal view with an orange line indicating the oblique axial plane used to measure the anterior and posterior margins of the esophageal hiatus (red arrowhead) and a green line indicating the oblique sagittal plane. B: oblique coronal view with a blue line showing the oblique axial plane intersecting the lateral margins of the esophageal hiatus (red arrowhead) and a green line in the oblique coronal plane. C: double-oblique axial showing the cross-sectional area of the esophageal hiatus of 46 cm² (red dashed line). Middle panel, D: axial view showing the maximum transverse diameter of the hernia sac (18.7 cm) (yellow line arrows). E: coronal view at the level of the maximum cranio-caudal diameter (15.6 cm) (yellow line arrows). F: sagittal MDCT showing the maximum anteroposterior diameter (13.6 cm) (yellow line arrows). The estimated intrathoracic hernia sac volume was 2,074 cc. 3D volume-rendered images in the lower panel, G: complete intrathoracic herniation of the stomach (white arrowhead) and adjacent mesentery (blue arrowheads). H: stomach rotated around its longitudinal axis between the cardia (blue arrowhead) and pylorus (yellow arrowhead) with reversal of the anatomy: The fundus is inferior (green arrowhead) and the antrum superior (white arrowhead). I: distended stomach with mixed air (blue arrowhead) and fluid content (white arrowhead).

MDCT: multidetector computed tomography; 3D: three-dimensional; cm: centimeters; cm²: square centimeters, cc: cubic centimeters.

who underwent emergency surgery had a lower BMI $(25.5 \pm 5.5 \text{ kg/m}^2)$ than those who underwent elective surgery $(29.4 \pm 5.0 \text{ kg/m}^2)$, p < 0.001). In our patient, conservative treatment was sufficient to resolve the gastric volvulus. The absence of clinical and imaging findings indicating complications such as ischemia or perforation on contrast-enhanced MDCT allowed initial conservative management and subsequent surgical planning.

CONCLUSION

This case report demonstrates that contrast-enhanced MDCT with multiplanar reformations and three-dimensional volumetric analysis enables the quantification of the esophageal hiatal defect area and hernia volume, as well as an anatomically detailed assessment of intrathoracic organoaxial gastric volvulus secondary to hiatal hernia. Not all patients with hiatal hernia undergo

preoperative MDCT, and there is no consensus on whether this examination should be added to the routine work-up⁹. Further studies are needed to assess whether CT imaging should be used as a standard imaging examination in the evaluation of a particular subset of patients with hiatal hernia⁹.

Acknowledgments

The authors thank Dr. Jesús A. Campos-Benavides for his support in completing the clinical data. The authors thank Professor Ana M. Contreras-Navarro for her guidance in preparing and writing this scientific paper.

Funding

This research received no external funding.

Conflicts of interest

The authors declare no conflicts of interest.

Ethical considerations

Protection of humans and animals. The authors declare that the procedures outlined in this case report were conducted in agreement with the Declaration of Helsinki (1964) and its amendments.

Confidentiality, informed consent, and ethical approval. The authors followed the protocols of their work center on the publication of patient data.

Declaration on the use of artificial intelligence. The authors declare that no generative artificial intelligence was used in the writing of this manuscript.

REFERENCES

- Bauman ZM, Evans CH. Volvulus. Surg Clin North Am. 2018;98(5): 973-993. doi: 10.1016/j.suc.2018.06.005.
- Sanekommu H, Siddiqui Z, Farrell A, Taj S, Saleh AB, Alsaadi E, et al. Gastric outlet obstruction caused by acute gastric volvulus: a rare complication of hiatal hernia. Cureus. 2023;15(5):e38609. doi: 10.7759/cureus. 38609.
- Urbina-Velázquez MA, González-Flores JE, Portales-Rivera CM, Cruz-Méndez M, Sandoval A, Silva-Cruz FM, et al. Gastric volvulus as a complication of giant hiatal hernia: a case report and literature review. Cureus. 2025;17(5):e84257. doi: 10.7759/cureus.84257.
- Chau B, Dufel S. Gastric volvulus. Emerg Med J. 2007;24(6):446-447. doi:10.1136/emj.2006.041947.
- Fuchs KH, Kafetzis I, Hann A, Meining A. Hiatal hernias revisited: a systematic review of definitions, classifications, and applications. Life (Basel). 2024;14(9):1145. doi: 10.3390/life14091145
- Kaoukabi AE, Menfaa M, Hasbi S, Sakit F, Choho A. Acute gastric volvulus on hiatal hernia. Case Rep Surg. 2020(2):1-5. doi: 10.1155/2020/4141729.
- Rashid F, Thangarajah T, Mulvey D, Larvin M, Iftikhar SY. A review article on gastric volvulus: a challenge to diagnosis and management. Int J Surg. 2010;8(1):18-24. doi: 10.1016/j.ijsu.2009.11.002.
- Verde F, Hawasli H, Johnson PT, Fishman EK. Gastric volvulus: unraveling the diagnosis with MPRs. Emerg Radiol. 2019;26(2):221-225. doi: 10.1007/s10140-019-01669-0.
- Kao AM, Ross SW, Otero J, Maloney SR, Prasad T, Augenstein VA, et al. Use of computed tomography volumetric measurements to predict operative techniques in paraesophageal hernia repair. Surg Endosc. 2020; 34(4):1785-1794. doi: 10.1007/s00464-019-06930-8.
- Ouyang W, Dass C, Zhao H, Kim C, Criner G, COPD Gene Investigators. Multiplanar MDCT measurement of esophageal hiatus surface area: association with hiatal hernia and GERD. Surg Endosc. 2016;30(6):2465-2472. doi: 10.1007/s00464-015-4499-9.
- Chan DL, Huang BW, Yip J, Chug M, Iliopoulos J, Hennessy A, et al. CT oesophageal hiatal surface area measurements: an objective and sensitive means of hiatal hernia detection. Surg Open Dig Adv. 2023;9(4): 100085. doi: 10.1016/j.soda.2023.100085.
- Rengo M, Boru CE, Badia S, Iossa A, Bellini D, Picchia S, et al. Preoperative measurement of the hiatal surface with MDCT: impact on surgical planning. Radiol Med. 2021;126(12):1508-1517. doi: 10.1007/s11547-021-01413-0.
- Elhage SA, Kao AM, Katzen M, Shao JM, Prasad T, Augenstein VA, et al. Outcomes and CT scan three-dimensional volumetric analysis of emergent paraesophageal hernia repairs: predicting patients who will require emergent repair. Surg Endosc. 2022;36(2):1650-1656. doi: 10.1007/s00464-021-08415-z.





IMAGES IN RADIOLOGY

CT and MRI calcifications in the basal ganglia in primary hypoparathyroidism

Jorge A. Montero-Torres* and Omar Sanchez-Figueroa

Department of Radiology and Imaging, Hospital de Especialidades, Centro Medico Nacional del Bajio, Instituto Mexicano del Seguro Social, Leon, Guanajuato, Mexico

A 13-year-old girl presented with recurrent cognitive seizures, paresthesias of the lower limbs, and fatigue. A non-contrast computed tomography (CT) scan of the head showed symmetrical hyperdense basal ganglia calcifications, particularly in the globus pallidus (Figure 1). Brain magnetic resonance imaging (MRI) showed hyperintense signals on T1-weighted images corresponding to

the calcified regions, with subtle high signal intensity on T2-weighted/FLAIR images and no susceptibility artifacts on T2-weighted gradient-echo sequences (Figure 2). Laboratory results were hypocalcemia (6.9 mg/dL, normal range 8.8-10.8 mg/dL) and an abnormally low parathyroid hormone level (4.2 pg/mL, normal range 10-65 pg/mL). The diagnosis was primary hypoparathyroidism.

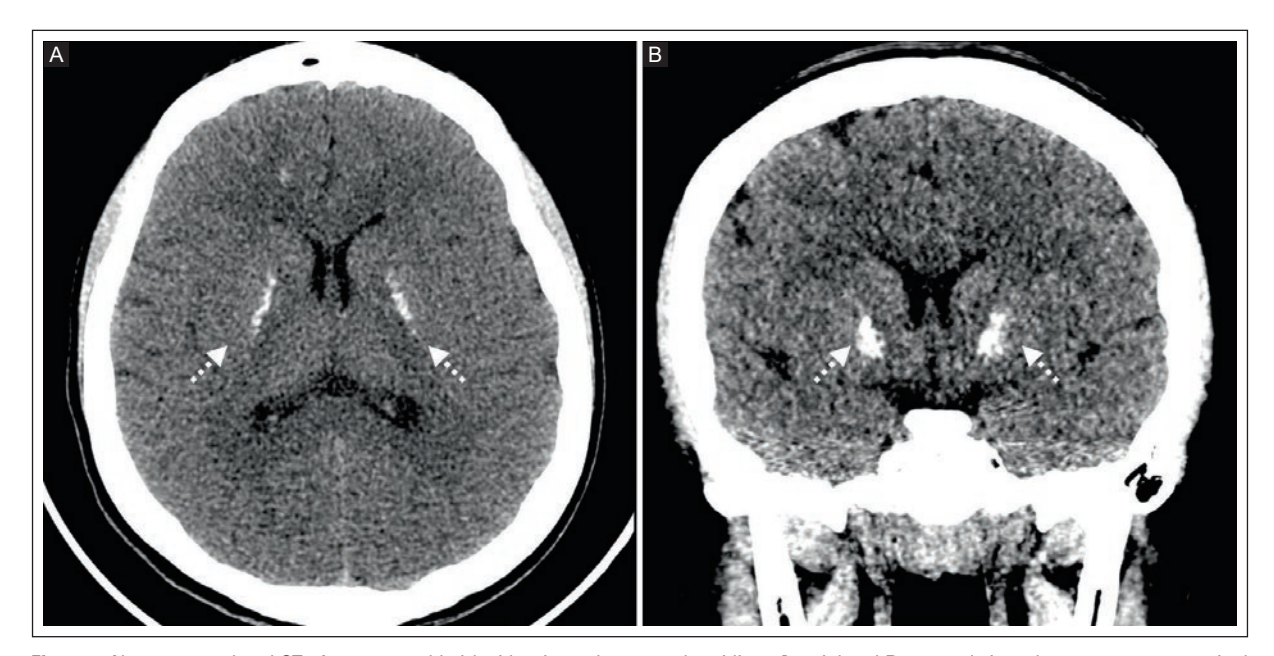


Figure 1. Non-contrast head CT of a 13-year-old girl with primary hypoparathyroidism. **A:** axial and **B:** coronal view show coarse symmetrical calcifications in the basal ganglia with an average attenuation of 79 HU.

CT: computed tomography; HU: Hounsfield units.

*Corresponding author:

Jorge A. Montero-Torres
E-mail: jorge_montero08@hotmail.com

Received for publication: 29-01-2025
Accepted for publication: 11-07-2025
DOI: 10.24875/JMEXFRI.25000005

Available online: 10-10-2025 J Mex Fed Radiol Imaging. 2025;4(3):211-213 www.JMeXFRI.com

2696-8444 / © 2025 Federación Mexicana de Radiología e Imagen, A.C. Published by Permanyer. This is an open access article under the CC BY-NC-ND (https://creativecommons.org/licenses/by-nc-nd/4.0/).

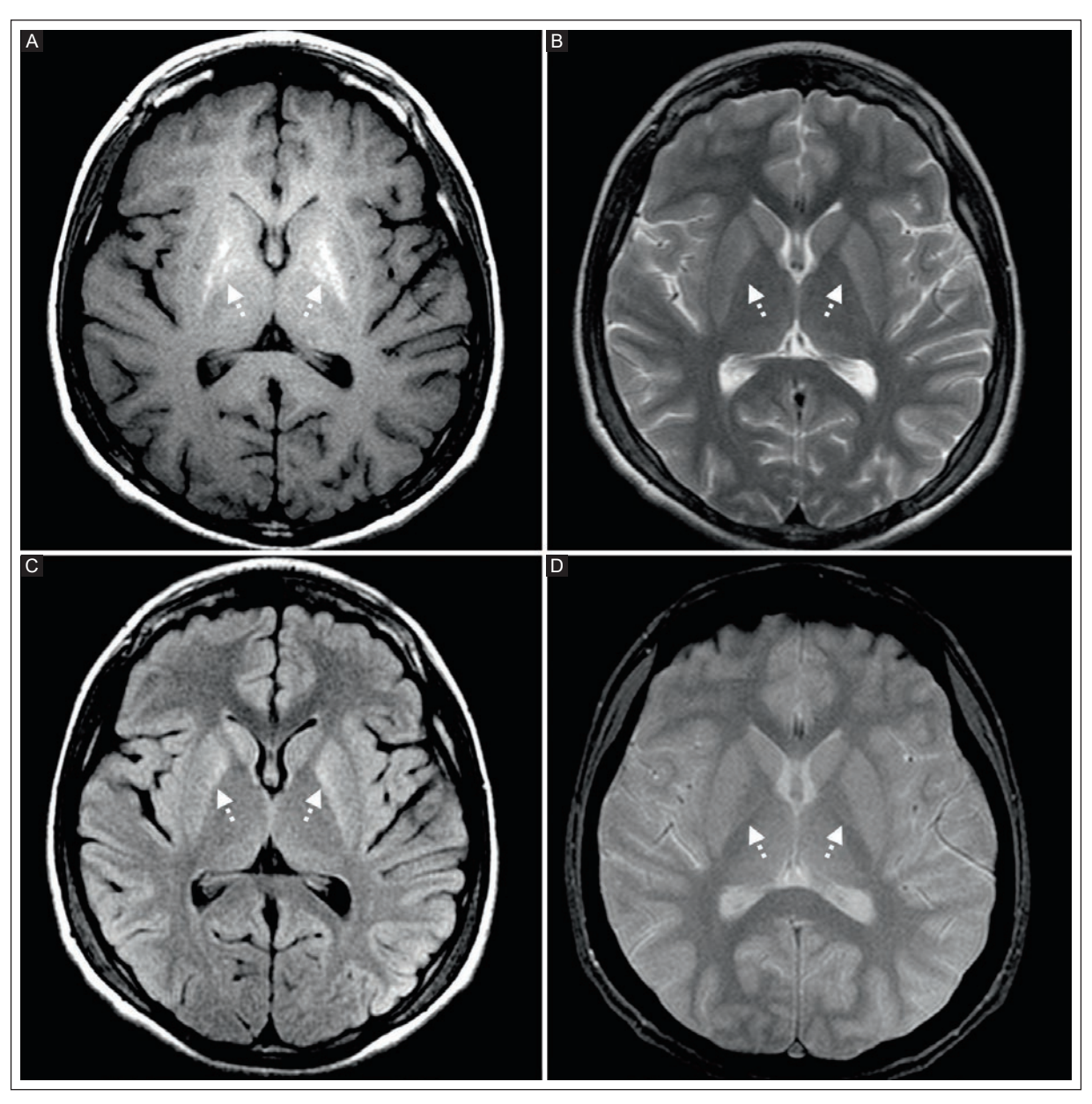


Figure 2. Brain MRI of a 13-year-old girl with primary hypoparathyroidism. A: axial T1-weighted image shows bilateral, symmetrical hyperintensity in the globus pallidus (white arrows). B: axial T2-weighted image shows subtle hyperintensity in the medial aspect of the bilateral putamen, corresponding to the calcifications visible on non-contrast CT (white arrows). C: axial T2-FLAIR image shows mild hyperintensity in the medial aspect of the bilateral putamen (white arrows). D: absence of hypointensity in the basal ganglia, which is more visible on T2* (white arrows). No magnetic susceptibility artifacts are visible.

CT: computed tomography; FLAIR: fluid-attenuated inversion recovery; MRI: magnetic resonance imaging.

T2 and T2*-weighted images of calcifications are uncommon in pediatric patients. They appear hypointense on T2 or gradient-echo sequences and are considered abnormal, often suggesting syndromic or metabolic disorders¹. Basal ganglia calcifications are often idiopathic but can also be associated with conditions such

as hypoparathyroidism². Brain MRI is sensitive to the magnetic susceptibility effects of calcified tissue. Typical MRI calcified tissue is hypointense on T1-T2 weighted and gradient-echo sequences. However, microcalcifications shorten the T1 relaxation time of surrounding water molecules due to their greater dispersion, resulting in T1

hyperintensity without producing susceptibility artifacts on T2 sequences³. Symmetry and localization in the globus pallidus are characteristic findings. A novel finding in this case is the absence of susceptibility artifacts in gradient-echo imaging and the absence of hypointensity in T2-weighted images.

Acknowledgements

The authors thank Professor Ana M. Contreras-Navarro for her guidance in preparing and writing this scientific paper.

Funding

This paper received no external funding.

Conflicts of interest

The authors declare that they have no conflicts of interest.

Ethical considerations

Protection of humans and animals. The authors declare that the procedures followed complied with the ethical standards of the responsible human experimentation committee and adhered to the World Medical Association and the Declaration of Helsinki.

Confidentiality, informed consent, and ethical approval. The authors declare they followed their center's protocol for sharing patient data.

Declaration on the use of artificial intelligence. The authors declare that no generative artificial intelligence was used in the writing of this manuscript.

REFERENCES

- Zavatta G, Clarke BL. Basal ganglia calcification in hypoparathyroidism and pseudohypoparathyroidism: local and systemic metabolic mechanisms. J Endocrinol Invest. 2021;44(2):245-253. doi:10.1007/s40618-020-01355-w.
- Livingston JH, Stivaros S, Warren D, Crow YJ. Intracranial calcification in childhood: a review of etiologies and recognizable phenotypes. Dev Med Child Neurol. 2014;56(7):612-626. doi:10.1111/dmcn.12359.
- Auffray-Calvier E, Lintia-Gaultier A, Bourcier R, Aguillar Garcia J. Calcifications des noyaux gris centraux [Basal ganglia calcification]. Rev Med Interne. 2020;41(6):404-412. doi:10.1016/j.revmed.2020.02.016.



Ultrasound

Affiniti

Designed for your everyday

Stepping up to today's Philips Affiniti Ultrasound System means stepping up to the next level of performance to help with a confident diagnosis using streamlined workflow.

Upgrade to the latest Affiniti capabilities



Intuitive use

Experience a user interface and workflow that helps increase your productivity.



Enhances user workflow with system-guided protocols that can be easily customized to suit your needs



Tablet-like 30.48 cm (12 in) touchscreen with workflow-related controls for ease of use



Next Gen AutoSCAN reduces button pushes by up to 54% with pixel-by-pixel real-time optimization and reduces the need for user adjustment while also enhancing transducer plunkability.*



At just 83.5 kg (184 lb), the system is 16% lighter than its predecessor system**



Shared transducer family across Affiniti and Compact 5000*** series systems helps maximize your investment



Wireless networking aids workflow

- * When comparing VM10 performance to VM7.
- *** R.S. #1437E2024 SSA.





Battery backup with sleep mode allows the system to sleep in 2 seconds and return to full functionality in 20 seconds

Consumes nearly 40% less power compared to our legacy predecessor system*





Intelligent imaging



Flow Viewer

Defines vasculature with a 3D-like appearance using both the velocity and power of the Doppler signal to accurately represent vascular flow topography



MicroFlow Imaging (MFI)

Provides remarkable sensitivity and detail in assessing blood flow



Find out more at

www.philips.com.mx/healthcare/solutions/ultrasound



Improved Diagnostic Accuracy, Especially for Dense Breasts

Automatically analyze and generate quantitative density assessment

Lunit Al-driven technology empowers radiologists to:

- > Enable early diagnosis for breast cancer
- > Reduce radiologists reading volume
- Automatically analyze and generate quantitative density assessment
- > Promote workflow efficiency

Informed decisions to conquer cancer



Lunit #13 lunit.io





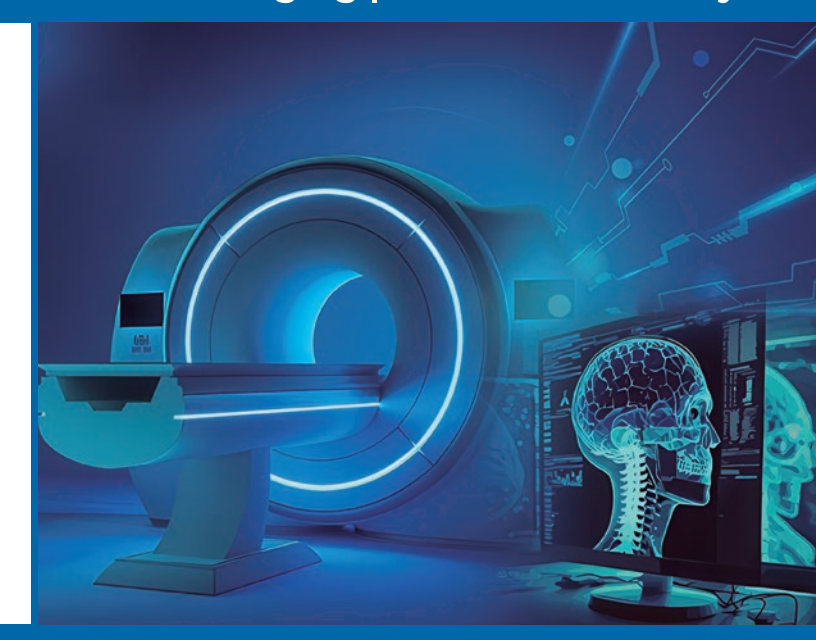
We are in different fields of radiology, from digital to molecular imaging.

Radiology Center | Nuclear Medicine | Molecular Imaging | Clinical Laboratory

Job opportunities for general and sub-specialty radiologists.

Consultancy in the implementation of radiology department for government agencies.

Contact: Lic. Guadalupe Pinzon Direct Line: +52 33 3648 9542 E-Mail: gpinzon@cid.com.mx



Guadalajara, Jalisco, Mexico

www.cid.com.mx

Call Center: +52 33 3817 0882

MRH Series Horizontal Radiographic Systems

CMR

cmr-rx.com

x contacto@cmr3.com.mx +52 55 9063 2047



solutions for advanced care



SUPPORTING RADIOLOGY MEDICAL EDUCATION SINCE 1979







Advanced Specialization Course in Breast Imaging

Hybrid Program (Academic-Work-Based)

*Theoretical and Practi<mark>c</mark>al *100% On-Site

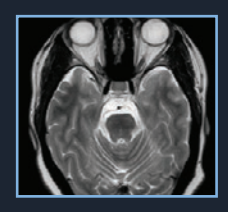
*Accredited by:



(a) +52 833 212 9170 (b) +52 833 658 5800



Diagnóstico Especializado en Imágen

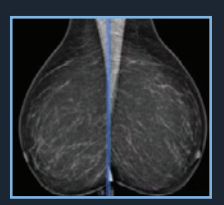












Dr. Gerardo S Navarro Gomez Radiologist Dr. Eduardo Sarda Inman Radiologist Dra. Beatriz Gonzalez Ulloa Radiologist

Clinical Laboratory

Digital Radiology

Digital Mammography

Tomosynthesis

Contrast-Enhanced Mammography

Computed Tomography (CT)

General Ultrasound

Color Doppler Ultrasound

4D Structural Obstetric Ultrasound

Musculoskeletal Ultrasound

Peripheral Doppler Ultrasound

gnetic Resonance Imaging (MRI)







OAXACAN RADIOLOGY OFFICE DEDICATED TO OFFERING IMAGING SERVICES.

Committed to offering image quality and diagnostic certainty to its patients and doctors in Imaging studies.

OUR SERVICES:

Tomography | Ultrasonido Special X-rays | X-rays

LOCATION:

Calle Álamos #603, Col, Reforma, between Jazmines and Heroico Colegio Militar, Oaxaca de Juárez, Oaxaca.



